STORED ENERGY MAPS IN DEFORMED METALS USING SPHERICAL NANOINDENTATION

A Dissertation
Presented to
The Academic Faculty

by

Shraddha Jagadishbhai Vachhani

In Partial Fulfillment
of the Requirements for the Degree
Doctor of Philosophy in the
George W. Woodruff School of Mechanical Engineering

Georgia Institute of Technology
May, 2014

STORED ENERGY MAPS IN DEFORMED METALS USING SPHERICAL NANOINDENTATION

Approved by:

Dr. Surya R. Kalidindi, Advisor
George W. Woodruff School of Mechanical Engineering
Georgia Institute of Technology

Dr. Richard W. Neu
George W. Woodruff School of Mechanical Engineering
Georgia Institute of Technology

Dr. Antonia Antoniou
George W. Woodruff School of Mechanical Engineering
Georgia Institute of Technology

Dr. Hamid Garmestani
School of Materials Science and Engineering
Georgia Institute of Technology

Dr. Roger D. Doherty
Department of Materials Science and Engineering
Drexel University

Date Approved: January 7, 2014

To my parents, Jagadishbhai and Varshaben Vachhani.
Thank you for your unconditional love and support

ACKNOWLEDGEMENTS

First and foremost, I would like to express my heart-felt gratitude towards my advisor Dr. Surya R. Kalidindi for the encouragement and thoughtful guidance during my Ph.D. work. He has been extremely supportive and has given me the freedom to pursue various projects without objection. I am also extremely thankful to Dr. Roger D. Doherty, without whose inputs this work would have been incomplete. I realize how extraordinarily lucky I have been to have such wonderful mentors and hope I will find opportunities to work with them in the future.

I would also like to thank Dr. Richard Neu, Dr. Hamid Garmestani and Dr. Antonia Antoniou for serving on my committee and providing valuable inputs and suggestions over this period.

I would like to express my gratitude towards Dr. Raja K. Mishra and Dr. Nathan Mara, for providing me with two invaluable internship opportunities in their respective groups at General Motors and Los Alamos National Laboratory over two summers. I also owe thanks for the help and guidance of Dr. Anil Sachdev, Mr. Robert Kubic and Dr. John Capenter during these internships.

A very special thank you to Dr. Siddhartha Pathak, who was always by my side since the first day I met him in graduate school. His guidance, support and encouragement have been immensely valuable throughout this period.

Thank you to a very long list of past and present members of the MinED research group for being exceptionally good and very helpful colleagues. I will cherish my

friendship with many of them in the future. A special thanks to Dr. Amanda Levinson for sharing the highs and lows.

I am also thankful to the ME staff at GaTech, specially Ms. Glenda Johnson, Ms. Trudy Allen and Ms. Samantha James and MSE staff at Drexel University, particularly Keiko Nakazawa and Dorilona Rose for their help.

Last but not the least, a big thank you to my family for their love, understanding and encouragement throughout my education, without which I would not be here today.

TABLE OF CONTENTS

Page

LIST OF TABLES

LIST OF FIGURES

LIST OF SYMBOLS AND ABBREVIATIONS

Abbreviations

FCC	Face Centered Cubic
NI	Nanoindentation
SEM	Scanning Electron Microscopy
EBSD	Electron Backscatter Diffraction
OIM	Orientation Imaging Microscopy
ISS	Indentation Stress-Strain
CSM	Continuous Stiffness Measurement
IPF	Inverse Pole Figure
GB	Grain Boundary
GOS	Grain Orientation Spread
SIBM	Strain Induced Grain Boundary Migration
SPM	Scanning Probe Microscopy
RD	Rolling Direction
TD	Transverse Direction
ND	Normal Direction
CPFEM	Crystal Plasticity Finite Element Model

Symbols

P	Indentation load
h_e	Elastic indentation depth
h_t	Total indentation depth
E_{eff}	Effective Modulus
E_s	Young’s Modulus of the sample
E_i	Young’s Modulus of the indenter
R_{eff}	Effective Radius
R_s	Sample Radius
R_i	Indenter Radius
S	Contact stiffness
a	Indentation radius of contact
$\tilde{P}$	Raw indentation load
$\tilde{h}$	Raw indentation displacement
P^*	Load correction
h^*	Displacement correction
σ_{ind}	Indentation Stress
ε_{ind}	Indentation Strain
P_{act}	Actual load during indentation
P_{app}	Apparent load during indentation
ΔP	Peak-to-peak indentation load range
h_{act}	Actual displacement during indentation

h_{app}	Apparent displacement during indentation
Δh	Peak-to-peak indentation displacement range
S_{act}	Actual or corrected stiffness
S_{app}	Apparent stiffness
P_{max}	Peak indentation load
Y_{ind}	Indentation yield strength
g	Crystal orientation
Φ_1, Φ, φ_2	Orientation represented in the form of Bunge-Euler Angles
M	Taylor factor
ρ	Dislocation density
τ_{crss}	Critical resolved shear stress
γ	Total shear on a given slip system
ε	Imposed strain
d	Deformation mode

SUMMARY

Microstructure changes that occur during the deformation and heat treatments involved in wrought processing of metals are of central importance in achieving the desired properties or performance characteristics in the finished products. However, thorough understanding of the evolution of microstructure during thermo-mechanical processing of metallic materials is largely hampered by the lack of methods for characterizing reliably their local (anisotropic) properties at the scale of grains and grain boundaries. This has also been one of the biggest hindrances in our ability to develop highly accurate, physics based homogenization theories to predict material properties as well as design effective processing routes for specific applications.

Nanoindentation technique, with its high resolution load and depth sensing capabilities, provides an excellent opportunity to quantify the mechanical properties at the length scales smaller than an individual grain in a polycrystalline sample. Recently, remarkable advances have been made in nanoindentation data analysis techniques which use the initial loading segment of the test data to transform the load-displacement data obtained from a spherical nanoindentation test into a meaningful indentation stress-strain (ISS) curve. These ISS curves have been shown to capture various aspects of the elastic-plastic material response more reliably, compared to conventional nanoindentation data analysis protocols. This capability now provides a means to quantify subtle changes in the mechanical properties at a sub-micron length scale.

Since the Continuous Stiffness Measurement (CSM) is central to the new data analysis procedures, the effect of the CSM on the indentation stress-strain curves during

spherical nanoindentation was critically examined, as the first part of this dissertation. For the remainder of this work, the local mechanical property information obtained from spherical nanoindentation data was combined with complementary structure information obtained locally at the indentation site using orientation imaging microscopy to carry out detailed investigations of the changes in the structure and mechanical properties occurring as a result of the imposed macroscale deformation. This combination of characterization techniques makes an effective tool for studying the underlying mechanisms that govern the development of stored energy gradients in metallic materials.

The changes in the structure and mechanical properties of high purity aluminum in the annealed and deformed (to varying strain levels) conditions were systematically studied using this approach. One of the reasons for choosing pure aluminum is that it exhibits very little elastic anisotropy and the plastic deformation mechanisms at the single crystal level are already well understood. This knowledge aids in the data analysis and interpretation. Also, in the fully annealed condition, the aluminum samples can be produced to exhibit extremely large grain sizes (of the order of several millimeters) making it possible to investigate individual grains and specific grain boundaries while avoiding contributions from the neighbors. Following is a brief outline of the tasks carried out and the main findings of this work.

- Tests were performed on pure aluminum and fused silica at different oscillation amplitudes and frequencies in order to determine the effect of the CSM on the ISS curves extracted from spherical nanoindentation data. It was seen that the amplitude and frequency of the superimposed oscillations in the CSM affected the harmonic stiffness signal (S) most significantly, owing to the machine dynamics and the characteristics of the data collection system. The values for the harmonic stiffness are unreliable at lower oscillation frequencies, and the noise levels are very high for low oscillation amplitudes. Therefore, 45 Hz–2 nm oscillations in the CSM during nanoindentation testing appears to be the best option for extracting reliable ISS curves and Y_{ind} from nanoindentation data.

- ISS curves were used to extract the indentation yield strength (Yind) from the raw nanoindentation data. The inherent dependence of the Yind on the local crystal lattice orientation was documented by measuring the mechanical response at various locations of known crystal lattice orientation on a fully annealed aluminum sample. In spite of a negligible difference in the dislocation density in the differently oriented grains in the fully annealed sample, it was seen that the Yind can vary by as much as 40% depending on the local crystal orientation. Quantifying the contribution of lattice orientation to the measured Yind is necessary to reliably estimate the specific contribution of the changes in dislocation density to the Y_{ind}.
- Following this, the local yield properties within the grains and close to the grain boundaries were characterized on samples deformed to light (10% reduction in height) and moderate (20% reduction in height) levels of strain. The microstructure that develops during deformation is highly complex and the dislocation density can vary significantly from one location to another within the grain. Using percentage change in the Yind as an indicator of local dislocation density, it was concluded that grains with a higher Taylor factor have higher stored energy content as compared to grains with a lower Taylor factor. Although

this relationship between Taylor factor and local stored energy of deformation has been hypothesized by many researchers in the past, there has been little direct experimental evidence to show it.

- The regions near grain boundaries in a moderately deformed high purity aluminum sample were also investigated in order to gain insights into the role of grain boundaries in the development of stored energy gradients during deformation. It was concluded that ‘soft’ grains when present next to ‘hard’ grain harden significantly more in the immediate vicinity of the boundary. The extent of hardening near the grain boundary increases with the increase in the difference in the Taylor factor for the adjacent grains. When both grains on either side of the boundary had similar values of Taylor factor, no additional hardening at the grain boundary was observed. A fairly strong correlation was observed between the extent of hardening at grain boundaries and the difference in Taylor Factor across the grain boundary.

CHAPTER 1

INTRODUCTION

It is generally agreed that advancement in our ability to develop highly accurate, physics based homogenization theories to predict material properties is dictated by the capability of extracting relevant information at the various length scales of interest. Over the last decade, tremendous advance in characterization of local mechanical properties on a sub-micron length scale has been possible with the availability of nanoindentation techniques [1-4] (also known as Instrumented Indentation Testing (IIT) or Depth-Sensing Indentation (DSI)). Dr. Siddhartha Pathak, during his PhD work in our research group, developed new data analysis procedures [5-6] that convert load-displacement data obtained from spherical nanoindentation into indentation stress-strain (ISS) data. This ISS data allows one to follow the local elastic, yield and post elastic behavior of materials during the deformation process. With this new characterization tool at our disposal, we are now in a position to gain insights into the grain-scale evolution of microstructure in deformation of polycrystalline metal.

Wrought processing of metals commonly leads to the development of complex heterogeneous microstructures with several hierarchical length-scales. Microstructure changes that occur during the deformation and heat treatments involved in these processes are of central importance in achieving the desired properties or performance characteristics in the finished products. Therefore, establishment of processing routes that optimize the performance of the final product is a major activity in the metals processing industry. In spite of over 70 years of research in this field, there still exist many gaps in our understanding of the evolution of deformed [7] and recrystallized microstructures [8-9]. The development of a robust physics-based model for the prediction of microstructures resulting from deformation and recrystallization processes has thus far eluded the scientific community. One of the main reasons is the lack of experimental protocols that reliably quantify the local changes in the mechanical response at the scale of individual grains and in the grain-boundary regions. With the recent developments in the nanoindentation data analysis procedures, we now have a technique that can be used to track changes in the local mechanical properties during such processes and provide insights into the underlying mechanisms governing these processes. The indentation data, together with the complimentary structure information measured locally at the indentation site using electron backscatter diffraction (EBSD), is thus expected to provide new insights about microstructure evolution during the thermo-mechanical processes employed by the metals producing industry.

The aim of this dissertation is to extend the methodologies developed by Dr. Pathak to investigate the role of plastic anisotropy and grain boundaries in the evolution of microstructure during macroscale deformation processes. This dissertation is laid out in the following manner. Chapter 2 will provide essential background and the current state-of-the-art for topics specific to the work discussed herein, including recrystallization and deformation processing in cubic metals and spherical nanoindentation data. Chapter 3 will present a systematic investigation to study the effect of the continuous stiffness measurement (CSM) on the mechanical properties extracted using spherical nanoindentation. Chapters 4 summarize the details of the materials used, the macroscopic processing and metallography. Chapters 5-7 will present the results and discussions of three experimental investigations aimed at addressing some of the existing gaps in our understanding of stored energy evolution during the deformation of cubic metals. In these studies, local mechanical property information obtained using spherical nanoindentation techniques will be combined with complimentary structure information measured using EBSD to establish the local structure-property relationships. Chapter 5 will discuss the variation in the indentation yield stress as a function of orientation for aluminum in the fully annealed condition and its evolution after light (10%) and moderate (20%) deformation. Chapter 6 will discuss the development of stored energy gradients near grain boundaries in aluminum, after moderate deformation. Chapter 7 will summarize the conclusions of this work and Chapter 8 will discuss possible directions for future research.

CHAPTER 2

BACKGROUND

Plastic deformation and heat treatments are the two of the most commonly used processing steps by the metals industry. Not only do these processes provide a means to transform a metallic material into the final shape desired for service, they are also a means to control the material's internal structure, whereby its properties can be controlled. Deformation leads to significant changes in the microstructure such as changes in the grain shape and size, development of in-grain misorientations and subsequently fragmentation of pre-existing grains. These changes often lead to development of microstructures that are very specific to the deformation part and degree (deformation textures). These changes in the microstructure are closely related to changes in the mechanical properties. Upon subsequent heat treatments, the deformed microstructure in metallic materials is replaced by new 'deformation free' grains by a process of recrystallization. This process is again accompanied by significant changes in the mechanical properties of the materials. The microstructure and associated mechanical properties that develop during recrystallization are strongly influenced by the deformed microstructure.

2.1 Recrystallization

During deformation processes, while most of the work done on the sample is dissipated as heat, a small fraction of it is stored in the material in the form of defects, particularly dislocations. These dislocations and dislocation structures are heterogeneously distributed within the deformed sample and the associated stored energy

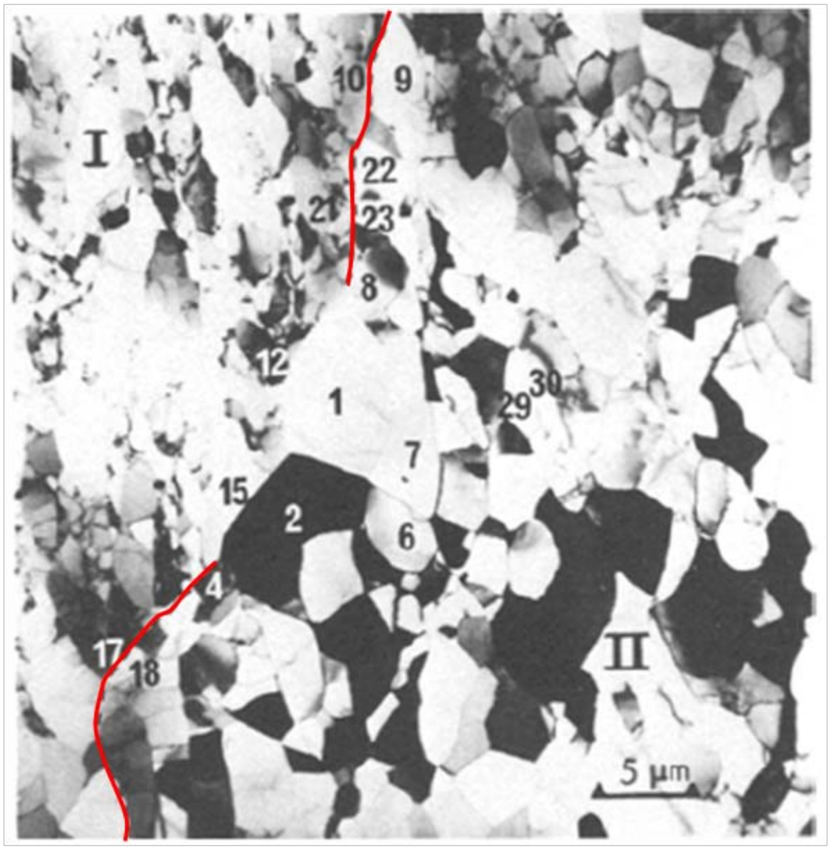

Figure 2.1: High purity aluminum- compressed 40% and annealed for 30s at 328oC. The pre-existing grain boundary is represented by the red line, with orientation differences of 44o about [1 2] between 17-18, 33o about [1 2] between 2-15, 44o about [1 1] between 1-12 and 30o about [1 2] between 21-23 and 9-10. Also, the other large misorientations are 18o about [1 4] between 1-2, 16o between 6-7, -21o about [0 0] between 1-29, -29o about [1 4] between 18-1 and , -10o about [0 2] between 1-23. The irregular shape of the boundary and the fact that the misorientation changes progressively from 18 to 1 and then the further misorientation from 1 to 23 is in the opposite sense, indicates that the nucleation has occurred at a junction of a deformation band within grain II rather than at a pre-existing triple point [10].

differences provide the necessary driving force for the nucleation and growth of new, almost dislocation-free grains during the process of recrystallization [8].

It is understood that the new grains originate from small regions, sub-grains or cells of the same orientation present in the deformed structure [8, 11-13]. Also, the presence of high angle grain boundaries, at least in part, between the sub-grain and its neighbors, along with stored energy gradients across the boundary are necessary for the sub-grains to grow into new recrystallized grains [14]. This is because high angle grain boundaries have higher mobility [15] as compared to low angle boundaries and hence the sub-grains with high angle boundaries grow faster.

It was observed that in moderately deformed high purity aluminum (40% compressed) [10] and high purity iron [16-17], nucleation occurred at intersections of transition bands and pre-existing grain boundaries by the process of strain-induced grain boundary migration (SIBM). This included the invasion of deformed grains by neighboring grains with larger sub-grain sizes and is illustrated in Figure 2.1. The required sub-grain size differences for SIBM nucleation appeared to be occurring by the process of sub-grain coalescence. The enlarged sub-grain then grows into the adjacent grain by migration of the existing high-angle grain boundary between the deformed grains. Szpunar and Doherty [18] proposed a model which explains the requirement of two non-parallel dislocation sinks for the process of sub-grain coalescence and subsequent nucleation. Upon further deformation (60% compression), they observed that the new grains nucleated at the transition bands within the pre-existing grains. At such high strains, the orientation gradients in the transition bands are large and hence the requirement of two non-parallel sinks can by fulfilled within the transition bands.

Another striking characteristic observed during recrystallization of heavily deformed cubic metals is the development of annealing or recrystallization textures [19-21], in which components that form only a negligible fraction of the deformation texture become a dominant feature (e.g.: cube texture after recrystallization of heavily deformed copper and high purity aluminum). The evolution of the cube texture depends on the mode and extent of plastic deformation. Two models [22-23] have been proposed for the development of the special recrystallization textures. Oriented nucleation or frequency advantage attributes the higher rate of nucleation of the recrystallization texture components to its dominance in the final texture while the second model, oriented growth or size advantage, proposes that the recrystallization texture components grow faster than the random grains and hence take up a larger volume fraction. The frequency advantage theory has enjoyed more success than the size advantage model but the actual mechanism responsible for this effect is still a subject of discussion.

Clearly, more work needs to be done in order to understand the kinetics of the recrystallization process before we can develop a physics-based quantitative model to predict the recrystallized microstructure. We need to understand not only where the new grains are most likely to nucleate but also which nuclei will grow the fastest as these are the ones that will survive to form the final recrystallized microstructure. The absence of sensitivity of final recrystallized microstructure to annealing conditions and its strong dependence on the prior plastic deformation indicates that the entire recrystallization process is latent in the deformed microstructure. Hence, understanding microstructure evolution during deformation processes is the key to finding answers to the questions regarding recrystallization.

2.2 Deformation

During deformation, changes in the grain shape and orientation occur due to plastic flow. The imposed deformation is accommodated in the metallic material by means of dislocation movement on different slip systems. This process is highly heterogeneous. The mode of deformation, the orientation of the grains with respect to the loading direction and the orientation of its neighboring grains, all play a role in determining the slip systems that are activated in a given part of the grain. Thus different combinations of slip systems are often activated in different regions within the grain, and this causes the different parts of a grain to rotate to different orientations during the imposed deformation. This results in the development of in-grain misorientations and subsequently grain fragmentation [7, 20, 24].

Detailed study of deformed commercially pure aluminum with coarse columnar grains (see Figure 2.2) has shown two types of grain fragmentation, those with repeating orientation fields and those with non-repeating orientation fields [7]. Fragmentation of the grains with repeating orientation fields was explained as an inherent instability of the initial crystal orientation when subjected to a particular deformation mode. On the other hand, fragmentation of the grains with non-repeating orientation fields was seen as a natural consequence of the grain interactions. This was particularly observed when a smaller and/or softer grain had a common boundary with the larger and/or harder grain. Grain fragmentation also results in the formation of transition bands which accommodate the misorientation between adjacent regions of the grains that have rotated in different directions. At low to moderate deformations, the transition bands have a finite width and

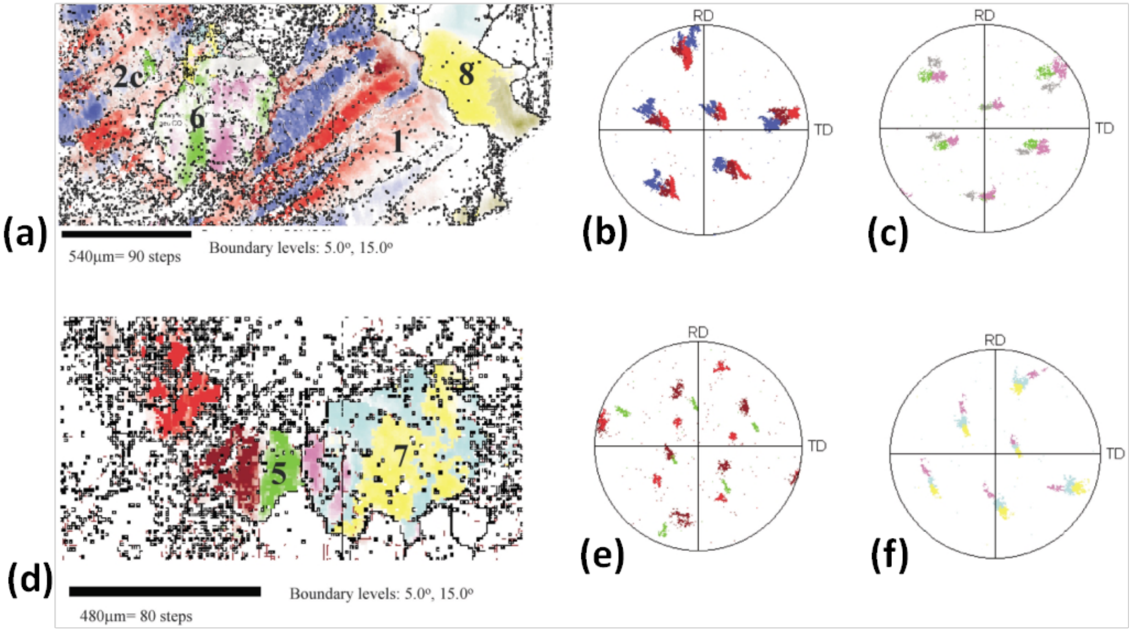

Figure 2.2: OIM micrographs from high purity (99.9%) aluminum sample, compressed at room temperature to a height reduction of 40%. Grain #1 and #2c in Figure 2(a) show elongated deformation bands with repeating orientation fields while grain #6 in Figure 2(a) and grain #7 in (d) show non-elongated deformation bands with repeating orientation fields. On the other hand grain #5 and #8 in (a) and (d) respectively shows roughly equiaxed misoriented regions. (b) shows the pole figure for the different but repeating orientations present in grain #1 and #2c. Pole figures for the orientation present in grain #6, #5 and #7 are shown in (c), (e) and (f) [7].

can be distinguished from the prior grain boundaries but as more deformation is imposed, the thickness of these bands decreases and at high strains, the transition bands are difficult to distinguish from the pre-existing grain boundaries. Figure 2.3(a) shows the microstructure in Fe-3%Si, after 80% deformation, showing severe grain fragmentation and very sharp transition bands. Figure 2.3(b) shows the same region after a short heat treatment, in which the new recrystallized nuclei are marked in dotted lines. As mention in the previous section, our capabilities to predict the location and orientation of these nuclei are very limited at present.

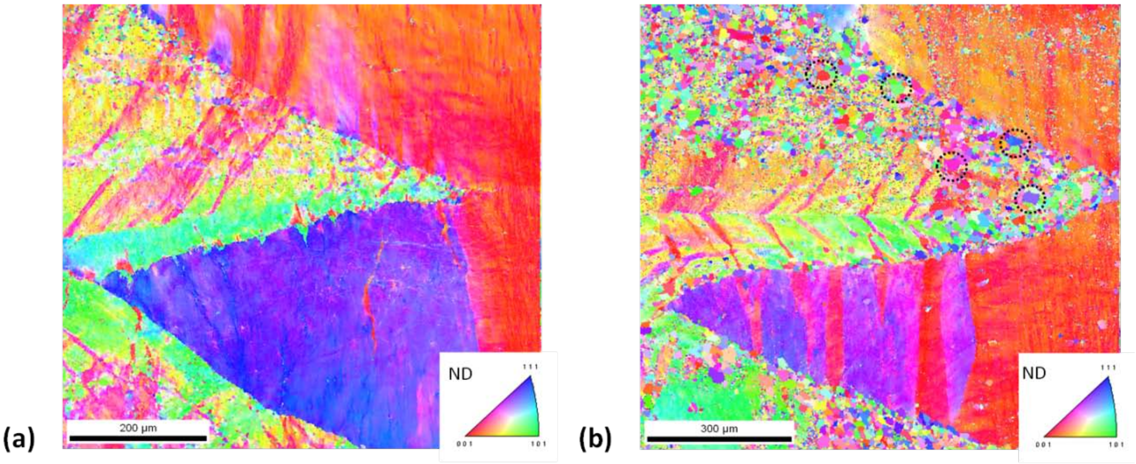

Figure 2.3: IPF maps showing the (a) deformed microstructure in a Fe-3% Si steel after 80% reduction in height. (b) The same region after partial recrystallization (620°C for 30 minutes). The dotted circles show the new recrystallized grains in the partially annealed structure.

Crystal plasticity models [25-26] that account for slip activity on individual slip systems in each grain during a selected deformation process have been developed and extensively used in literature. The crystal plasticity models have also been successfully used in finite element simulations to model complex forming operations [27-28]. These simulations have been successful in predicting the average crystallographic texture after deformation but have enjoyed varying success in predicting the orientations of the individual grains in the sample [7, 29-31]. While the crystal plasticity models failed almost entirely in predicting individual grain orientations in the work on Al - 0.15 wt % Fe – 0.07 wt % Si by Panchandeeshwaran et al. [29], they enjoyed much more success for the work on Al-0.1% Mn by Quey et al. [31]. This may have been because in the former case the presence of precipitates in the former case which would affect the motion of dislocations. The crystal plasticity models predict development of in-grain misorientations but are generally unable to capture the nature and extent of these misorientations. This indicates that the physics of grain fragmentation is not accurately captured in the currently used crystal plasticity models [7].

Consideration of local microstructure evolution through OIM measurements constitutes only one aspect of the characterization of a deformed material at the sub-micron length scale. Another equally important attribute to be considered is the local stored energy gradients that develop in the deformed material. As mentioned in the previous section, stored energy gradients play a vital role in determining the recrystallization and grain growth processes. Additionally, understanding the evolution of stored energies during deformation has profound impact in the development of strain hardening theories in polycrystalline materials. It is well known that stored energy is strongly dependent on orientation and that the stored energy of cold work generally increases with the increase in Taylor factor [32-33]. However, quantitative information regarding the orientation dependence of the stored energies and its evolution with continued deformation is limited, mainly due to the limited data available on this subject.

Most studies consider only few orientations [33-35] and few large strain increments [34-36]. Figure 2.4 shows the stored energy for two orientations in OFHC copper at increasing strain levels, measured using X-ray diffraction studies.

Investigations using microhardness tests [34, 36-37] and X-ray diffraction [34, 38] do not provide the necessary spatial resolution or possess the requisite reliability, particularly at high deformation levels where there is significant grain fragmentation and development

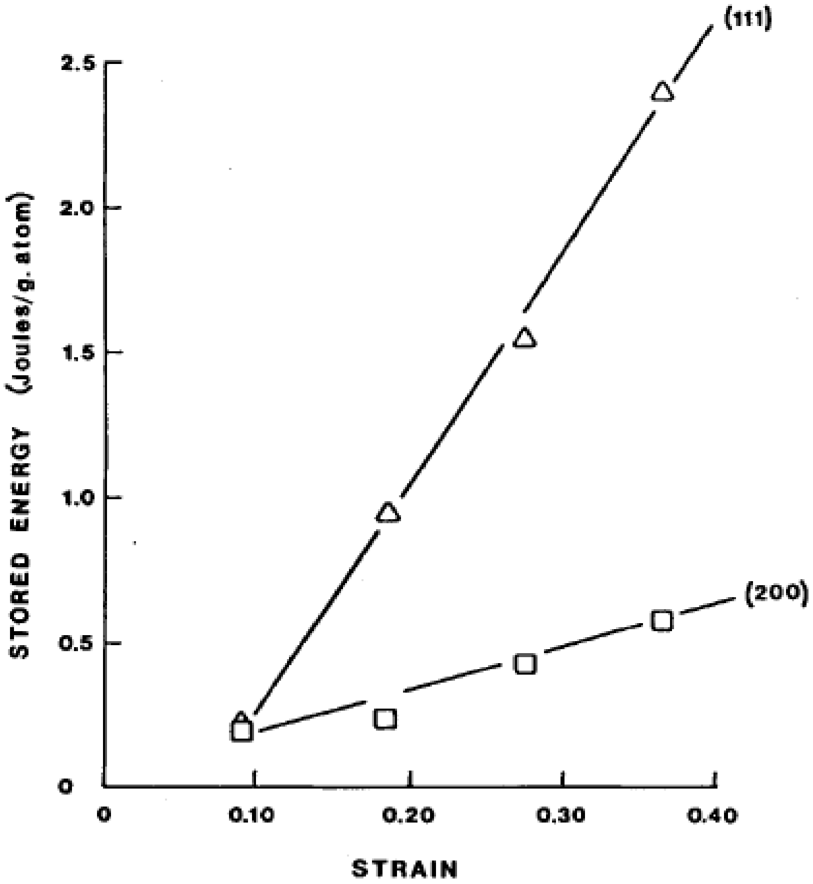

Figure 2.4: Correlation of stored energy of cold work with strain level for (111) and (200) diffraction profiles (Taylor factors of 3.67 and 2.45, respectively) in OFHC copper [33].

of sub-grain microstructure. In these cases, local stored energy is not only dependent on the orientation of the parent grain, but can vary significantly from one region to another within a pre-existing grain. Therefore a systematic study of the evolution of stored energies during the deformation of polycrystalline materials is critical to address the existing gaps in our understanding of the recrystallization process.

Another equally important microstructural feature that is known to have a profound effect on the evolution of microstructure during deformation is the grain boundary. The state-of-the-art in our understanding of grain boundary behavior and some critical gaps in our knowledge of these are summarized below.

2.3 Role of Grain Boundaries

As mentioned is section 2.1, grain boundaries are important nucleation sites during recrystallization. Grain boundaries also play an important role in determining the stored energy variations in the deformed structure and a deeper understanding of this phenomenon is critical for gaining insights into the nucleation and grain growth kinetics.

Since the discovery of the Hall-Petch effect [39-40] more than sixty years ago, it is well known that the yield strength of a polycrystalline material can be connected to its average grain size by an inverse power-law relationship. The dislocation pile-up model [41] proposed to explain this strengthening effect implicitly assumes that the grain boundaries are poor dislocation sinks. An alternate model proposes the presence of a hardened region in the vicinity of the grain boundary [42] as a result of the increased dislocation density in the area. These concepts are still a topic of debate in literature, again, mainly due to the lack of experimental protocols for reliably extracting information about the material behavior at the sub-micron length scale.

Also, the Hall-Petch effect, while highly successful in capturing the homogenized effect of grain boundaries on the macroscale mechanical properties of metallic materials, attributes little importance to the difference in the behavior of the different type of boundaries. In other words, it does not provide any information on the factors that determine grain boundary behavior. It is known that the presence of low angle boundaries has little hardening effect in the mechanical response of bicrysals [43-44]. High angle boundaries, on the other hand provide a significant barrier to movement of dislocations [15]. Several attempts to characterize the mechanical behavior of high angle boundaries have been made using the micropillar approach [45-49], nanoindentation testing [48-52] as well as TEM studies [53-54]. Micro-pillar tests require intricate fabrication and handling as well as highly specialized testing equipment [55-56]. The process is also very effort intensive and hence limits the number of pillars that can be tested within a reasonable time-frame. While nanoindentation testing addresses these issues satisfactorily, the data analysis commonly used to interpret nanoindentation data is not sufficiently advanced to provide the necessary resolution and repeatability (see Figure2.5). Subtle differences in the local mechanical properties cannot be identified using conventional nanoindentation testing methods. Therefore, the interaction between dislocations and grain boundaries is still a topic of debate. In some cases, contradictory reports exist regarding the grain boundary behavior [45-46]. A careful analysis and comparison of grain boundary character for the boundaries studied can potentially provide an explanation to these seemingly contradictory observations.

Since grain boundaries play a vital role in the development of deformation and recrystallization microstructures, there clearly is a critical need for a systematic study correlating the mechanical response at grain boundaries to the local microstructure and crystallography, in order to better understand the role grain boundaries play during thermo-mechanical processing of polycrystalline metals.

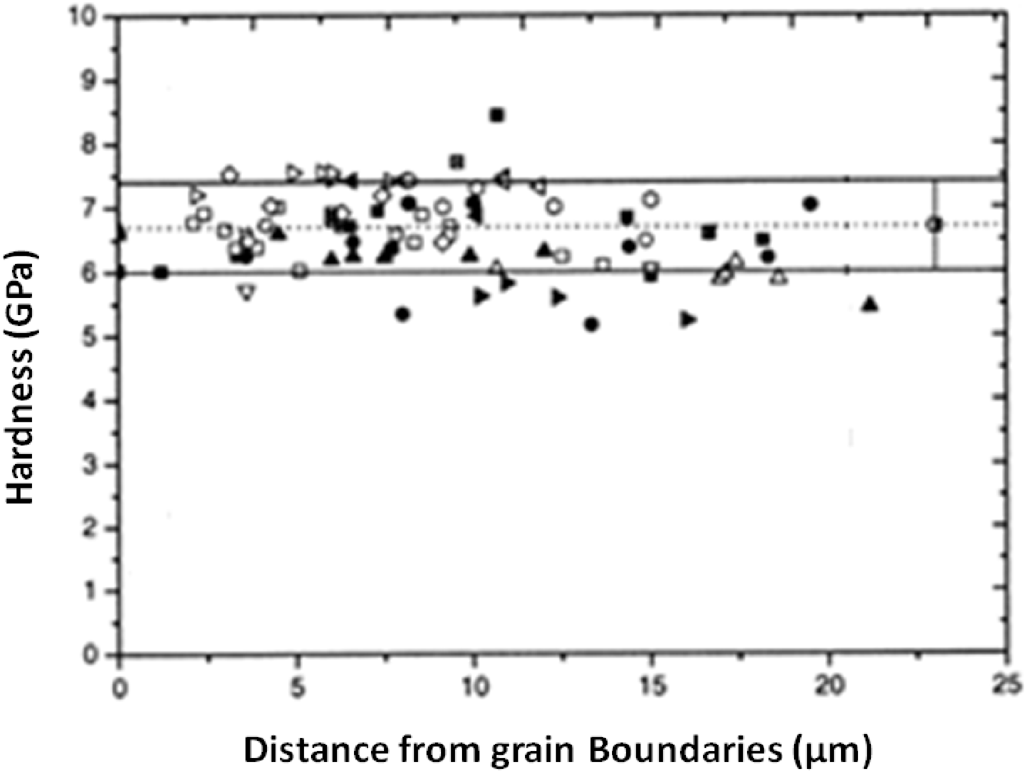

Figure 2.5: Hardness H against the shortest distances from an indent to the nearest grain boundary in the Ni3Al sample. The H values were obtained by indentation using a cube-corner tip and a maximum load of 300 mN. The H values shown were obtained by direct SEM imaging. The mean H value for the grain interior is indicated by the dotted line while the horizontal solid lines show the upper and lower bounds of one standard deviation from such mean value. The data points show the H value at distances less than a few times the indent size. The error bar on the right of the diagrams shows the variations due to judgmental errors of the indent size [52].

2.4 Spherical Nanoindentation

Indentation is a versatile tool for measuring the mechanical properties from small material volumes [57]. Nanoindentation, with its high resolution depth and load sensing capabilities, can be used to probe volumes on the order of cubic micrometers. The analysis of nanoindentation data is based on Hertz Theory [58-59] which describes the frictionless, linear elastic contact between two isotropic solids. Nanoindentation has been widely used in the past to determine the elastic modulus and hardness of the given sample material [3, 60-62], from the unloading portion of the load-displacement data, which is predominantly elastic. Kalidindi and Pathak [5-6] recently developed a novel approach to convert the load-displacement data measured during spherical nanoindentation into more meaningful indentation stress-strain (ISS) curves. During the course of his Ph.D., Dr. Pathak was able to validate and use this technique to obtain insights into the structure-property correlations in a wide range of materials systems, including grain interiors and grain boundaries in polycrystalline metals [5] and alloys [63-64], carbon nanotubes [65] and biological materials such as bone [66]. Since this approach forms the basis of experimental techniques used in this work, a brief summary of the methodologies and its salient features is provided in the remainder of this section.

The analysis methods in spherical nanoindentation are largely based on Hertz Theory [58-59, 67]. According to this theory, the frictionless contact between two linear elastic, isotropic solids is described by

$$P = \frac{4}{3} E_{eff} R_{eff}{}^{1/2} h_e^{3/2} \tag{2.1}$$

$$a = \sqrt{R_{eff} h_e} \tag{2.2}$$

where P is the load at elastic indentation depth h_e and a is the corresponding radius of contact. Note that the theory was developed for quadratic surfaces but in the limit of small contacts ($R_{eff} >> a$) these equations can be used to describe the contact mechanics of spherical surfaces. R_{eff} and E_{eff} are the effective radius and the effective modulus, respectively, and are defined as

$$\frac{1}{R_{eff}} = \frac{1}{R_i} + \frac{1}{R_s}, \qquad \frac{1}{E_{eff}} = \frac{1-\nu_i^2}{E_i} + \frac{1-\nu_s^2}{E_s} \tag{2.3}$$

where R is the radius, E and ν are the Young's Modulus and Poisson's ratio, and the subscripts i and s correspond to the indenter and the sample, respectively. For spherical indentation on a flat surface of an elastic-plastic material, $R_{eff} = R_i$, when the depth of indentation is within the elastic limit. However, R_{eff} increases sharply with the onset of plastic deformation in the sample, and therefore, accurate determination of a during a nanoindentation test is a challenge. This is addressed by the continuous stiffness measurement (CSM) [68] which superimposes a small-amplitude high-frequency sinusoidal load on top of the monotonically increasing load, and measuring the resulting amplitude and phase of the displacement oscillation. From this, a continuous estimate of the unloading stiffness (S) in the indentation experiment is obtained and the radius of contact, a is given by

$$a = \frac{S}{2E_{eff}} \tag{2.4}$$

The methodology to convert raw indentation data into indentation stress-strain curves can be described as a two-step process. The first step of the analysis involves identifying accurately the initial point of effective contact, or the effective zero-point, such that the initial loading segment matches the predictions of the Hertz theory. The expected relationship between the measured load ($\tilde{P}$), displacement ($\tilde{h}$) and stiffness (S) for spherical nanoindentation is expressed as

$$S = \frac{3P}{2h_e} = \frac{3\left(\tilde{P} - P^*\right)}{\tilde{h} - h^*} \tag{2.5}$$

where P^* and h^* denote the load and the displacement values at the point of effective contact. Linear regression is used to determine the values for P^* and h^* that provide the best-fit for the expected relation (Eq. 2.5) between the measured load, displacement, and stiffness signals [7].

Figure 2.6 shows an example of the regression analysis performed to identify the values of P^* and h^* for data obtained from spherical nanoindentation –on high purity aluminum. For the selected test, the load signal was shifted by 0.062 mN and the displacement signal by 11.2 nm. The spherical indenter used in this study had a radius of 100 microns. The points of initial contact as identified by the default procedure in the nanosuite software (*C1*) and by this analysis (*C2*) are displayed in the inset on Figure 2.7a. After these small shifts, the resulting load-displacement curves in the initial elastic loading segments were consistent with the trends predicted by Hertz's theory, and estimated the Young's moduli of aluminum to be 68 GPa. These values are in very good agreement with reported values in the literature from other testing methods [69].

In the second step of the analyses, the ISS curves were extracted from the raw data (corrected for the initial point of effective contact) by recasting Hertz theory for frictionless elastic contact between the sample and a spherical indenter as

$$\sigma_{ind} = E_{eff}\,\varepsilon_{ind}\,, \qquad \sigma_{\mathrm{ind}} = \frac{P}{\pi a^2}\,, \qquad \varepsilon_{\mathrm{ind}} = \frac{4h_e}{3\pi a}\,, \tag{2.6}$$

where σ_{ind} and ε_{ind} denote the indentation stress and strain, respectively and a is the

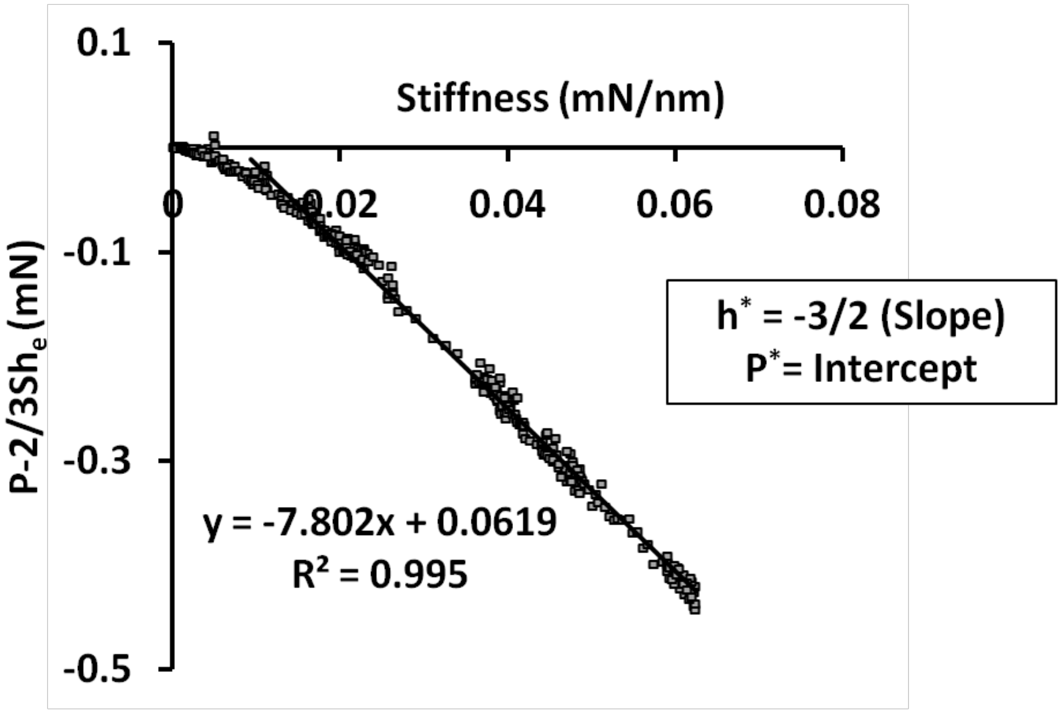

Figure 2.6: The identification of the effective zero-point using the new method. A linear regression analysis of the straight line portions of the curves shown above yields estimates of the effective zero-load and zero-displacement that make the data consistent with Hertz's theory.

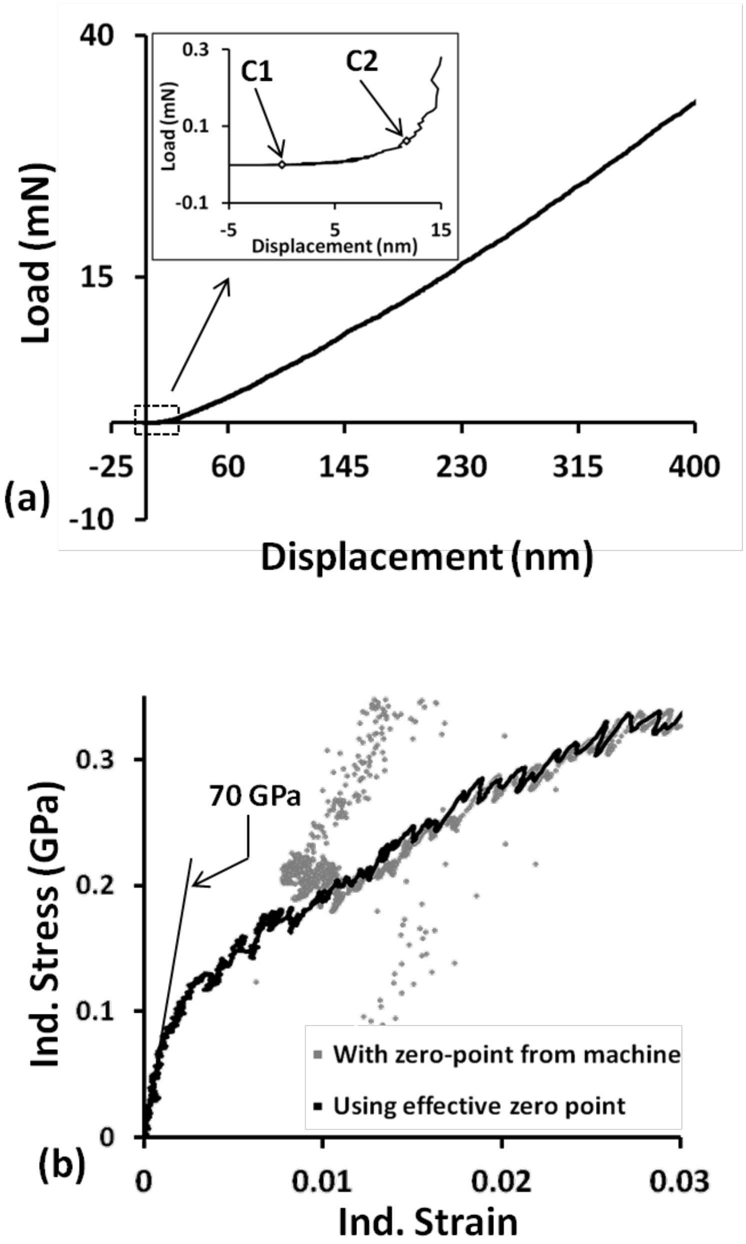

Figure 2.7: The measured (a) load-displacement curve and the extracted (b) indentation stress-strain curve for aluminum are shown here using two different estimates of the zero-point. The use of the zero-point established by the machine (C1) results in an unexplainable spike in the initial elastic loading portion of the curve (in grey). When the effective zero point (C2) is used, much better indentation stress-strain curve is obtained (in black).

contact radius at load P and elastic indentation depth h_e. In the elastic-plastic regime of deformation, beyond the linear elastic portion of the stress strain curve, indentation strain is defined in terms of the total indentation depth (h_t), (i.e. h_t replaces h_e in the definition of indentation strain in Eq. (2.6)) and the linear relationship between the indentation stress and the indentation strain is no longer valid. A representative of load-displacement curve obtained from spherical nanoindentation on pure aluminum and the corresponding indentation stress-strain are shown in Figure 2.7. The grey markers in Figure 2.7(b) represent the indentation stress-strain curve obtained if the zero point as determined by the machine is used and shows an unexplainable spike in the initial regions. When the effective zero point, determined as explained above and demonstrated in Figure 2.6 is used, the spike disappears and the indentation stress-strain curve shows a very distinct linear elastic segment, followed by an elastic plastic transition and post elastic hardening.

One of the challenges in using the methods described above to characterize the anisotropic behavior in metals is that the analysis is based on Hertz theory for analysis of nanoindentation data assumes an isotropic elastic material response. However, as shown by Vlassak and Nix [70], the elastic indentation response for a variety of high symmetry orientations of a cubic crystal can be adequately captured using a modified form of the Hertz theory. Spherical nanoindentation testing has recently been employed to successfully capture the crystal level plastic anisotropy [63] in Fe-3%Si. A similar approach will be used in this work.

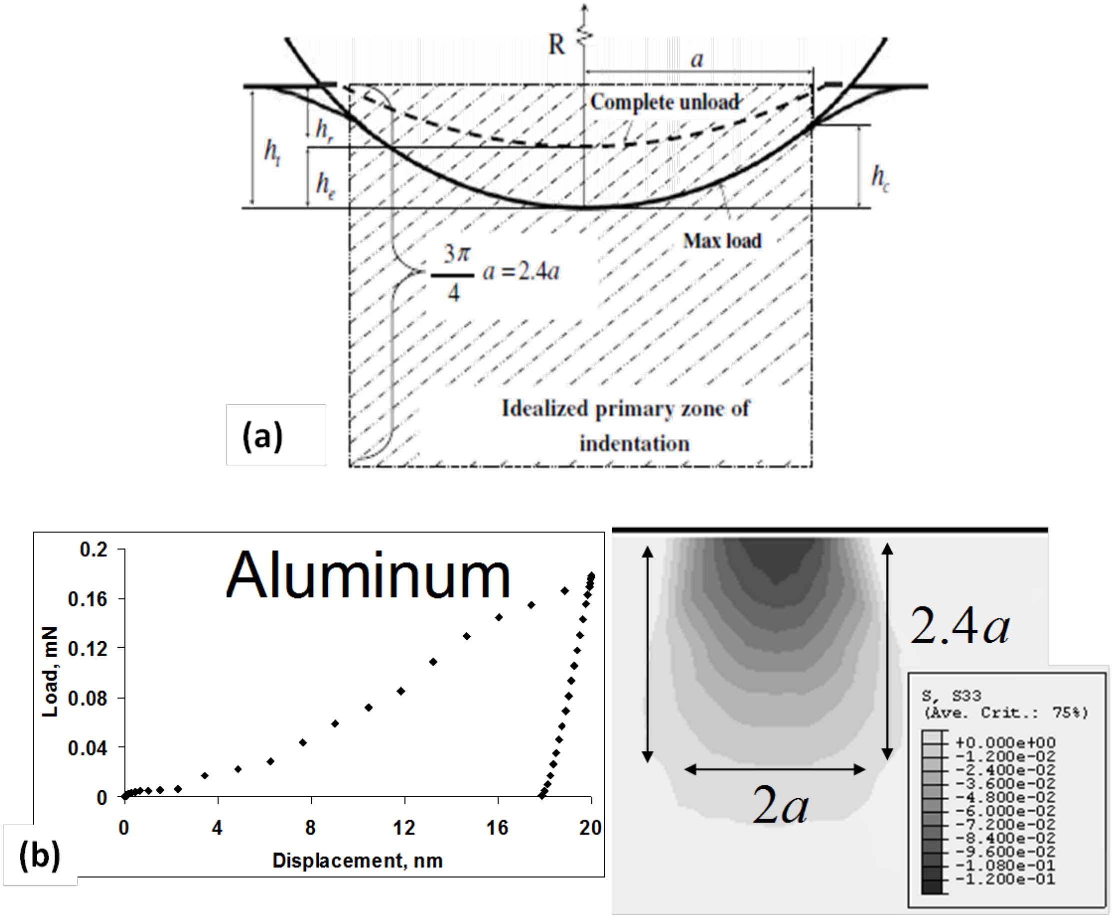

Figure 2.8: (a) Schematic of a spherical nanoindentation showing the primary zone of indentation. (b) The predicted load-displacement curves and stress contours in the finite element simulations for Aluminum. The indentation zone in the simulations extends approximately to a depth of about 2.4a.

Traditionally, the unloading portion of the load-displacement curve has been used to extract information about the material behavior, since the unloading segment is predominantly elastic and Hertz equations can be applied. Note that the additional deformation imposed during nanoindentation can alter the local microstructure and properties of the material and hence the properties extracted from the unloading portion of the curve may not represent the properties of the virgin material. Therefore, it is extremely important to extract the material properties from the initial loading portion of the nanoindentation data. Also, most nanoindentation testing is carried out using sharp tips which give rise to very steep stress gradients. However, spherical tips generate stress gradients that are less sharp, and the initial elastic segment is relatively longer, making the application of Hertz theory to the initial loading segment relatively easier. Finally, it should be noted that the indentation strain definition used in Eq. (5) is substantially different from the definition used in many prior studies [71-72]. This new definition of indentation strain has been validated in many recent studies both using numerical simulations [73] and experimental measurements [5, 63-66, 74] and is tantamount to idealizing the primary indentation zone to be a cylinder of diameter *2a* and height *2.4a*, as shown in the schematic in Figure 2.8(a). Here, indentation is idealized as being equivalent to compressing a cylinder of original height *2.4a*, by a height of h_e . The predicted load-displacement curve and the stress field obtained from finite element simulation [73] corresponding to an indentation depth of 20 nm are shown in Figure 2.8(b) and (c) respectively and it is clearly seen from the figure that the indentation zone extends approximately to a length of about *2.4a*, justifying the new definition of the indentation strain.

Using a spherical indenter tip and extracting information from the initial loading segment has very significant advantages over the methods more commonly used in literature, but comes with its own set of challenges. Since the new approach uses the initial loading segment to extract material properties finding the accurate point of initial contact is very critical as even deviations of the order of a nanometer or tens of micro-

Newtons produces an unexplainable spike in the elastic portion of the indentation stress-strain curve. Therefore the demand for a well polished, smooth surface, free of an oxide film and any residual effects from sample preparation is even higher and hence sample preparation is a challenge. The importance to sample preparation and its effects on indentation stress-strain curves is detailed in [74]. Another very important aspect of nanoindentation, for extracting reliable indentation stress-strain curves is the continuous stiffness measurement (CSM). As mentioned earlier in this section, the calculation of the radius of contact (*a*) at every point on the loading segment is done with the help of the CSM. Therefore, before we use nanoindentation testing to measure the local mechanical properties, the effect of CSM on the nanoindentation measurements need to be understood, particularly because there have been reports [75-77] that the use of CSM alters the mechanical response measured by nanoindentation testing . This is addressed on Chapter 3.

CHAPTER 3

EFFECT OF CONTINUOUS STIFFNESS MEASUREMENT ON THE SPHERICAL NANOINDENTATION DATA

3.1 Introduction

The continuous stiffness measurement (CSM) [68] produces a continuous estimate of the unloading stiffness in the indentation experiment by superimposing a small amplitude high-frequency sinusoidal load on top of the monotonically increasing load, and measuring the resulting amplitude and phase of the displacement oscillation. The potential of CSM to improve dramatically the reliable extraction of meaningful mechanical properties from the measured load–displacement data in the nanoindentation experiments is well documented [4, 60, 62, 78-79]. Furthermore, as mentioned in the previous section CSM is central in the nanoindentation data analysis procedures to convert raw nanoindentation load–displacement data into indentation stress–strain (ISS) curves. Since the magnitude of the imposed oscillations is very small compared with the overall load on the sample, it is generally assumed that this additional dynamic loading does not alter the quasi-static mechanical response of the sample. However, recent studies on some metallic materials [75-77, 80] and visco-elastic materials [76, 81-82], using a sharp-tip indenter have reported a significant influence of the CSM on the values of the measured mechanical properties. Cordill et al. [12] suggested that the additional oscillations aid in dislocation nucleation, resulting in the softening behavior. They also reported [76] that the CSM affects both the number of pop-ins during a nanoindentation test and the stress at the start of the pop-in. Given the critical role of CSM in the analysis of the indentation measurements [5, 63] used in this work, as a first task, the precise influence of CSM on the ISS responses extracted from spherical nanoindentation data was systematically investigated.

Although sharp-tip indenters have been employed widely in prior studies [60, 76-77, 80, 83], there is now significant interest in the use of spherical indenter tips because of their recent success in producing reliable ISS curves that include the initial loading segment, the post-yield response and the unloading segment [5, 65, 72, 84]. Examining the indentation data in the form of ISS curves provides better insights into the microscale mechanical response in the sample (suitably averaged over the indentation zone). This chapter reports a thorough investigation of the consequences of changes in the amplitude (h_{rms}) and the frequency (ν) of the superimposed oscillations in the CSM on the resulting ISS curves obtained using a spherical indenter tip. This was deemed to be a critical first task of this thesis work. Section 3.2 details the errors associated with using the CSM and the suggested corrections to compensate for the errors. The details of the materials used and experimental methods are provided in Section 3.3. Section 3.4 describes the experimental observations and discusses the results of this work. The concluding remarks are presented in Section 3.5.

3.2 Errors in the Raw Data

The main sources of the errors in the raw data due to the superimposed oscillations in the CSM are described in detail in Ref. [75] for nanoindentation testing using a Berkovich indenter. In summary, Pharr et al. [75] consider two major sources of errors and a schematic illustrating the sources of these errors is presented in Figure 3.1.

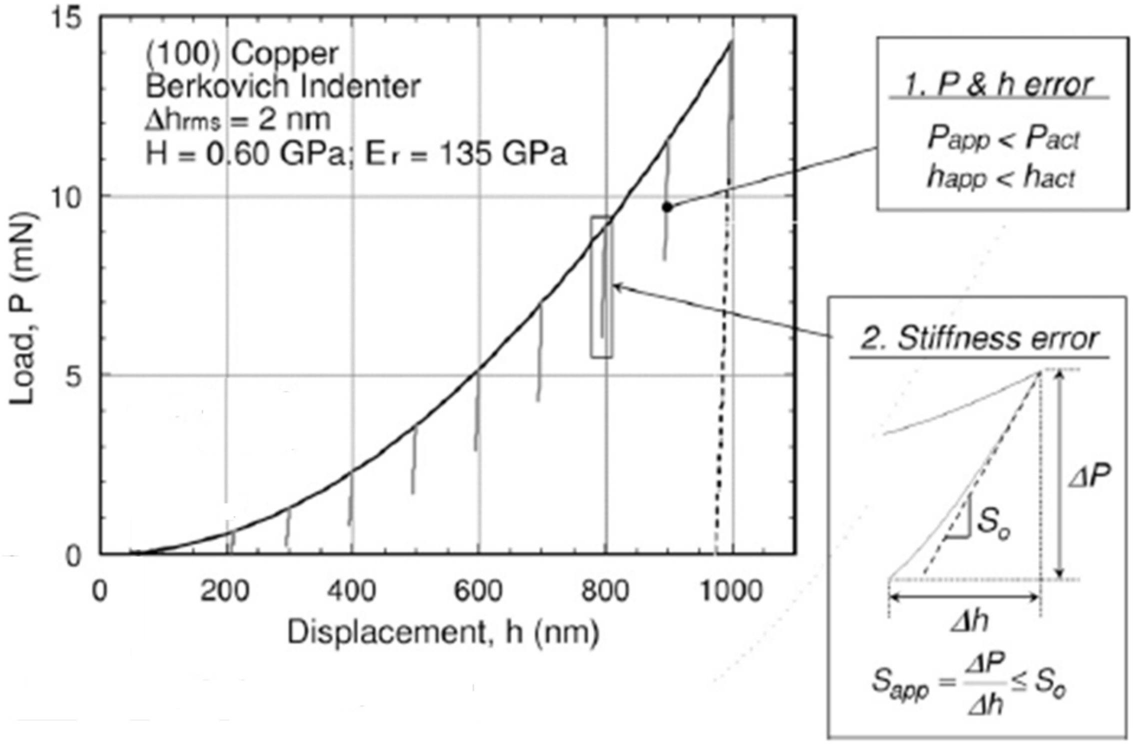

Figure 3.1: Schematic illustration of the proposed sources of measurement errors in the nanoindentation data due to the Continuous Stiffness Measurement (CSM) [75]

First, the load and the displacement are underestimated with the use of CSM, because the machine records average values. However, the material being tested actually experiences the load and displacement corresponding to the maxima of the superimposed oscillations. This error in the recorded data can be easily corrected using the following equations:

$$P_{act} = P_{app} + \frac{\Delta P}{2} \quad \text{or} \quad P_{act} = P_{app} + \sqrt{2}\Delta P_{rms} \tag{3.1}$$

$$h_{act} = h_{app} + \frac{\Delta h}{2} \quad \text{or} \quad h_{act} = h_{app} + \sqrt{2}\Delta h_{rms} \tag{3.2}$$

where *P* and *h* refer to the load and displacement signals, respectively, and the subscripts act and app refer to the actual values experienced by the sample and the apparent values recorded by the machine, respectively. *ΔP* and *Δh* are the peak-to-peak load and displacement ranges, respectively, associated with the superimposed oscillations. The corrections are easy to apply, since the machine provides the *rms* values of the oscillating signal.

The second source of error is associated with the measurement of the stiffness *S*. The apparent stiffness S_{app} reported by the machine is essentially the ratio of the peak-to-peak amplitudes of the load and displacement signal. However, from Hertz theory [58-59], it is known that the relationship between load and displacement is not linear, even in the elastic regime, and therefore this measurement underestimates the stiffness at peak load. Following the methodologies described in Ref. [75], the unloading curve for spherical nanoindentation was modeled, and the following expression was derived to correct for this error:

$$S_{act} = \frac{1}{\sqrt{2\pi}} \frac{P_{\max}}{\Delta h_{rms}} \left(\frac{1}{K}\right)^{1/m} \left[1 - \left(1 - \frac{2\sqrt{2}\Delta h_{rms} S_{app}}{P_{\max}} \right)^{1/m} \right] \tag{3.3}$$

where S_{act} is the corrected stiffness signal, K is a constant whose value is a function of the indenter geometry ($K = 0.6524$ for spherical nanoindentation), and $m = 3/2$ for the case of spherical nanoindentation. A third potential error discussed in Ref. [75] arises from the loss of contact between the indenter tip and the sample at low loads (during the dynamic oscillations). This is not considered here because the protocols used for determining the effective zero point (explained in Section 2.4) indirectly addresses this issue.

3.3 Experimental Details

3.3.1 Materials Used

The materials used in this study are (i) high-purity, fully annealed, aluminum (99.999%), (ii) high-purity deformed aluminum, and (iii) fused silica. The fully annealed aluminum samples were selected for this study for two main reasons: (i) they exhibit a fairly high modulus-to-strength ratio (~3500), which in prior studies [75] was shown to result in a greater influence of CSM on the measured properties from the indentation experiments; (ii) these samples exhibit relatively large initial loading segments, followed by distinct pop-ins (also referred to as displacement excursions) [74, 85-88], allowing the role of CSM on the pop-in stress levels to be investigated clearly. The deformed aluminum samples were selected to investigate the role of CSM on ISS curves measured in samples with pre-existing dislocations, which is known to suppress the pop-ins [74]. All comparisons were done among tests carried out in the same grain (in the bulk of the grain, away from visible grain boundaries), thereby avoiding the complications that arise from the influence of the lattice orientation on the measured ISS curves [63]. Fused silica samples were selected to serve as a control, as they exhibit a much lower modulus-to-hardness ratio (~7) and no pop-ins.

3.3.2 Surface Preparation

The aluminum samples were cut out from a heavily rolled block of high-purity aluminum (99.999%), and annealed at 640 ºC for 72 hrs in order to grow the grains, so that the average grain size was ~3 mm. Because of the large grain size, all the tests reported in this study could be performed within a single grain, far away from the grain boundaries. A sample was then deformed by plane strain compression in the channel-die to achieve a 20% reduction in height. The deformation was carried out at room temperature, and care was taken to ensure that all sample surfaces in contact with the die and the punch were lubricated with a 0.1-mm-thick Teflon tape. All aluminum samples were prepared by mechanical grinding using Si–C papers followed by polishing with 3 μm and 1 μm diamond suspensions. As a final step, the samples were electropolished [89] for 45 s using a voltage of 12 V in a mixture of perchloric acid (10%) and methanol (90%) at -20 º C. The fused silica sample was tested as-received from the manufacturer.

3.3.3 Nanoindentation Tests

All nanoindentation tests were performed using a MTS nanoindenter XP® equipped with the CSM attachment. A set of nine indents were performed without the CSM on each of the samples mentioned earlier to serve as the reference response for comparisons. In addition, nanoindentation tests including the CSM were carried out by varying the frequency and amplitude of the superimposed oscillations at four different test conditions: 45 Hz–2 nm, 45 Hz–1 nm, 10 Hz–2 nm and 10 Hz–1 nm. In this convention for labeling the tests, the first number specifies the frequency, and the second number specifies the displacement amplitude for the superimposed oscillations. A set of at least nine indents were performed at each test condition listed above, in order to document the repeatability of the measurements. All tests were carried out such that the strain rate, defined as $\dot{h}/h$ by the MTS software, remained at a constant value of 0.05 s^{-1} during the loading segment, unless specified otherwise.

For the tests on annealed aluminum, spherical indenter tips of 1 μm and 100 μm radii were used. It was shown in prior studies [74] that the larger indenter tip radius results in a smaller pop-in. The use of two indenters with different tip radii allowed for a critical evaluation of the role of CSM on the measured ISS curves. For the indentations on the deformed sample, where there are no pop-ins, the 100 μm indenter tip was used. Tests on fused silica were carried out with the 1 μm spherical indenter tip. The 100 μm indenter tip could not be used on fused silica samples, because it does not produce appreciable plastic deformation, even at indentation depths of 1000 nm.

3.4 Experimental Observations and Discussion

3.4.1 Load – Displacement Data

Representative load–displacement data for indentation tests carried out on the different test samples are shown in Figure 3.2. Indentation tests conducted with the 1 μm indenter tip on the pure aluminum samples that included the CSM resulted in load–displacement curves that were shifted down compared with the tests conducted without the CSM (see Figure 3.2(a)). This observation is consistent with the previous reports in the literature for tests on other metal (copper and nickel) samples [75-76] with a sharp indenter tip. The effect is the highest for tests carried out with the CSM at 45 Hz–2 nm. The tests carried out at 10 Hz–2 nm, 45 Hz–1 nm and 10 Hz–1 nm CSM conditions show progressively less softening. Thus, the tests carried out with CSM at 10 Hz–1 nm produced data closest to the data obtained from the tests without the CSM. As expected, these effects are most prominent for indentation tests carried out on annealed aluminum with the 1 μm spherical tip. For tests carried out with the 100 μm spherical tip on annealed aluminum (not shown here) and deformed aluminum (see Figure 3.2(c)), the effect was not discernible. Tests on fused silica with the 1 μm indenter tip (see Figure 3.2(e)), in contrast, showed little effect of the test method on the raw nanoindentation load–displacement data. The load and displacement data were corrected using Eq. 3.1 and 3.2 in order to account for the errors explained earlier in Section 2. It is seen that the load–displacement measurements corrected as indicated in Section 2 significantly improved the agreement for data between the different CSM test conditions for the first set (see Figure 3.2(b)). The corrections for tests with the 100 μm indenter tip (Figure 3.2(d)) were less significant, and no improvements are noticeable.

Indentation measurements for pure aluminum with a relatively high elastic modulus-to-hardness ratio showed a significant effect of the CSM, while fused silica with a relatively low modulus-to-hardness ratio showed negligible effects. This dependence on the modulus-to-hardness ratio was reported previously by Pharr et al. [75] for sharp indenters. It is concluded from Figure 3.2 that the corrections for the load and displacement signals are indeed important for materials with a high modulus-to-hardness ratio, especially when small–radii spherical indenters are used.

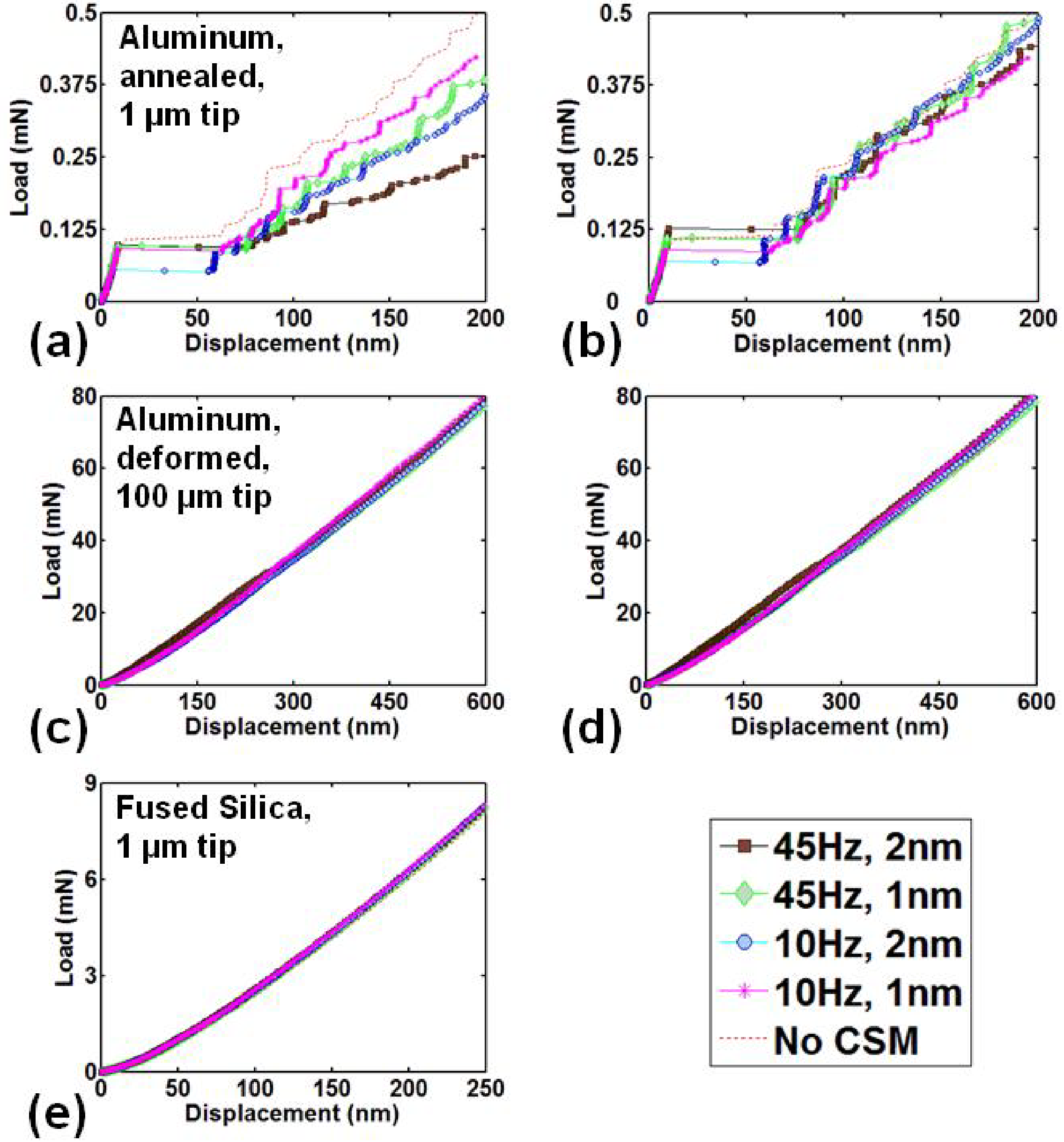

Figure 3.2: Influence of CSM on the indentation load-displacement data: (a) Raw load-displacement data for measurements conducted using a 1 μm spherical tip on ultra-high purity aluminum; (b) Corresponding corrected data; (c) Raw load-displacement data corresponding to measurements conducted using a 100 μm spherical tip on 20% deformed ultra-high purity aluminum (d) Corresponding corrected data; (e) Raw load-displacement data for nanoindentation on fused silica using the 1 μm spherical tip.

3.4.2 Stiffness – Displacement Data

The stiffness – displacement data corresponding to the tests shown in Figure 3.2 are plotted in Figure 3.3. Figure 3.3(a) and (b) displays the apparent stiffness (S_{app}) and the corrected stiffness (S_o) as a function of the total indentation displacement for the different test conditions on annealed aluminum with the 1 μm spherical tip. It is generally seen that the values of the corrected stiffness are slightly higher. It should be noted that the apparent stiffness is computed by the system as a simple ratio of increment in load over the increment in displacement, whereas the analytical relationship between elastic load and displacement is expected to show an exponential dependence. Consequently, the stiffness computed by the machine should be expected to underestimate the actual slope at the point of unload. No other trends are discernible because of the stochastic nature of the large pop-ins that occur in these tests. Pop-ins are a result of increased elastic stresses under the indenter tip due to the lack of active dislocation sources, followed by a strain burst resulting from the activation of new dislocation sources [74]. While for this comparison, tests that had pop-ins occurring at similar displacements and of similar size were selected, it is highly improbable to find tests where the pop-ins occur at the same depth and are of the same size. Thus, by their very stochastic nature of their occurrence, comparison among them in the current context would not be possible.

Figure 3.3(c) and (d) presents the corresponding data for the tests conducted with the 100 μm spherical tip on the deformed aluminum, where the pop-ins are absent. Here, the values for the harmonic contact stiffness at higher indentation depths are progressively lower for the tests carried out with CSM at 10 Hz–2 nm and 10 Hz–1 nm oscillations, respectively, compared with the tests carried out at 45 Hz frequency. It is

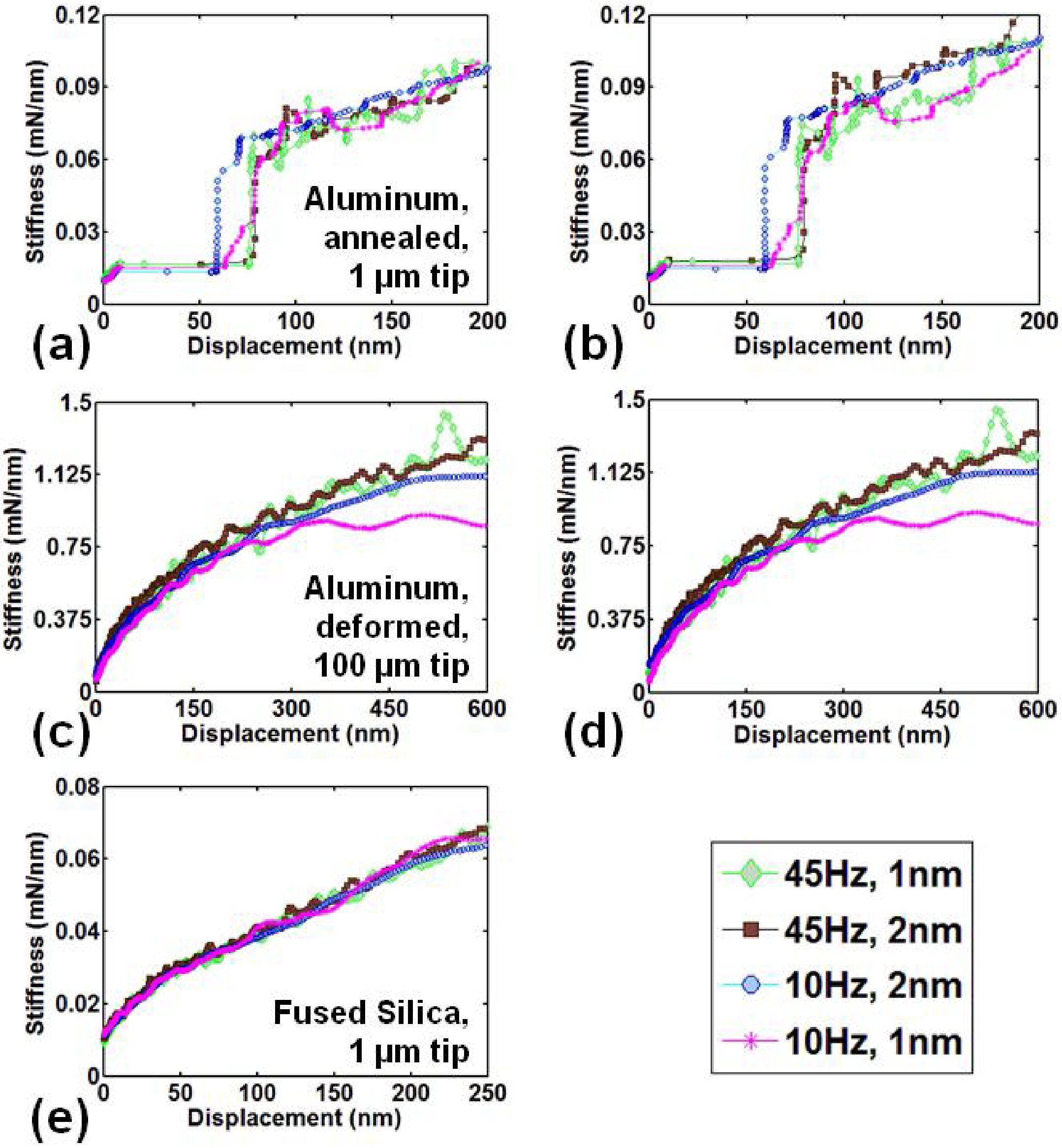

Figure 3.3: Influence of CSM on the indentation stiffness-displacement response: (a) Raw stiffness-displacement data for measurements conducted using a 1 µm spherical tip on fully annealed ultra-high purity aluminum; (b) Corresponding corrected data; (c) Raw stiffness-displacement data corresponding to measurements conducted using a 100 µm spherical tip on 20% deformed ultra-high purity aluminum; (d) Corresponding corrected data; (e) Raw stiffness-displacement data for nanoindentation on fused silica using the 1 µm spherical tip, showing little effect of the test method used except for in the level of noise.

also observed that data for both deformed aluminum and fused silica, obtained with the CSM at 45 Hz–1 nm oscillations showed higher levels of inherent noise in the stiffness signal. However, the data for fused silica showed no other effect of the test method used. Note here that the tests on the pure undeformed aluminum with the 100 lm spherical tip exhibited the same trends as the data for the deformed aluminum. The corrections described earlier (Eq. 3.3) did not bring the curves for the displacement–harmonic stiffness data with the different CSM conditions closer.

For elastic deformations, the phase angle between the displacement oscillation and the corresponding load oscillations is expected to be near zero. However, as shown in Figure 3.4, at higher indentation depths this value deviates significantly from the expected near-zero value, for the tests carried out with CSM at 10 Hz. If this deviation from near-zero values was caused by plastic deformations due to the imposed oscillations, the effect would be more pronounced for the case of CSM at 45 Hz–2 nm instead. Also, the harmonic stiffness signal for the nanoindentation tests conducted at a constant loading rate of 0.25 mN s^{-1} (the tests shown in Figures. 3.2 and 3.3 were conducted at a constant strain rate of 0.05 s^{-1}) on pure aluminum (see Figure 3.4(b) and (c)) show a much better agreement for the data obtained under different CSM conditions. Note that, while at the early stages of the tests the two methods produce similar displacement rates, for the tests conducted at constant strain rates, the displacement rate is constantly increasing and, at higher indentation depths, these tests proceed much faster. The decrease in the stiffness values at higher indentation depths observed for these tests is most likely an artifact of the machine dynamic control system. The higher noise levels

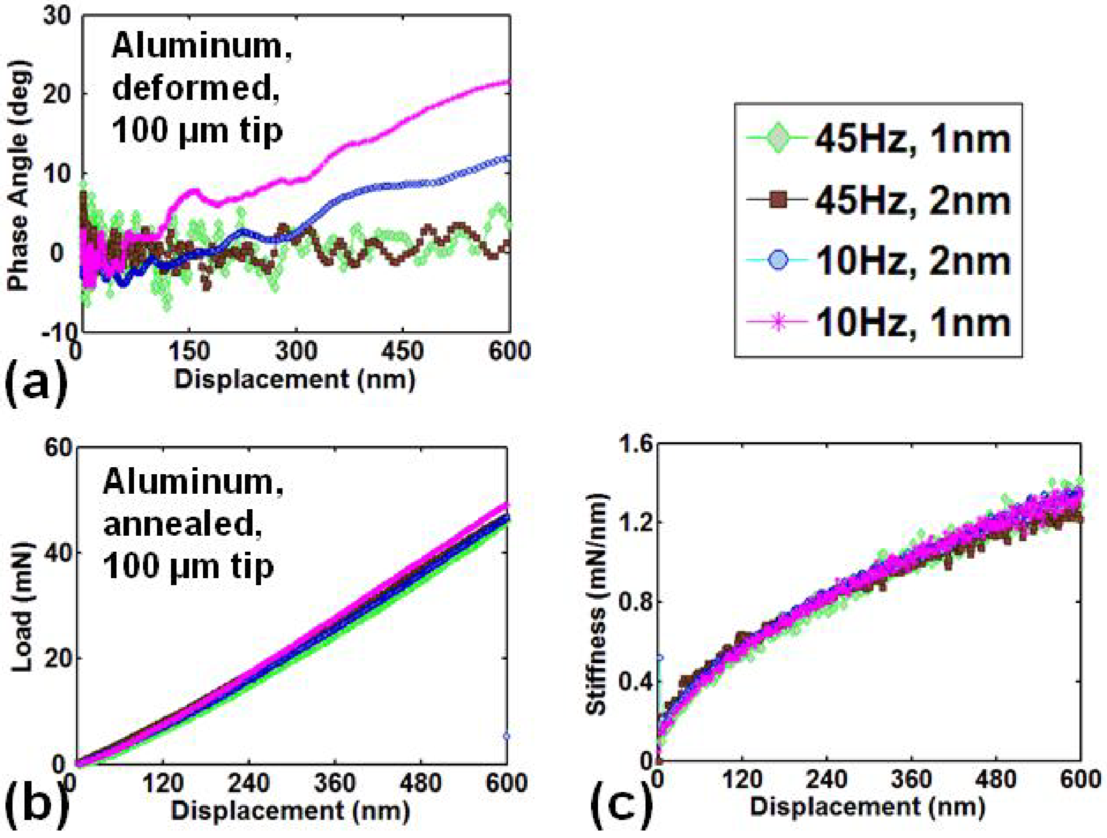

Figure 3.4: (a) Variation of the phase angle between the harmonic load and harmonic displacement, for the various CSM conditions, on 20% deformed high purity aluminum samples with the 100µm indenter tip showing a significant deviation from the expected near zero phase angle for purely elastic load cycles. Representative (b) load displacement data (c) corresponding raw stiffness-displacement data for tests carried out at a constant loading rate, on fully annealed high purity aluminum samples with the 100µm indenter tip are shown. The number of data points in the initial elastic segment was too small to allow for the extraction of indentation stress strain curves. Unlike the data shown in Fig. 1 and Fig. 2, there tests carried out at a constant loading rate do not show any effects of the CSM.

3.4.3 ISS Data

for the stiffness signal obtained for the 45 Hz–1 nm CSM condition may be reconciled by the fact that this test condition presents the most difficult case for the feedback control to accurately maintain low-amplitude– high-frequency oscillations. While instrumentation and controls are outside the purview of this paper, it is important to keep in mind that these observations help conclude that the effects of CSM observed here do not reflect material behavior.

ISS curves, extracted following the methods described in Section 2.4, for the raw data presented in Figures 3.2 and 3.3 are shown in Figure 3.5. In the ISS curves, pop-ins manifest as a strain burst at extremely high stresses, followed by an unloading segment. The large pop-ins in the data corresponding to the tests on annealed aluminum with the 1 μm spherical tip mask the elastic–plastic transition and make it difficult to compare the post-elastic deformation behaviors under the various imposed test conditions. As mentioned in the previous section, the pop-ins are stochastic in nature and hence, in this context, a comparison of ISS curves with very large pop-ins is not very meaningful. The pop-ins disappear for the tests carried out on deformed aluminum using the 100 μm indenter tip, as shown in Figure 3.5(c) and (d). In this case, the post-elastic stress values are very similar for the tests done with CSM at a 45 Hz oscillation frequency. However, the tests carried out using the 10 Hz– 2 nm and 10 Hz–1 nm CSM conditions show pronounced post-elastic hardening, with the effect being most severe for the latter. This is the result of the lower stiffness values recorded for these test conditions. As explained in the previous section, this is only an artifact. Since both stress and strain are inversely related to the radius of contact and hence inversely related to the stiffness [5], lower

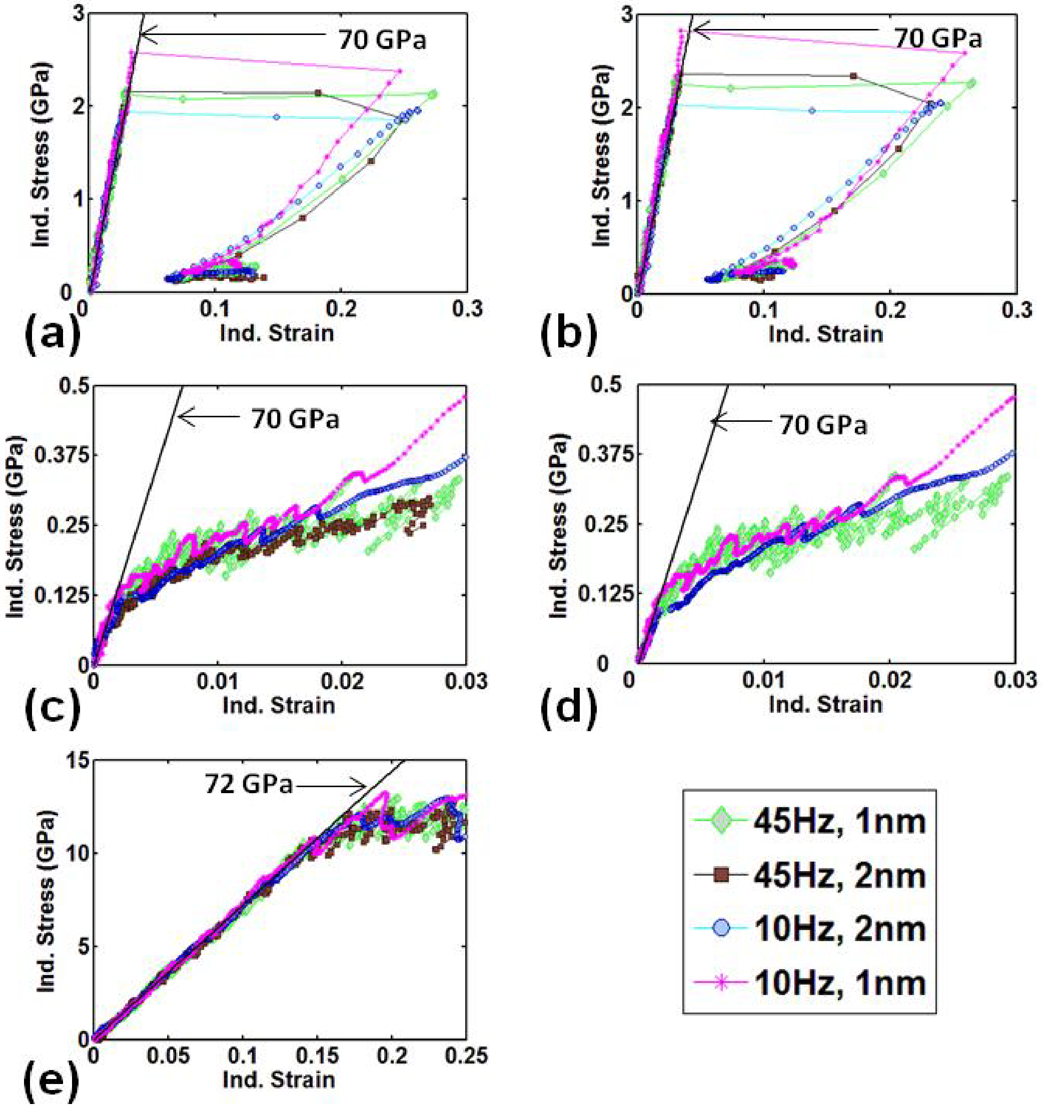

Figure 3.5: of CSM on the Indentation stress-strain curves: (a) ISS curves corresponding to the measurements conducted using a 1 μm spherical tip on fully annealed ultra-high purity aluminum; (b) ISS data for the corresponding corrected data; (c) ISS data for tests on 20% deformed ultra-high purity aluminum using a 100 μm spherical tip; (d) ISS data for the corresponding corrected data (Note that for tests with 45Hz – 2nm oscillations, most of the initial elastic segment is lost while correcting for the stiffness signal, and hence the indentation stress-strain curve could not be extracted); (e) ISS curves extracted using the raw nanoindentation data for tests on fused silica using the 1 μm spherical tip.

stiffness values result in increased values of both, with the effect being more pronounced for the magnitude of stress. Also, as in the case of data for the stiffness vs. displacement data, the ISS data for both aluminum and fused silica is noisiest for the tests carried out at the 45 Hz–1 nm test condition.

The various corrections to the raw data sets (described in Eq. 3.1–3.3) appear to have a smaller effect on the ISS curves compared with their effect on the raw data. This suggests that the corrections to individual signals appear to negate each other to some extent in the computation of the ISS values. Also, note that most of the initial elastic segment for the indentation of deformed aluminum with the 100 lm indenter tip using the 45 Hz–2 nm CSM condition is lost while correcting for the stiffness signal using Eq. (3.3). In summary, the tests done at 10 Hz CSM frequency produced dubious data sets, while the tests carried out at 45 Hz–1 nm CSM condition were noisy, and the corrections for the raw data were not very helpful. Therefore, the corrections can be skipped altogether, and the CSM signal at 45 Hz–2 nm oscillations seems to be the most reasonable choice for nanoindentation testing.

It has been proposed by Cordill et al. [77] that the added energy associated with the superimposed oscillations assists dislocation nucleation, which causes the observed softening in the nanoindentation response using the CSM. In the present work, the nanoindentation response, in terms of the effects of the CSM, is very similar for the data obtained for tests on annealed aluminum (data not shown) and the deformed aluminum using the same spherical tip. Prior plastic deformation or, in other words, the presence of active dislocation sources did not change the behavior of aluminum during nanoindentation under the CSM. The changes in the response, due to the presence of the

CSM signal seems to be related only to the machine dynamics and the data acquisition systems.

Cordill et al. [76, 80] also reported that the occurrence of the pop-in (or onset of plastic deformation) is affected by the displacement amplitude and oscillation frequency of the superimposed oscillations. Cordill et al. [80] reported one major excursion for tests done in the absence of the superimposed oscillations in single-crystal nickel, while staircase yielding (many small displacement excursions) was reported for nanoindentation tests with the CSM. Also, Cordill et al. [76] reported an increase in the stress at the start of the pop-in by a factor of 3 for indentations done without the CSM compared with those done with the CSM. Note that sharp indenter tips were used in these previous studies.

The pop-ins observed in the present tests on annealed aluminum with a 1 μm spherical nanoindenter tip were highly stochastic. A set of 12 nanoindentation measurements for each of the CSM test condition were used to perform the statistical analysis. The two-factor analysis of variance (ANOVA) revealed that no significant differences ($p > 0.05$) exist between the data (in terms of displacement and stress at the start of the first pop-in) when comparing tests done under the different CSM conditions to one another and also compared with tests done without the CSM. Note here that the data used for the ANOVA were corrected using Eq. 3.1–3.3 to account for the effects of the CSM. However, using the raw data for the ANOVA did not significantly alter the findings.

The present authors' primary concern in this work was to minimize any effects that the CSM signal might have on the nanoindentation response of the test material, while ensuring that the stiffness signal obtained was reliable. Therefore, only data obtained at the default CSM test conditions (oscillation frequency and amplitude of 45 Hz and 2 nm, respectively) were compared with the oscillation frequency and amplitude that are lower than the default values. It has also been recommended by Pharr et al. [75] that reducing the harmonic displacement amplitude would improve the measurements. In this work, comparing data from different tests conditions obtained using only two values for the oscillation frequency (45 Hz, 10 Hz) and for oscillation amplitudes (2 nm, 1 nm) showed that the data obtained at a lower oscillation amplitude and frequency was unreliable. Lowering the oscillation frequency and/or amplitude of the CSM signal further would most likely to make it worse.

3.5 Conclusions

In this chapter, the effect of the CSM on the indentation response in pure aluminum and fused silica during spherical nanoindentation was critically examined. While fused silica showed little effect of the superimposed oscillations, the data for pure aluminum obtained under the different CSM conditions differed significantly. The amplitude and frequency of the superimposed oscillations in the CSM affected the harmonic stiffness signal most significantly, owing to the machine dynamics and the characteristics of the data collection system. The phase angle between the harmonic displacement and harmonic load is expected to be near zero for elastic oscillations and is used here as an indicator for questionable measurements of the stiffness. The values for the harmonic stiffness are unreliable at lower oscillation frequencies, and the noise levels are very high for low oscillation amplitudes. Therefore, 45 Hz–2 nm oscillations in the

CSM during nanoindentation testing appears to be the best option. Also, the use of CSM did not significantly affect the pop-in response measured in spherical indentation.

CHAPTER 4

MATERIALS, MACROSCALE PROCESSING AND METALLOGRAPHY

High Purity (99.999%) aluminum is utilized in the different experiments described in the remainder of this dissertation. Fully annealed, large grained samples of aluminum are used to establish and validate methods to extract indentation yield point data from nanoindentation experiments as well as to characterize plastic anisotropy of aluminum in the undeformed state. Samples deformed by plane strain compression, to increasing levels of strain are used in the subsequent steps of the study. One of the reasons for choosing pure aluminum was that it exhibits very little elastic anisotropy (a = 1.22) [69]. This is desirable since the data analysis protocols for nanoindentation are based on Hertz theory, which describes the frictionless contact behavior of two elastically isotropic surfaces. For materials with a higher level of elastic anisotropy, a modified form of Hertz theory can be used [70]. This theory predicts the reduced modulus (*Eeff* - defined in Eq. 2.3) to be in the range of 68.8 - 70.6 GPa for pure aluminum. Therefore, there is very little effect of the crystal orientation on the elastic modulus at the indentation site. The oxide film on aluminum is very thin, making its contribution to the indentation response negligible. Furthermore, plastic deformation at room temperature is known to occur in fcc Aluminum only along <110> directions on the (111) planes. Absence of solute eliminates complications due to segregation and precipitation during plastic deformation. Also, in the fully annealed condition, these aluminum samples can be produced to exhibit extremely large grain sizes (of the order of several millimeters).

Such samples are ideal for indentation studies as they allow us to investigate individual grains and specific grain boundaries while avoiding contributions from the neighbors.

All test samples were sectioned out from a heavily rolled block of high purity aluminum using electric discharge machining (EDM) and annealed for 72 hours at 640˚C in order to obtain large grains in the fully annealed state. Another advantage of heat treatment after cutting the samples to final size is that as the grains grow very large after recrystallization, the grain boundaries, very close to the surfaces, will then be migrating very slowly will have time to orient themselves at right angles to the free surface. This, together with the large grain size means that when indentation tests are done reasonably away from the grain boundaries visible on the 2-D surface scan, the probability of encountering a grain boundary under the surface, close to/intersecting our interrogation volume is very low. This allowed for clean experiments and aided in the interpretation of the experimental data.

Some of the annealed samples were then deformed in a channel die at room temperature using an Instron screw driven testing machine at Drexel University to produce height reductions of 10% (light deformation), 20% (moderate deformation) and 40% (heavy deformation) that correspond to true strains of -0.11, -0.22 and -0.51 respectively. Care was taken to ensure that all sample surfaces in contact with the die and the punch were lubricated with a 0.1 mm thick Teflon tape to minimize friction. The compression itself was carried out in multiple small steps and the sample was lubricated between steps.

The samples were mounted in epoxy and prepared by mechanical grinding using SiC papers followed by polishing using the 9 µm-, 3 µm and 1 µm diamond suspensions on a commercial grinding and polishing machine. Since the material property information is to be extracted from the initial segment of the indentation data, a good sample surface, free of any damaged/deformed surface layer or scratches is critical [69]. In order to ensure reliable and reproducible data from nanoindentation experiments, electropolishing was used as the final sample preparation step. The samples were electropolished using a mixture of 100 ml perchloric acid and 900 ml methanol at -20 °C at a voltage of 11.8-12 V for 1-2 min.

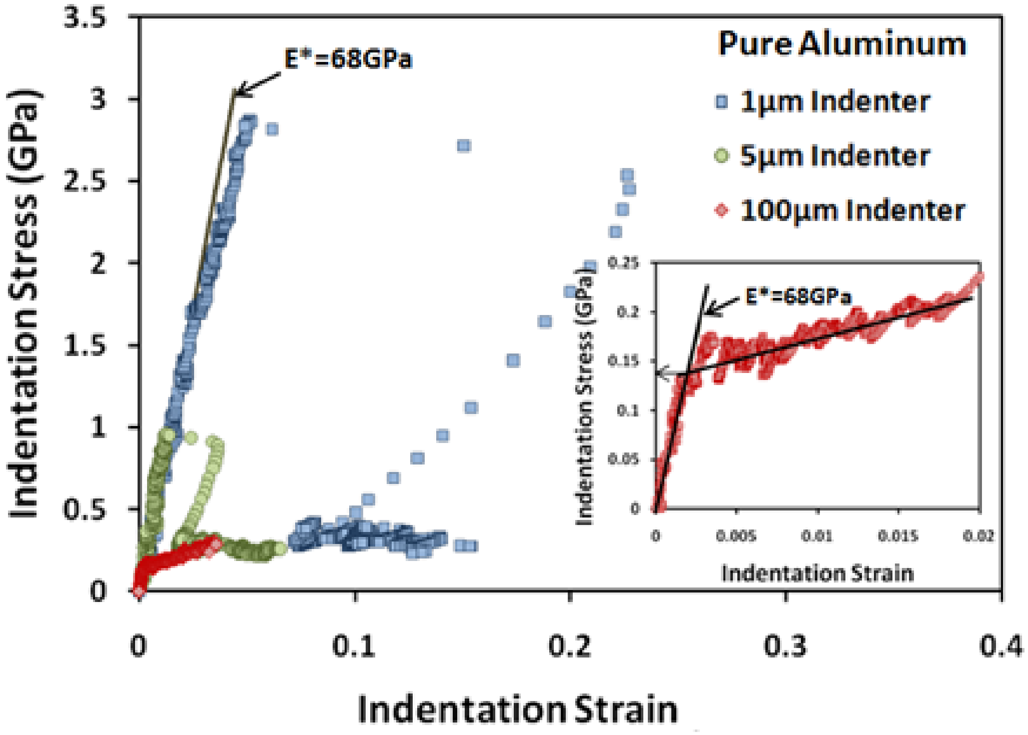

Figure 4.1: Effect of indenter size- The indentation stress–strain curves obtained using spherical tips of three different indenter tip sizes (1 µm, 5 µm, and 100 µm radii). Note that the pop-in is largest for the test performed with the 1 µm tip and that for the largest (100 µm) tip, its altogether absent.

Grain orientation maps for the prepared sample surface were obtained using orientation imaging microscopy (OIM), which is based on the automatic indexing of electron back-scatter diffraction (EBSD) patterns [90]. Orientation at each point was denoted using the Bunge-Euler angles [91], an ordered set of three angles (φ1,Φ, φ2), which describe the rotations for the transformation from the sample reference frame to the crystal reference frame. The grains tested on the different sample surfaces were numbered for convenience and will be referred to using their assigned grain numbers. The grain maps were used to identify regions of interest to perform the indentation testing. After the indentation tests were performed, the regions of interest were imaged again in the SEM using OIM, to confirm the location of the indents and determine the local crystal orientation at the indentation site.

Nanoindentation tests were then carried out at pre-selected locations on these samples using the MTS nanoindenter XP® or the Agilent G200® systems equipped with the CSM attachment. Care was taken to ensure that the indents were placed well away from the grain boundaries. Using the ISS data, the indentation modulus of the test specimen can be obtained from the slope of the elastic loading part of the curve. However, in order to be able extract indentation yield stress values from the ISS data, the displacement excursions or pop-ins [85-86] in the nanoindentation data need to be avoided. Hence for the annealed and lightly deformed samples, nanoindentation data obtained using the 100μm indenter tip was used. In these materials, due to the very low density of active dislocation sources, nanoindentation tests with small indenter tips result in displacement bursts (pop-ins) at near-theoretical stresses [74] that mark the transition from elastic to post-elastic material response. In the nanoindentation stress-strain curves,

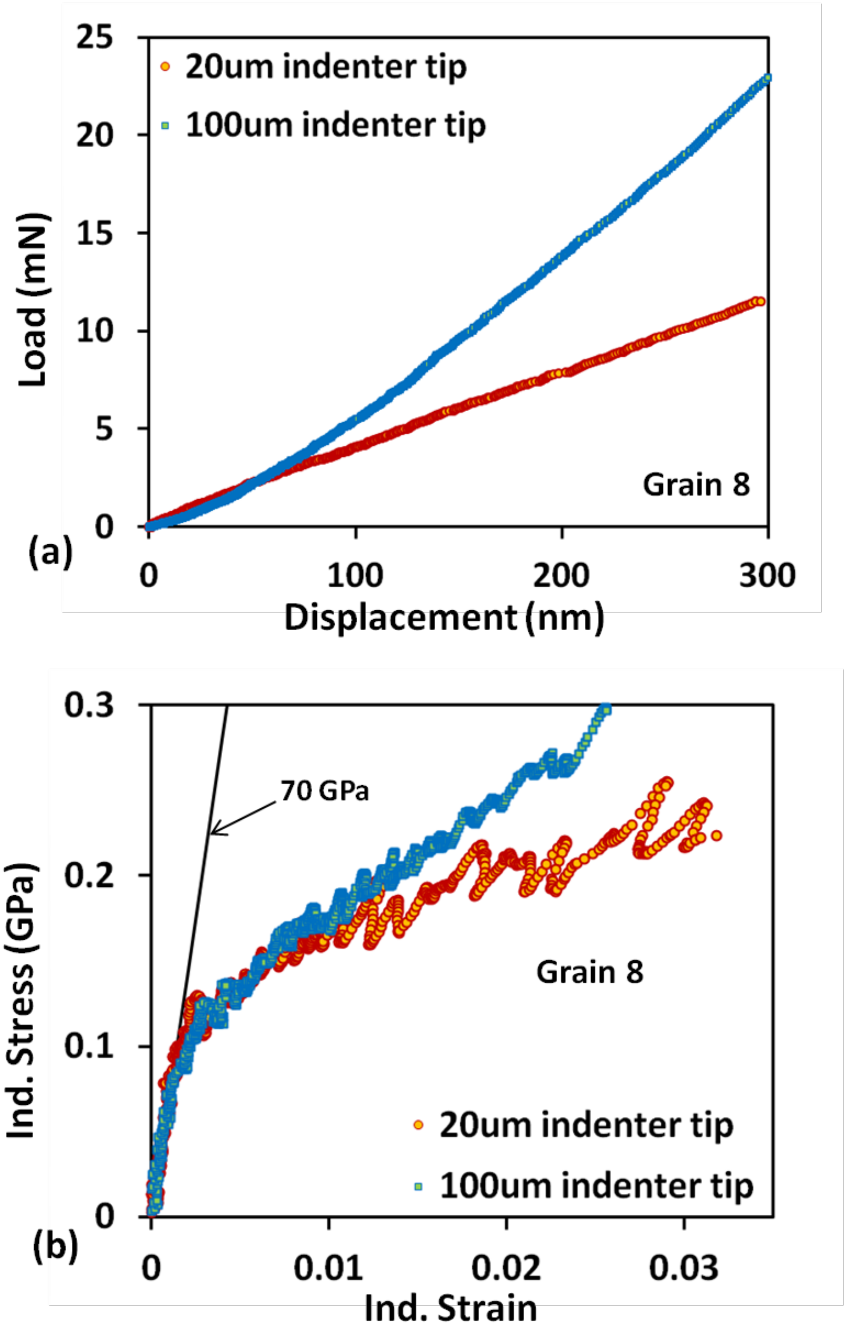

Figure 4.2: Effect of indenter size on the (a) load displacement curves (b) indentation stress–strain curves from deformed samples. a While the indentation stress– strain curves obtained using two different indenter radii show a similar Y_{ind} value, the bigger 100 µm indenter shows larger strain hardening than the smaller 20 µm indenter.

these pop-ins manifest as strain bursts at near theoretical strengths followed by an unloading part before the stresses approach values that represent flow stresses in the absence of the pop-in. Thus, the occurrence of pop-ins masks the yield behavior and the extraction of the indentation yield point becomes difficult. Since the indentation zone is much larger for a larger indenter tip, the probability of finding the necessary dislocation sources to accommodate the imposed deformation is higher, and hence the probability of the occurrence of the pop-in is greatly reduced. As seen in [74] the pop-in size decreases with increase in the indenter tip size. Figure 4.1 shows the size of the pop-in on an indentation stress-strain curve, for representative nanoindentation data on pure aluminum obtained using the 1 µm, 5 µm and 100 µm spherical tips. Note that the pop-in is almost completely absent for the test preformed with the 100 µm spherical tip. Therefore the 100 µm indenter tip is preferred for the extraction of the indentation yield stress values in these materials.

However, in heavily deformed samples, large in-grain misorientations and grain fragmentation are expected to occur. In these cases as well as to probe near grain boundary regions, a smaller indenter tip was required in order to obtain the necessary spatial resolution. Since the dislocation density in the deformed materials is high, pop-ins are either absent or when present, are much smaller in size. Hence their occurrence is not a concern. The effect of the indenter tip size on the indentation response of a moderately deformed sample (20% reduction in height by plane strain compression) is shown is Figure 4.2. All the data used for comparisons was obtained within the same grain. As seen from the figure, although there is significant difference in the post elastic behavior, the values of Y_{ind} are in excellent agreement in the two indentation stress-strain curves.

This observation is in agreement with the findings discussed in [64] regarding the effect of indenter tip size on the indentation stress strain curves. For this work, since we are interested only in the Y_{ind} values, switching the indenter tip size between 20 µm and 100 µm does not affect the extracted values.

CHAPTER 5

GRAIN-SCALE MECHANICAL RESPONSE IN ALUMINUM POLYCRYSTALS

5.1 Introduction

In metallic materials, energy is predominantly stored in the form of defects, dislocations in particular. The increase in the density of dislocations during plastic deformation of a metallic material is directly proportional to the stored energy of plastic work [92]. With the increase in the dislocation density in a deformed structure, the movement of dislocations is impeded by interactions with other dislocations resulting in significant changes in the mechanical properties. Therefore, changes in the local mechanical properties can be used as a measure for local stored energy in deformed metallic materials.

Over the last decade, nanoindentation has emerged as a tool of choice for investigating sub-micron scale material behavior since the interrogation volume under the indenter is of the order of cubic micrometers or less, depending on the indenter tip size. Examining the indentation data in the form of ISS curves provides better insights into the microscale mechanical response in the sample (interpreted as an averaged response from the indentation zone) and makes it possible to extract meaningful information such as the local indentation modulus, indentation yield stress (elastic-plastic transition) and certain aspects of the strain hardening response from the initial loading segment of the nanoindentation data. In recent work, the use of ISS curves has been demonstrated to produce new insights into material mechanical behavior at lower length scales such as grain-scale elastic and plastic anisotropy in metallic materials [63], role of grain boundaries during plastic deformation in metals [64], buckling response of carbon nanotube forests [65], and the dependence of lamellar level mechanical properties in bone on the local mineral composition [66].

In this second task of this thesis, we apply the protocols established in [5] to combine the local mechanical properties obtained from nanoindentation with the complimentary structure information obtained using electron backscatter diffraction (EBSD) to extract information about changes in the indentation yield values resulting due to the imposed macroscopic deformation and use this information to compute local stored energy changes. The first step in this task is to characterize the plastic anisotropy in fully annealed, high purity aluminum. As mentioned in Section 4, aluminum exhibits negligible elastic anisotropy. However, the local crystal orientation can have a very significant effect on the measured indentation yield strength (Y_{ind}). Establishing the dependence of Y_{ind} on the local crystal orientation for aluminum is extremely important because this relationship serves as a base-line for later tasks. When interpreting indentation results on deformed samples, this 'yield surface map' will be used to isolate the contribution of local orientation to the Y_{ind} from the changes in Y_{ind} resulting from the imposed macroscopic deformation.

The second goal of this work is to gain insights into the microstructure development during plastic deformation. It is well known that the microstructure that develops during plastic deformation is highly complex typically exhibits strong anisotropy. In spite of several experimental and modeling studies [7, 11, 93-95], the physics of microstructure evolution during plastic deformation is not fully understood, mainly due to the difficulty in extracting relevant quantitative information at a sub-micron length scale. In this paper, we address this gap using our recently developed protocols for nanoindentation data analysis, together with orientation imaging microscopy.

The chapter is organized as follows: Section 5.2 provides the details of the experimentation methodologies used in this study. The experimental observations and discussion of the results is provided is Section 5.3. Concluding remarks are presented in section 5.4.

5.2 Experimental procedure

Four large grained aluminum samples in the fully annealed condition were used to identify 27 grains of different orientations, spread out over the inverse pole figure triangle (IPF). As detailed in section 4, these samples were sectioned from a heavily rolled high purity aluminum slab, annealed at 640°C for 72 hrs to produce a fully annealed microstructure with large grains. The samples were mounted in epoxy and the surface was polished mechanically, followed by electropolishing. EBSD was used to map the polished surface and determine individual grain orientations. Between 9 and 18 indentation tests were performed on each of the identified grains with the 100 μm spherical tip and using the protocols described in Section 2.4, the ISS curves were plotted for each test. As seen in Figure 5.1, the pop-ins in the annealed samples are either very small or absent while using the 100μm indenter tip. From the ISS curves, the indentation yield point (Y_{ind}) was extracted by back-extrapolating from the post-elastic segment as shown in Figure 5.1(b).

In order to study the effect of macroscale deformation on the local mechanical properties within the grains, three samples, two deformed lightly (10% reduction in height) and other deformed to 20% reduction in height were used. They were processed in the same manner as the samples tested in the fully annealed condition described above, except that they were compressed in a channel die to achieve the desired reduction in height before being mounted and prepared for nanoindentation and OIM. Even in this case, indentation tests were carried out with the 100 μm spherical tip in locations pre-selected with the help of a grain map obtained using OIM. At least 15 indents were performed in each grain due to the increased heterogeneity in the microstructure of deformed samples and higher expected scatter even for tests done within the same grain. Macroscale deformation increases the dislocation density, and hence in the deformed samples, the pop-ins are almost always completely absent. Therefore, in this case, the value of the indentation stress at 0.1% offset strain was used as the yield point.

5.3 Results and Discussion

The OIM scans of one of the four samples tested in the fully annealed condition is shown in Figure 5.2. The placement and approximate size of the indents with respect to the grains is also shown in this figure. Each grain in the OIM map is color coded to represent its position on the standard [001] inverse pole figure (IPF). In other words, the color represents the crystal direction in the grain that is perpendicular to the sample surface and parallel to the loading direction during nanoindentation testing. Note that since the indenter tip is axisymmetric, in-plane rotations of the crystals will not alter the nanoindentation response. Consequently, the nanoindentation response is only a function

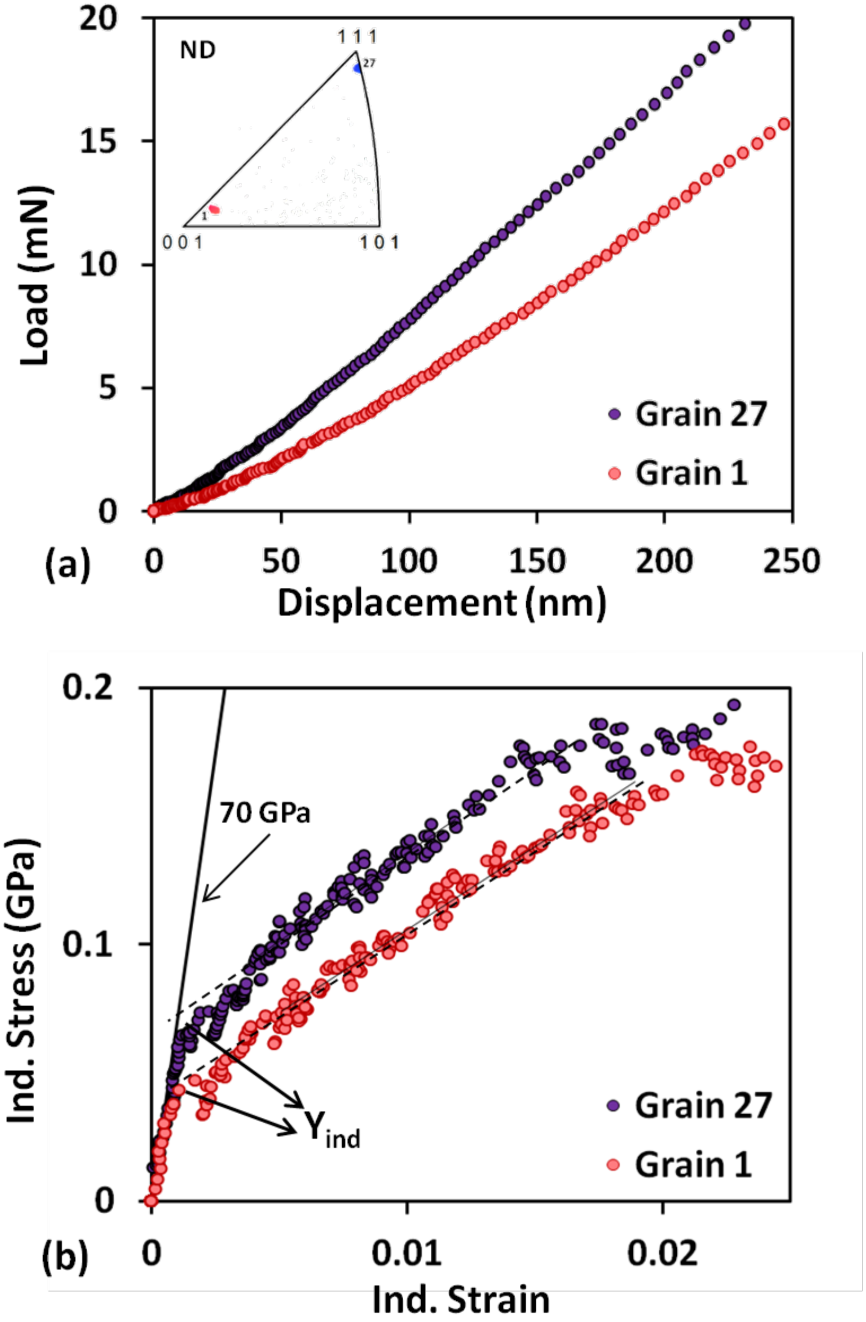

Figure 5.1: (a) The measured load-displacement data for two grains (grain #1 and grain #24) in the fully annealed condition. The inset shows the IPF map which indicates the orientation of the grains with respect to the indentation axis. The corresponding ISS curves are in (c) and show that the Yind varies quite significantly between the two orientations.

of two (Φ, φ2) of the three Bungle Euler angles [91] used to represent the grain orientation.

Representative load-displacement and corresponding ISS curves for two grains are plotted in Figure 5.1(a) and Figure 5.1(b) respectively. Grain #1 is close to the [001] corner of the IPF triangle, meaning that the [001] crystal direction for this grain is close to the loading direction. On the IPF, the second grain, grain #27 is close to the [111] corner and has the [111] crystal direction almost parallel to the loading direction. The misorientation between these two orientations is close to the maximum possible value for cubic crystals and, as expected, these two orientations show a very large difference in their nanoindentation response. On the other hand, measurements made within the same grain agree very well with each other. Multiple (9-18) measurements were performed on each grain to account for the experimental scatter and increase the confidence in the extracted Y_{ind} values. It should be noted here that the nanoindentation response within each grain was highly consistent and the standard deviations for the extracted indentation yield points were very small. While representative nanoindentation data for only two grains is shown in Figure 5.1, a total of twenty seven grains were tested using the 100 μm spherical tip, in order to populate the entire stereographic triangle.

Table 5.1 provides a summary of the tests results for all the grains tested in the fully annealed condition. Note here that as expected, the indentation modulus (E_s) values measured for all the grains are very close to one another. The values in this table show that the Y_{ind} however, can vary by up to 40% depending on the orientation of the grain. Figure 5.3 is a contour plot showing the dependence of the indentation yield strength

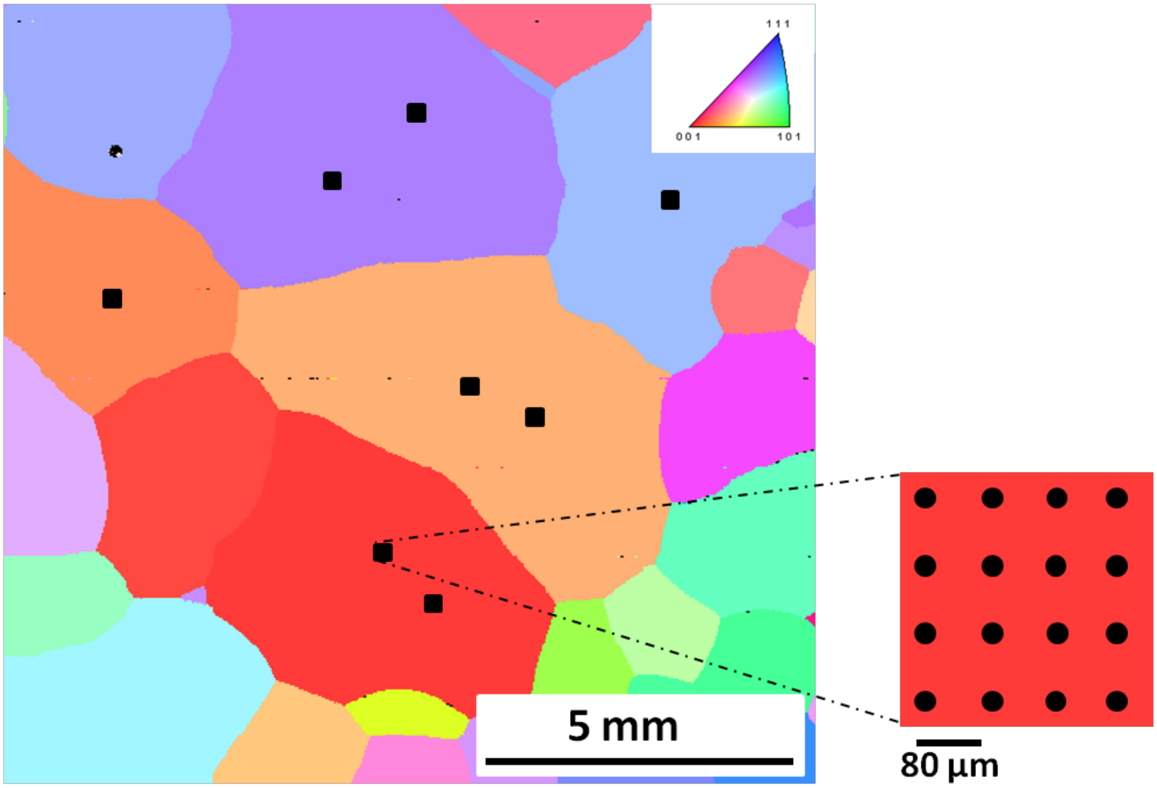

Figure 5.2: OIM map of one of the four fully annealed pure aluminum samples used to generate the indentation yield surface map. Since the grains are very large (~2-3 mm) only a limited number of orientations are present on each sample surface and hence multiple samples had to be tested in order to populate the entire IPF triangle. The black squares denote the approximately size of the grid of indents performed within in grains, using the 100 µm tip. Each grid contained a total of 16 indents (4 rows and 4 columns) placed 80 µm apart

(Y_{ind}) on the local crystal lattice orientation at the indentation site. This plot was generated by interpolating between the measured indentation yield strength (Y_{ind}) values for the 27 grains provided in Table 5.1. The inset in Figure 5.3 shows the orientations of the different grains tested in terms of an IPF map. The lowest indentation yield value observed was 49 MPa for grain #1, a grain close to the cube orientation and the highest value observed was 69.5 MPa for the grain very close to the [111] orientation (grain #27). Since the dislocation structure and density in an annealed material is expected to be very small and independent of the crystal lattice orientation, this variation in the indentation yield stress with respect to the crystal orientation is fully attributable to the differences in the orientations of the active slip systems with respect to the loading direction. A similar indentation yield surface map has been reported [63] for Fe-3 wt% Si (bcc) and in this case, the Y_{ind} varies by as much as 33% depending on the orientation. While the orientations closest to [001] showed the lowest values for Y_{ind} and those closest to [111] still showed the highest values, the difference in the Y_{ind} values between the grains close to [111] and [101] grains was much more significant in this case. Although there is no simple analytical means to verify this dependence of Y_{ind} on local crystal orientation, crystal plasticity finite element models (CPFEM) could be used to verify it. Also, if we assume that most of the stresses during indentation are along the indentation direction, then it follows that the Y_{ind} would vary almost linearly with the Taylor Factor for simple compression. This is shown in Figure 5.4. Note that this is only an approximation and the stress state during indentation is far more complex than that for simple compression.

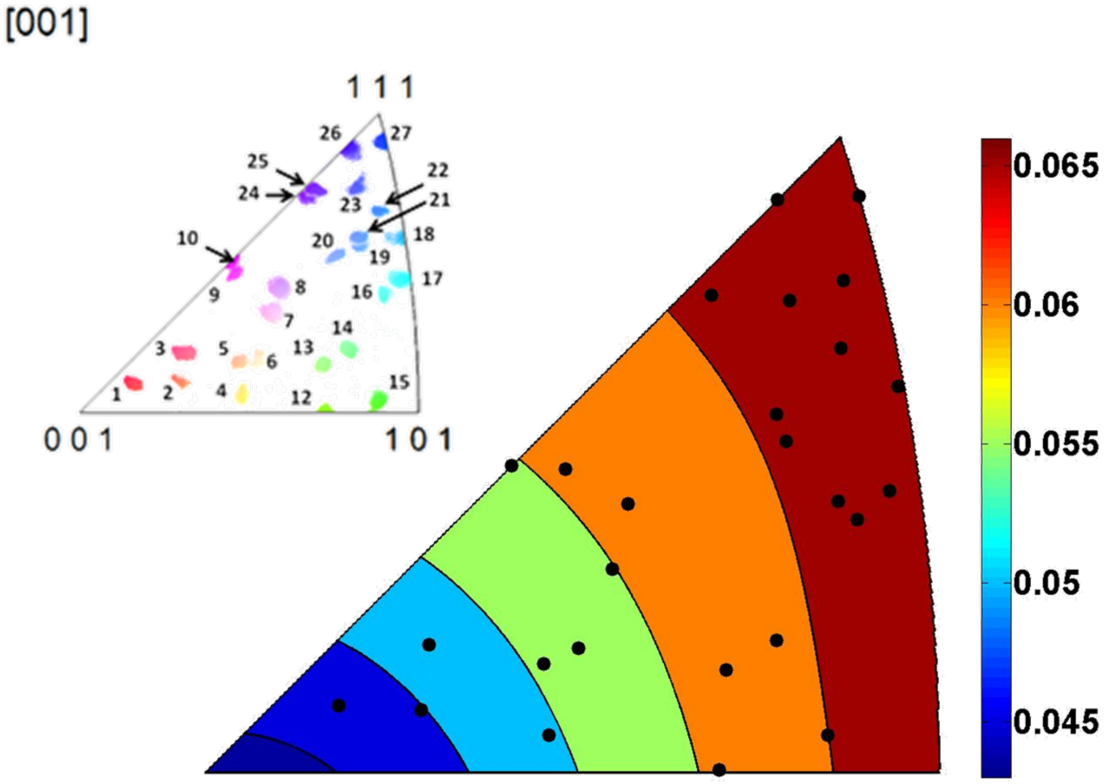

Figure 5.3: Contour plot generated by interpolating the average Y_{ind} values extracted for the 27 grains. The black circles and the inset show the IPF map with the position of all the grains with respect to the indentation axis. The inset shows the IPF map showing the positions of all the grains, with respect to the indentation axis, tested in the fully annealed condition in order to generate the Y_{ind} surface map.

Using this indentation yield surface plot, Y_{ind} for any given orientation of pure aluminum in the fully annealed condition can now be predicted. We shall focus on characterizing the local mechanical properties in the deformed sample for the remainder of this section, with the goal of obtaining insights into the stored energy distribution in the material after plastic deformation.

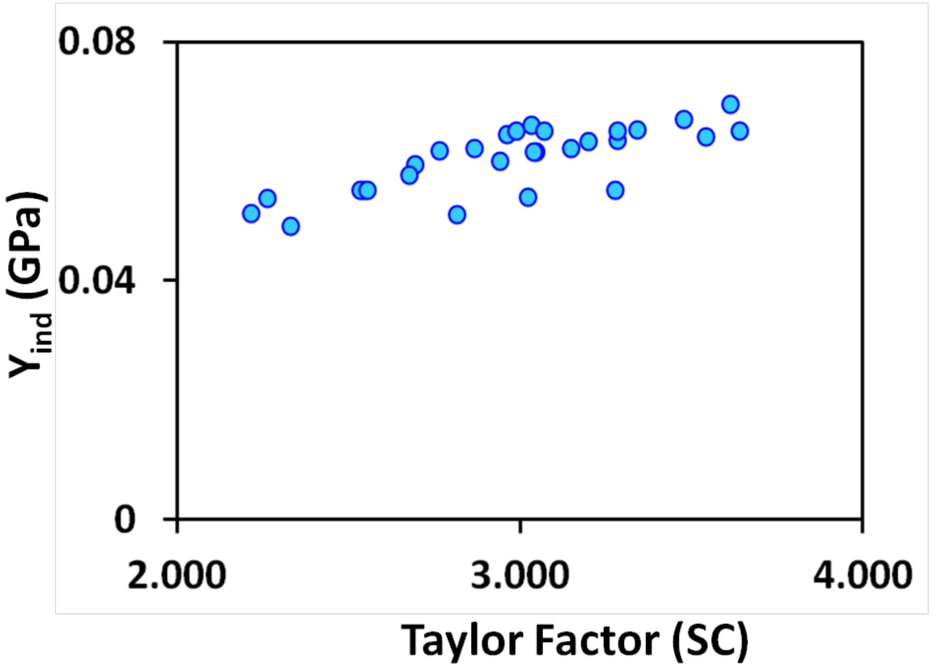

Figure 5.4: Variation of Yind (GPa) with respect to Taylor Factor for simple compression.

When a material is deformed plastically, a small fraction of the work done on the sample is stored in a deformed sample, mostly in the form of dislocations. This increase in the dislocation density due to plastic deformation reduces the mean free path for dislocation motion. Therefore higher stresses are required to deform the sample further.

The dislocation density and hence the stored energy in a deformed material is far from uniform and understanding its distribution is expected to provide key insights into material behavior during thermo-mechanical processing.

For this part of the work, we used two high purity aluminum samples subjected to light deformation (10% reduction in height) and another subjected to moderate deformation (20% reduction in height). OIM map of the sample deformed to 10% reduction in height is shown in Figure 5.5 and for the sample deformed to 20% reduction in height shown in Figure 5.6 (due to the limitations of the microscopes, the entire sample surface could not be captured in one scan). As seen in these maps, for deformed samples, there is a much larger spread in orientation within the grains. This spread is also higher for a sample with higher amount of deformation as compared to the lightly deformed sample. However, no significant grain fragmentation was observed in either of these samples. Again, indentation tests were performed on selected regions within the individual grains (well away from visible grain boundaries). It was once again observed that multiple indentations performed on same grains produced consistent measurements. In this case, the pop-ins were almost always completely absent.

The indentation yield strength values in this case were extracted as stress at 0.1% offset strain. An offset of 0.1% was picked because finite element simulations [73] of nanoindentation experiments have shown that at about this value, the elastic plastic transition is completed and the deformation under the indenter is predominantly plastic. Also, this offset approach, when used to extract Y_{ind} for data on fully annealed pure aluminum with no pop-ins, produced values that were consistent with those obtained using the back-extrapolation method. It should be noted again that a significant fraction

Table 5.1: Details about the 27 grains tested in the fully annealed condition: Orientation of the grains in terms of the Bunge-Euler angles, the measured indentation modulus (*E_s*) and the extracted indentation yield strength (*Y_{ind}*).

	Grain Orientation				
Grain No	φ_1	Φ	φ_2	E_s (Gpa)	Y_{ind} (GPa)
1	73.1	9.8	63.4	68.49 ± 0.81	0.049 ± 0.004
2	224.9	14.7	73.9	68.18 ± 0.85	0.054 ± 0.005
3	219.9	16.8	60.3	69.02 ± 0.29	0.051 ± 0.004
4	143	22.4	83.7	68.56 ± 0.22	0.055 ± 0.001
5	347.9	23	72.2	68.13 ± 0.9	0.055 ± 0.004
6	29	25.4	71.6	68.11 ± 1.77	0.055 ± 0.002
7	60.9	29.2	63.4	68.3 ± 1.9	0.062 ± 0.003
8	348.5	32	57.6	68.27 ± 0.94	0.065 ± 0.005
9	190.1	30.2	49.9	68.32 ± 0.5	0.065 ± 0.006
10	347.2	27.9	45	67.54 ± 0.5	0.060 ± 0.006
12	23	32.8	89.7	68.27 ± 0	0.058 ± 0.001
13	13.7	33.8	78.8	67.62 ± 2.29	0.059 ± 0.004
14	306.5	37.1	77	67.35 ± 0.2	0.062 ± 0.004
15	299.7	39.3	86.5	68.29 ± 0.77	0.063 ± 0.005
16	273.4	43.6	68.8	68.48 ± 0.96	0.066 ± 0.007
17	167.3	45.9	67.6	67.62 ± 0.56	0.062 ± 0.004
18	219.6	49.6	60.3	68.24 ± 0.49	0.065 ± 0.003
19	232.2	42.2	57.9	68.63 ± 0.96	0.065 ± 0.004
20	15	41.9	60.3	68.37 ± 1.14	0.061 ± 0.007
21	196.7	52.3	59	67.94 ± 0.95	0.065 ± 0.005
22	222.7	52.4	55.9	68.44 ± 0.85	0.064 ± 0.004
23	185.6	46.5	51.1	67.97 ± 0.71	0.067 ± 0.006
24	288.6	43	66.8	68.06 ± 0.78	0.062 ± 0.006
25	241.3	43.4	46.7	68.72 ± 1.37	0.063 ± 0.006
26	45.4	53	48.6	67.86 ± 0.69	0.065 ± 0.007
27	45	49.7	45	67.99 ± 0.88	0.070 ± 0.007

of the tests on aluminum in the fully annealed condition produced pop-ins and therefore the offset yield method could not be used to extract Y_{ind}. Figure 5.7 shows the difference in the nanoindentation response for two grains of the (almost) same orientation, one being tested in the fully annealed condition and the other after light deformation (10% reduction in height). As seen here, the increment in the indentation yield strength can be as high as 60% depending on the location of the indent.

Tables 5.2 and 5.3 summarize the indentation measurements on the deformed samples. For each of the grain tested in the deformed condition, the indentation yield point (Y_{ind}) in the fully annealed condition was predicted using the indentation yield surface presented in Figure 5.3. This is the indentation yield strength that would have been measured for the orientations in question, if they were tested in the fully annealed condition. It is important to establish this value since the Y_{ind} can vary by as much as 40%, even in the fully annealed condition, depending on the local crystal lattice orientation at the indentation site. A reliable estimate of the increment in the indentation yield strength (ΔY_{ind}) for any given orientation can then be determined as the difference between the measured indentation yield point ($Y_{ind}(g,d)$) in the deformed condition and the estimated $Y_{ind}(g,0)$ in the fully annealed condition and is given as

$$\Delta Y_{ind}(g,d) = Y_{ind}(g,d) - Y_{ind}(g,0) \tag{5.1}$$

where d refers to the deformation step- 10% or 20% reduction in height by plane-strain compression and g refers to the local crystal lattice orientation at the indentation site.

The simplest relationship that one can establish between the increment in the indentation yield point and the local dislocation content is through the increment in the

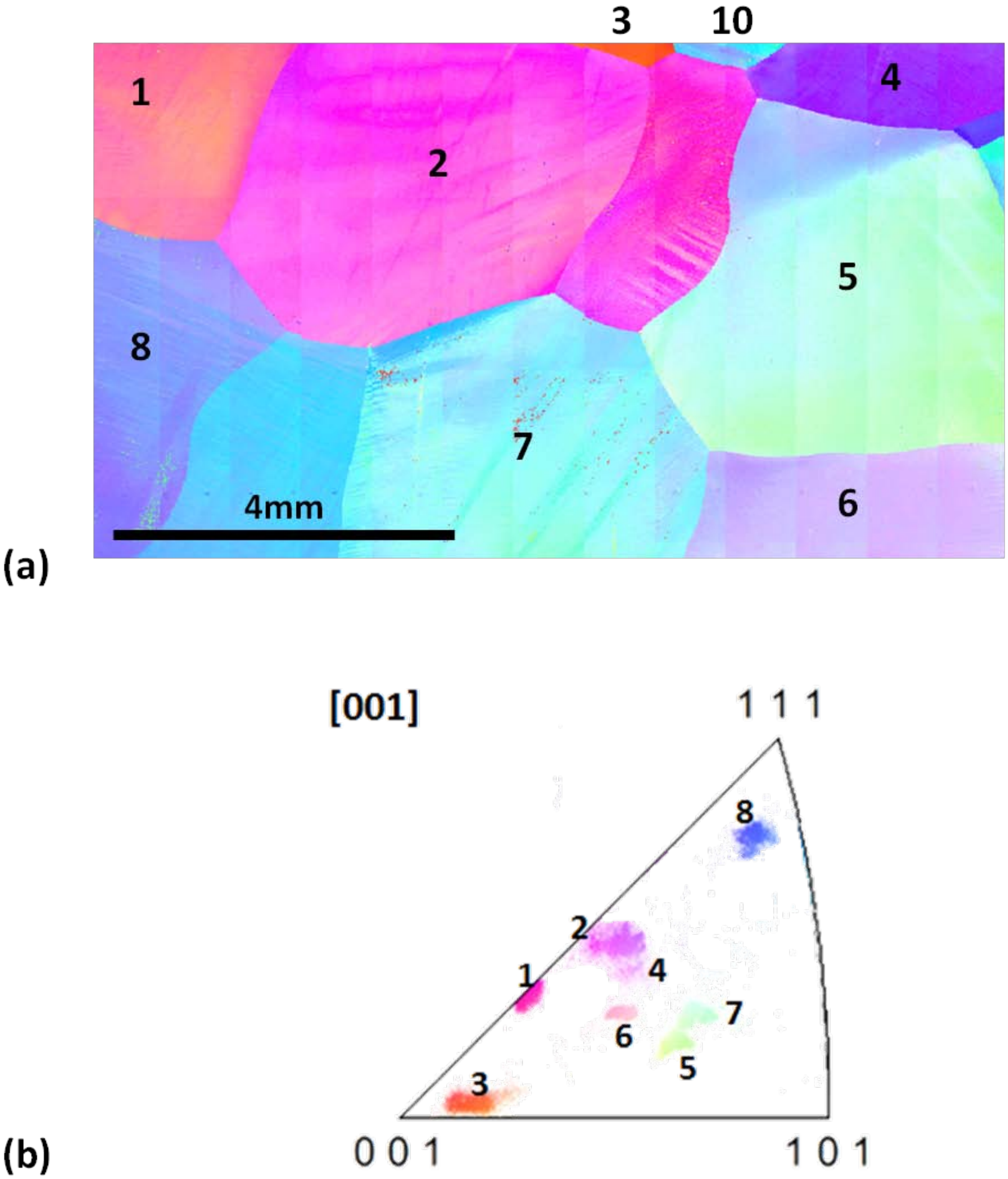

Figure 5.5(a): OIM map of a part of the aluminum sample deformed by plane strain compression to 10% reduction in height. (b) The IPF map showing the positions of all the grains with respect to the indentation axis for the sample. Note the larger spread in orientations within individual grains, as compared to the fully annealed samples (See Fig 5.3)

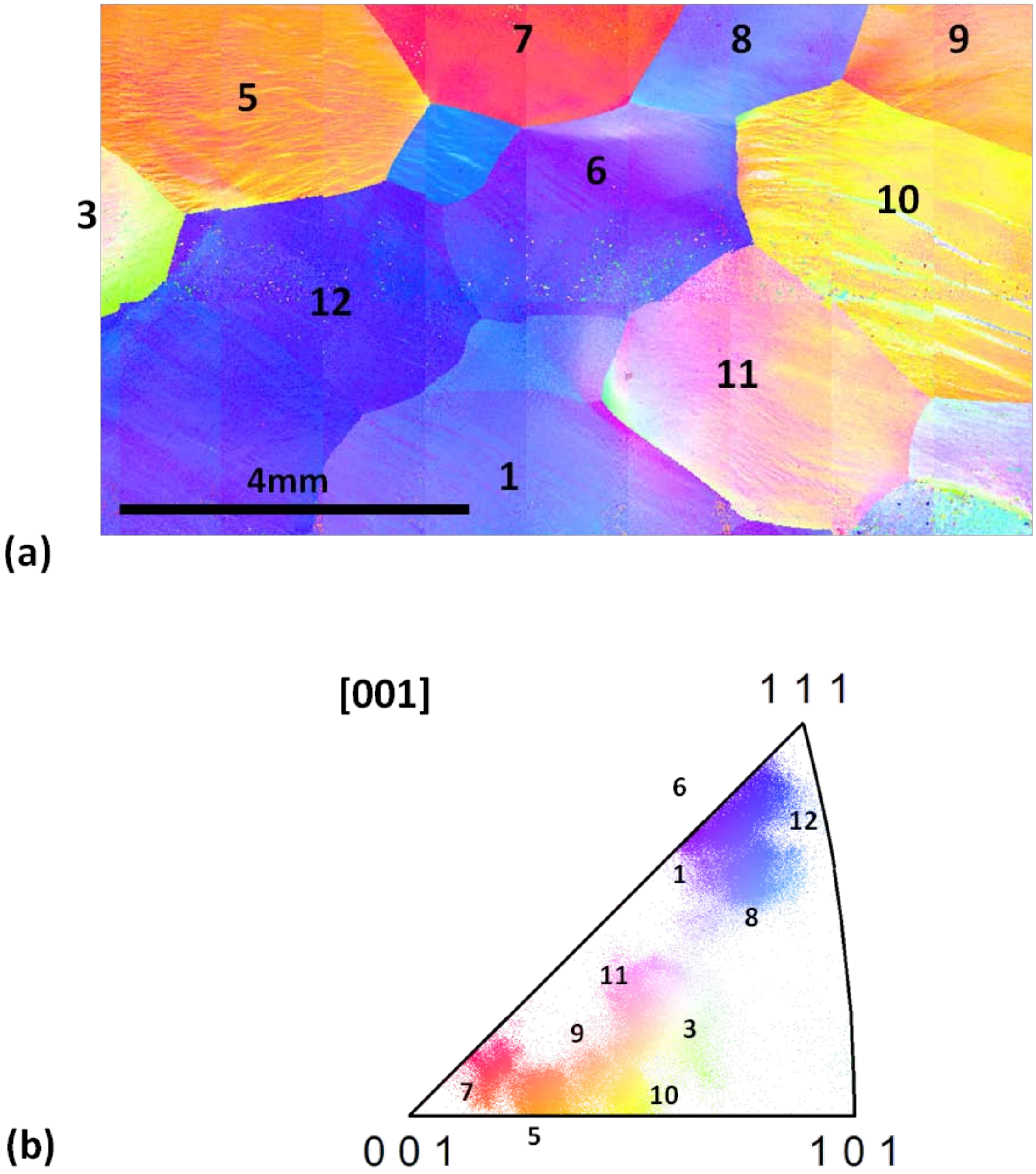

Figure 5.6(a): OIM map of the aluminum sample deformed by plane strain compression to 20% reduction in height. (b) The IPF map showing the positions of all the grains with respect to the indentation axis for the sample. Note the larger spread in orientations within individual grains, as compared to the fully annealed samples (See Figure 5.3) as well as the 10% deformed sample (Figure 5.4)

critical resolved shear strength of the slip system. In a highly simplified manner, this relationship can be expressed as

$$Y_{ind} = M\left(\Phi, \varphi_2\right)\tau_{crss} \tag{5.2}$$

$$\Delta\tau_{crss} \propto \sqrt{\rho} \tag{5.3}$$

and

$$M = \frac{\sum \Delta\gamma}{\Delta\varepsilon} \tag{5.4}$$

where M is a Taylor-like factor that depends only on the grain orientation with respect to the indentation direction (in this case, only two of the three Bunge-Euler angles describing local crystal orientation), τ_{crss} is the average critical resolved shear stress in the crystal, $\Delta\tau_{crss}$ is the increment in the local averaged critical resolved shear strength between the annealed and deformed conditions, and ρ is the local dislocation density. $\Sigma\Delta\gamma$ is the sum of the shears on all the slip planes and Δε is the imposed macroscopic strain.

Combining Eq. (5.1) and (5.2), the percentage increase in the critical resolved shear stress is given as

$$\frac{\Delta Y_{ind}}{Y_{ind}\left(g,0\right)} = \frac{\Delta\tau_{crss}}{\tau_{crss}\left(g,0\right)} \tag{5.5}$$

Since the change in the average critical resolved shear stress ($\Delta\tau_{crss}$) in the crystal can be related to the local dislocation density (ρ) (Eq. 5.3), the percentage increase in Y_{ind} provides an indirect measure of the local dislocation content or the local stored energy in the deformed samples.

From Table 5.2 and 5.3 it is clear that the percentage differences in the Y_{ind} between the annealed and deformed condition, or in other words, the change in the

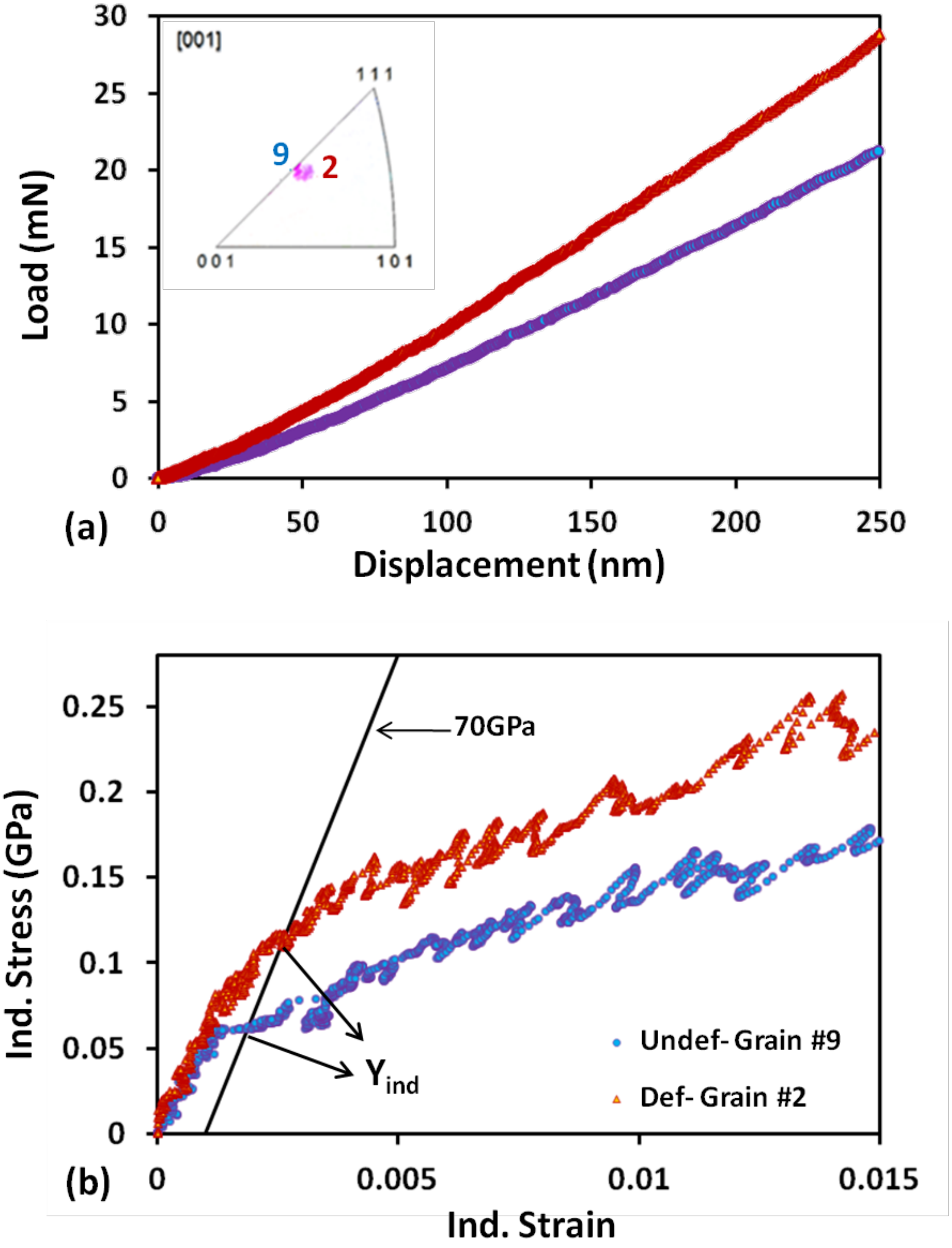

Figure 5.7: (a) The load-displacement data (b) Corresponding indentation stress-strain curves, for two almost identically oriented grains (4.3° misorientation). Grain #9 was tested using a 100 µm spherical tip in the fully annealed condition and grain #3 was tested after the sample was deformed to 10% reduction in height y plane strain compression

local dislocation density is highly non-uniform and varies significantly depending on the orientation of the grain. Also reported in the Tables 5.2 and 5.3 are values of the Taylor factor for plane strain compression for each of the orientation of interest. Taylor factor is a parameter frequently used for indication of slip activity for a particular orientation, during a given deformation mode. Thus, an orientation with a lower Taylor factor is expected to undergo a lower amount of slip activity in order to accommodate the imposed strain, as compared to an orientation with the higher Taylor factor. Consequently, an orientation with a lower Taylor factor is expected to have a lower amount of stored dislocations. Taylor Factors for the orientations of interest were calculated using a simple Taylor model [25]. Note here that the Taylor factors reported in Table 5.2 and 5.3 are for plane strain compression, and are and are not to be confused for Taylor factors for spherical nanoindentation. Although both are Taylor factors, they are for different deformation modes – one for indentation and the other for plane strain.

A lower Taylor factor in Table 5.2 and 5.3 implies that the crystal orientation is favorably oriented to accommodate the imposed deformation by plane strain compression, while a higher Taylor factor means that the crystal in question is unfavorably oriented to accommodate the imposed deformation. This may be and often is very different from the Taylor factor corresponding to indentation, particularly because the sample was compressed along ND during plane strain compression, while indentation was carried our perpendicular to the TD surface.

It has been hypothesized [96-97] that orientations with a lower Taylor factor (Taylor soft grains) develop lower stored energies compared to grains with a higher Taylor factor (Taylor hard grains) and that for a given increment of imposed plastic

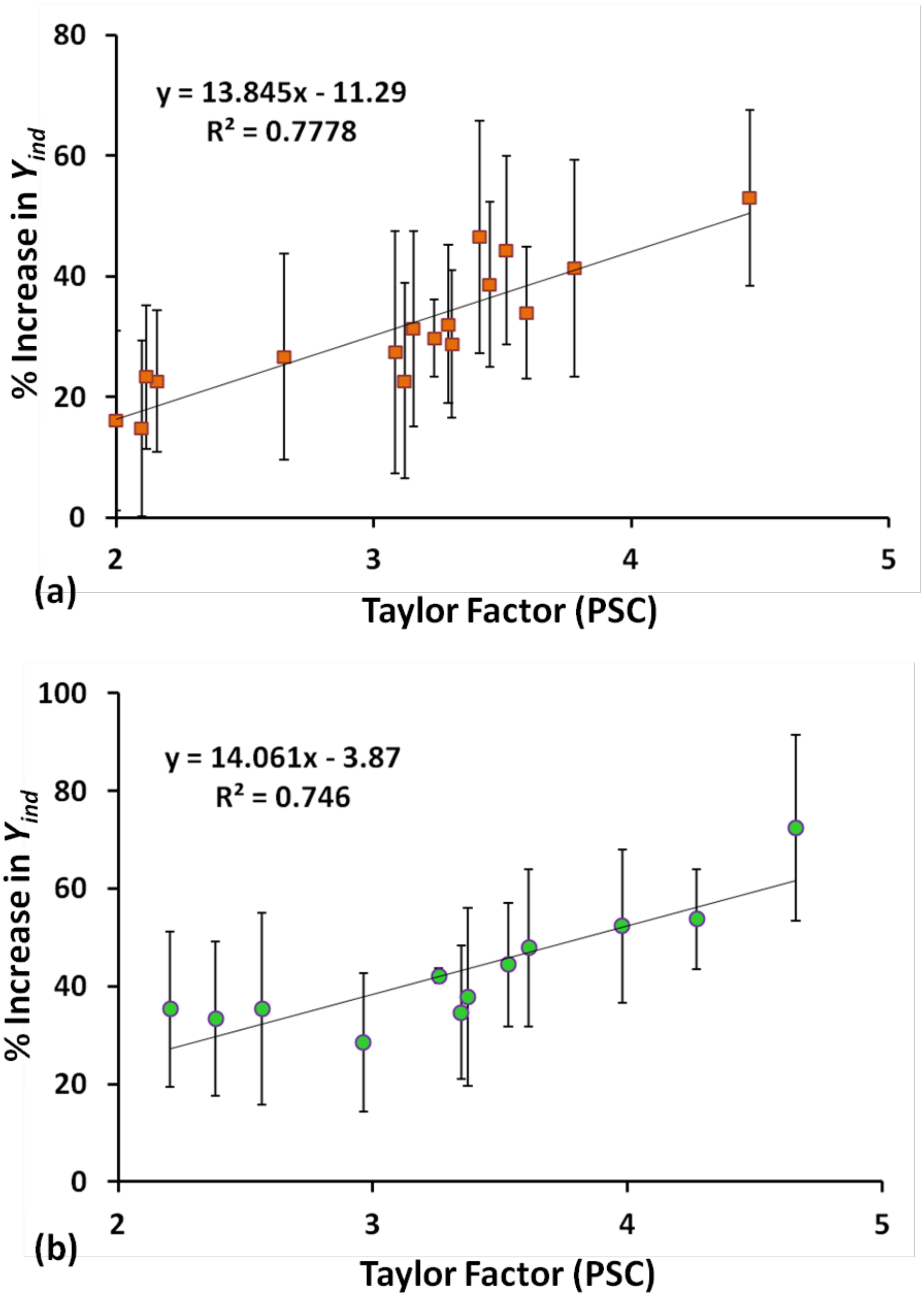

Figure 5.8: Plot of the percentage increase in the indentation yield strength resulting from the macroscopic deformation, for individual grains, as a function of Taylor Factor for plane strain compression, for the sample deformed to (a) 10% and (b) 20% reduction in height

strain, the increment in stored energy is directly proportional to the Taylor factor. Figure 5.8 shows the variation of the percentage increase in the indentation yield strength as a result of the macroscopic deformation, for individual grains, as a function of Taylor Factor for plane strain compression for the samples deformed by 10% and 20% reduction in height respectively. It is seen in both these cases there is a fairly strong linear relationship between the Taylor factor for PSC and the percentage increase in Y_{ind}. This is a very important finding and supports the hypothesis.

The observed deviation from a perfect linear relationship between Taylor factor and percentage increase in Y_{ind} can be due to one or more of the following reasons: (i) inherent scatter in the experimental data and limitations of the testing equipment. (ii) Taylor model assumes full-constraints or very strong interactions. In reality, we have relaxed constraints. It has been shown that [7] grain interactions lead to activation of different slip systems than those predicted by Taylor model. (iii) Grains that deform by single slip (or fewer intersecting slip systems) may result in a lower rate of storage of dislocations as compared to grains that deform with a higher number of active slip systems, due to the increased probability of dislocation interaction in the latter case. (iv) The Taylor factors reported are for orientations after macroscopic deformation while the starting orientations may be different. The deformation path followed by individual grains is likely to affect its final stored energy thus contributing to the scatter in the plots.

From Tables 5.1-5.3 and Figure 5.8, it is also seen that the scatter in the measured Y_{ind} values for individual grains is higher for the deformed samples as compared to the scatter observed for the annealed samples. This is expected because, for the deformed samples, in addition to the experimental scatter in the Y_{ind} values, there is also real

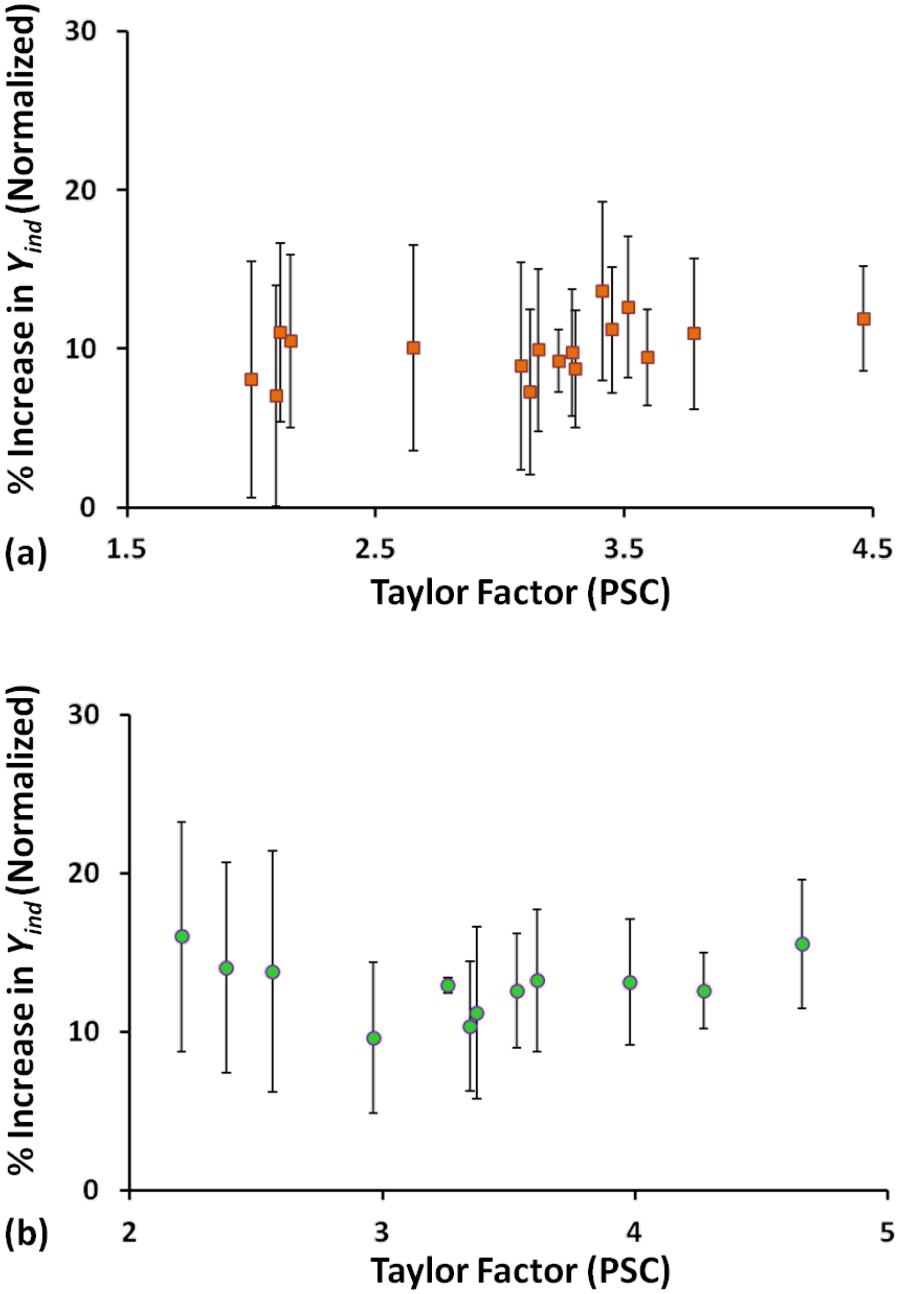

Figure 5.9: Plot of the percentage increase in the indentation yield strength, normalized by Taylor Factor, as a result of the macroscopic deformation, for individual grains, as a function of Taylor Factor for plane strain compression, for the sample deformed to (a) 10% and (b) 20% reduction in height

variation in the dislocation density (or stored energy) from one location to another within individual grains.

Hardening (*h*), during macroscopic deformation is defined as

$$h = \frac{\Delta s}{\sum \Delta \gamma} \tag{5.6}$$

where Δs in the change in slip resistance and $\Sigma\Delta\gamma$ is the sum of the shears on all the slip planes. Combining Eq. (5.6) with Eq. (5.4) and Eq. (5.5), it follows that the percentage change in Y_{ind} normalized by the Taylor Factor (for plane strain compression) is a constant given as

$$\frac{\Delta Y_{ind}}{Y_{ind}(0)} \Big/ M = \frac{h * \Delta\varepsilon}{s_0} \tag{5.7}$$

where s_o is the initial slip resistance. In Figure 5.9, the percentage increase in the $Y_{ind,}$ normalized by the Taylor factor is plotted against Taylor Factor. In this case, the best fit line is almost horizontal for both the lightly deformed and the heavily deformed case. Although the amount of strain in the 20% deformed sample is almost twice that for the 10% deformed sample, the increase in the value of the constant is fairly small between the two cases. This indicates that the value of h is decreasing as the amount of strain increases. In other words, our data is suggesting a saturation type hardening in the material.

Table 5.2 and 5.3 (Page 73 and 74): The grain orientations, corresponding Taylor factor for PSC, extracted values of Y_{ind} measured using indentation, the predicted Y_{ind} values for the orientation in the fully annealed condition and percentage increase in the Y_{ind}, as a result of the imposed macroscopic strain for the sample deformed to 10% and 20% reduction in height, respectively, by plane strain compression.

Grain No	Grain Orientation			Taylor Factor for PSC	Predicted Yind (undef)	Yind (GPa)	% increase in Yind
	φ_1	Φ	φ_2				
1	180.8	19.5	45.0	4.46	0.055	0.084 ± 0.008	53.08 ± 14.60
2	328.1	31.0	52.8	3.12	0.061	0.075 ± 0.010	22.69 ± 16.19
3	257.6	9.7	80.0	3.41	0.046	0.068 ± 0.009	46.53 ± 19.23
4	43.3	33.4	51.8	2.16	0.062	0.076 ± 0.007	22.65 ± 11.73
5	44.3	30.9	72.6	3.45	0.061	0.084 ± 0.008	38.64 ± 13.68
6	58.0	25.9	63.4	3.51	0.058	0.084 ± 0.009	44.36 ± 15.58
7	62.2	32.4	68.2	3.59	0.061	0.082 ± 0.007	34.00 ± 10.92
8	251.8	47.1	51.8	3.08	0.066	0.085 ± 0.013	27.45 ± 20.12
9	97.8	38.2	66.0	2.65	0.064	0.081 ± 0.011	26.65 ± 17.11
10	155.2	44.5	56.3	3.30	0.066	0.085 ± 0.008	28.83 ± 12.24
11	256.8	49.7	53.6	3.29	0.067	0.088 ± 0.009	32.08 ± 13.11
12	129.1	38.9	47.5	2.10	0.064	0.074 ± 0.009	14.80 ± 14.60
13	270.0	35.3	45.0	3.78	0.063	0.089 ± 0.011	41.38 ± 17.96
14	36.0	42.7	49.4	2.12	0.066	0.081 ± 0.008	23.36 ± 11.91
15	135.7	38.8	48.5	2.00	0.064	0.075 ± 0.010	16.12 ± 14.94
16	274.8	29.1	54.5	3.15	0.060	0.079 ± 0.010	31.30 ± 16.14
17	231.8	36.5	53.1	3.23	0.064	0.082 ± 0.004	29.81 ± 6.36

Grain No	Grain Orientation			Taylor Factor for PSC	Predicted Yind (undef)	Yind (GPa)	% increase in Yind
	φ_1	Φ	φ_2				
1	119	43.2	56.3	2.20	0.066	0.089 ± 0.011	35.32 ± 15.96
2	13.6	38.4	77.3	2.38	0.065	0.086 ± 0.010	33.40 ± 15.80
3	143.7	28.1	69.4	3.53	0.059	0.085 ± 0.008	44.42 ± 12.70
4	189.2	35.3	48.8	3.26	0.063	0.089 ± 0.010	42.12 ± 15.54
5	152	15.8	71.2	4.66	0.051	0.088 ± 0.010	72.47 ± 18.97
6	116.8	40.5	47	2.96	0.065	0.083 ± 0.009	28.52 ± 14.17
7	224.4	10.8	69.4	3.37	0.048	0.065 ± 0.009	37.81 ± 18.25
8	354	43.2	59.5	3.35	0.066	0.088 ± 0.009	34.63 ± 13.66
9	250	19.6	69.4	4.27	0.054	0.082 ± 0.006	53.79 ± 10.26
10	223.8	21.9	85.2	3.98	0.054	0.082 ± 0.009	52.31 ± 15.77
11	347.5	28.4	67.4	3.61	0.059	0.088 ± 0.010	47.85 ± 16.18
12	51.4	44.8	49	2.57	0.066	0.089 ± 0.013	35.41 ± 19.56

5.4 Conclusions

From indentation stress-strain curves obtained by testing within individual orientation of high purity aluminum in the fully annealed condition, an indentation yield surface map was established that accounts for the effect on local orientation on the indentation yield strength. Even in the fully annealed condition, the indentation yield indentation yield strength. Even in the fully annealed condition, the indentation yield strength values vary by as much as 40% depending on the local crystal orientation. Establishing the variation of indentation yield strength as a function of orientation in the fully annealed condition was necessary for reliably computing the increase in the indentation yield strength as a result of the imposed macroscopic strain, in the deformed samples. Macroscale plastic deformation produced a highly heterogeneous structure and from computations of percentage change in the indentation yield strength, it can be concluded that the grains with low Taylor factors have lower stored energies compared to grains with a higher Taylor factor.

CHAPTER 6

LOCAL MECHANICAL PROPERTIES NEAR GRAIN BOUNDARIES IN DEEFORMED ALUMINUM

6.1 Introduction

As discussed in Section 2, during the recrystallization process, new grains have been observed to nucleate near high angle grain boundary regions in moderately deformed cubic materials [10, 16-17]. It is proposed that steep gradients in stored energies across boundaries as well as high angle grain boundaries provide the necessary driving force for new grains to nucleate and grow from these regions. However, not all high angle grain boundaries are favorable nucleation sites. Our current understanding of deformed microstructures and recrystallization process has many gaps regarding which boundaries are favored as nucleation sites and where along the favored boundaries will nucleation occur.

The Hall-Petch equation [39-40] marks one of the first steps towards quantification of structure-property relations in the field of Metallurgy and Materials Science. Proposed almost 70 years ago, it empirically relates the increase in the material strength to the decrease in the grain size; or in other words increase in the grain boundary content in the sample. The origins [41-42] of the Hall-Petch effect are still a topic of debate in the community in spite of the extensive work being done in the field of grain boundary and interface behavior in general. Moreover, the Hall-Petch equation captures only the macroscopic effect and does not distinguish between the different types of grain boundaries. It is now widely acknowledged that the behavior of grain boundaries is likely to be strongly influenced by the grain boundary character, including misorientation across the grain boundaries, the orientation of the grain boundary with respect to the loading direction, etc. However, the exact nature of these relationships is still unknown. Again, one of the main reasons for our inability to adequately address these questions is the relative difficulty in extracting relevant mechanical information at the length scales of individual grains and grain boundaries.

The recent advances in the analysis of spherical nanoindentation data, which we have extensively discussed in previous sections, now provides a means for extracting very reliable and repeatable measurements of local mechanical properties at a sub-micron length scale. As in the previous section, this local mechanical behavior data will be combined with local structure information obtained using complementary techniques such as orientation imaging microscopy (OIM) to further our understanding of local structure-property relationships in metallic materials and their evolution during macroscopic deformation. In the previous section, we explored the evolution of local mechanical properties within the grains during macroscopic deformation. A natural progression to this work is to investigate the evolution of mechanical properties near the grain boundary regions during macroscopic deformation in these materials. In [64], Pathak et al. have demonstrated the effectiveness of spherical nanoindentation testing in capturing subtle changes in mechanical properties in the grain boundary regions of a deformed Fe- 3% Si steel sample. In this work, we systematically investigate regions around eight grain boundaries in a high purity aluminum sample deformed by plane-strain compression to obtain a 20% reduction in height, with an aim to relate the factors in the grain boundary crystallography and sample geometry to the mechanical property changes observed near these grain boundary regions.

This chapter is organized as follows. Section 6.2 provides a brief overview of the experimental protocols. The results and discussion are presented in Section 6.3 and the concluding remarks are given in Section 6.4.

6.2 Experimental methods

The moderately deformed (20% reduction in height) high purity aluminum sample used in the previous section was also used for this study. The sample, after being cut out from a rolled slab on high purity Al, was heat treated at 640°C for 72 hours to produce a fully annealed microstructure with very large grains. The sample was then compressed in a channel die to produce a 20% reduction in height and mounted in epoxy. Electropolishing was the final sample preparation step and it followed mechanical grinding and polishing. From the OIM map of the sample surface, eight high angle grain boundaries were selected for this study. With an aim to obtain better spatial resolution and also place as many indents as possible close to the grain boundary, a 20 μm spherical indenter tip was used in this case. Note that using a tip with an even smaller diameter increased the probability of the occurrence of pop-ins, which are undesirable and hence were avoided.

Indentation tests were performed along lines inclined to the grain boundary at shallow angles. The long grain boundary segments, which are a result of the large grains in our samples allowed us to place multiple rows of indents (6-9) close to the boundary. Each row contained 12 to 13 indents spaced 20 μm apart. This resulted in approximately 80 to 120 indents across each grain boundary. The large number of indents used in this

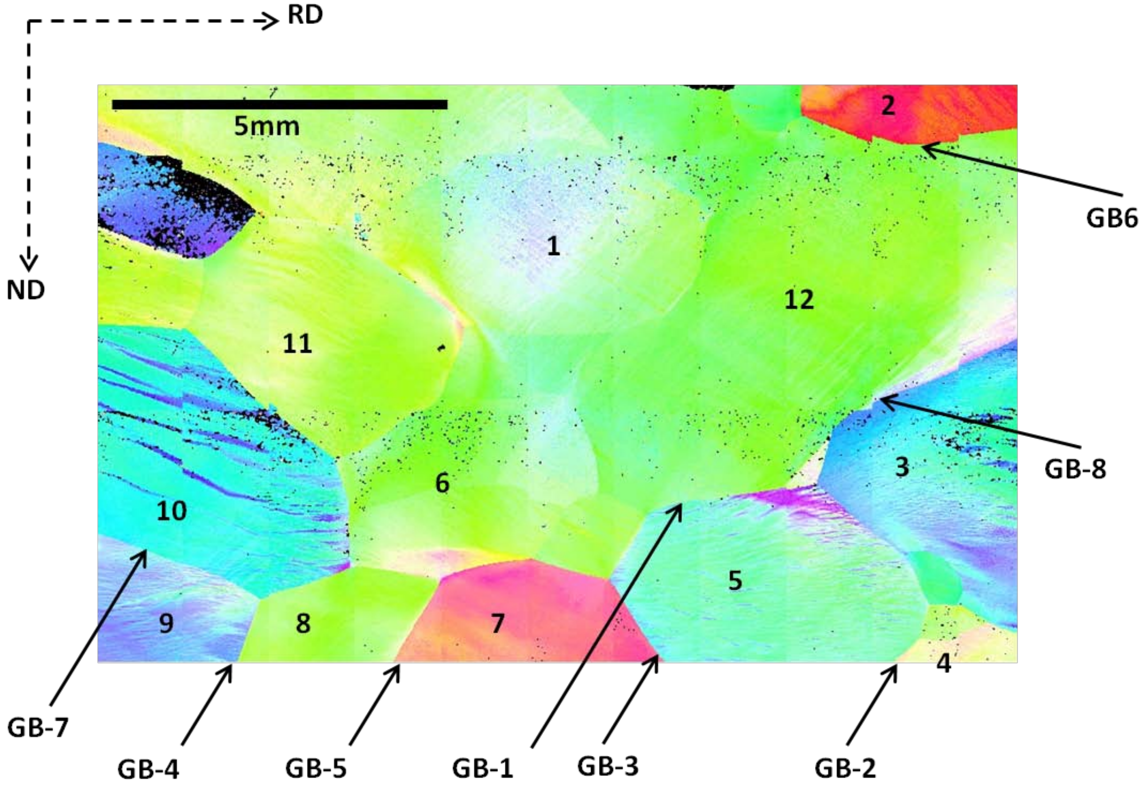

Figure 6.1: Overview of the sample deformed to 20% reduction in height, by plane strain compression showing the grain boundaries of interest, tested using nanoindentation. (Note that the steps seen in grain boundaries 5 (GB-5) and 6 (GB-6) are only artifacts that show up as the OIM image is a composite of many small scans)

study allows us to ensure that the mechanical trends observed in our investigations can be distinguished from the inherit noise in the nanoindentation response. It should be noted that such a high number of data-points would be almost impossible to obtain using other small-scale mechanical testing techniques such as micro-pillar testing. High resolution OIM maps as well as optical micrographs were obtained near the grain boundaries of interest after the indentations were performed in order to extract crystallographic information in the vicinity of the grain boundary as well as accurately determine the position of the indents with respect to the grain boundary. The perpendicular distance from the center of each indent to the grain boundary was calculated from these micrographs and will hence forth be referred to as the distance from the grain boundary, for the indentation in question.

6.3 Results and Discussion

The eight grain boundaries studied here are marked on the OIM map of the 20% deformed high purity aluminum sample shown in Figure 6.1. Each grain in the OIM map is color coded to represent its position on the standard [ND] inverse pole figure (IPF). In other words, the color represents the crystal direction in the grain that is perpendicular to the sample surface and parallel to the loading direction during the plane strain compression. Note however that the sample surface that was used for the nanoindentation testing is the TD section. The rolling direction (RD) for the section in the OIM map is horizontal and the normal direction (ND) is vertical.

About 80-120 indentation tests across each of the six boundaries were carried out and the raw indentation data was converted into indentation stress-strain curves. Representative indentation data for indents close to and far away from the boundary, for the two grains (Grain #5 and #12) on either side of grain boundary 1 (GB-1) is shown in Figure 6.2. As discussed previously in Section 4, pop-ins are absent for these indentation testes carried out using the 20 µm spherical tip because in these deformed samples it is relatively easy to set up the necessary dislocation sources using the existing network of forest dislocations. Also clear from this figure is the fact that, even for the same grain boundary, the grains on either side behave very differently in the immediate vicinity of the boundary as compared to the response measured away from the boundary. From the indentation stress-strain curves, the indentation yield strength is extracted as the indentation stress at 0.1% offset yield. As seen in Figure 6.2, for grain #5, there is little difference between the indentation response measured close to the grain boundary and away whereas on the other side of GB-1, in grain 12, the measured indentation stress-strain curve and the Y_{ind} are much higher in the immediate vicinity of the grain boundary than far away.

As in the case with the measurements discussed in the previous chapter, for each of the orientations tested close to the grain boundary regions, in the deformed condition, the expected indentation yield strength (Y_{ind}) in the fully annealed condition was extracted using the indentation yield surface presented in Figure 5.3. This is the indentation yield strength that would have been measured for the orientations in question, if they were tested in the fully annealed condition. It should be noted that in order to establish the indentation yield surface, a 100 µm spherical indenter tip was used whereas all the indentation measurements close to the boundary were performed using the 20 µm spherical tip (except GB-7 where the 100 µm tip was used, due to the unavailability of the 20 µm tip) . Effect of the indenter tip size on the nanoindentation response has been

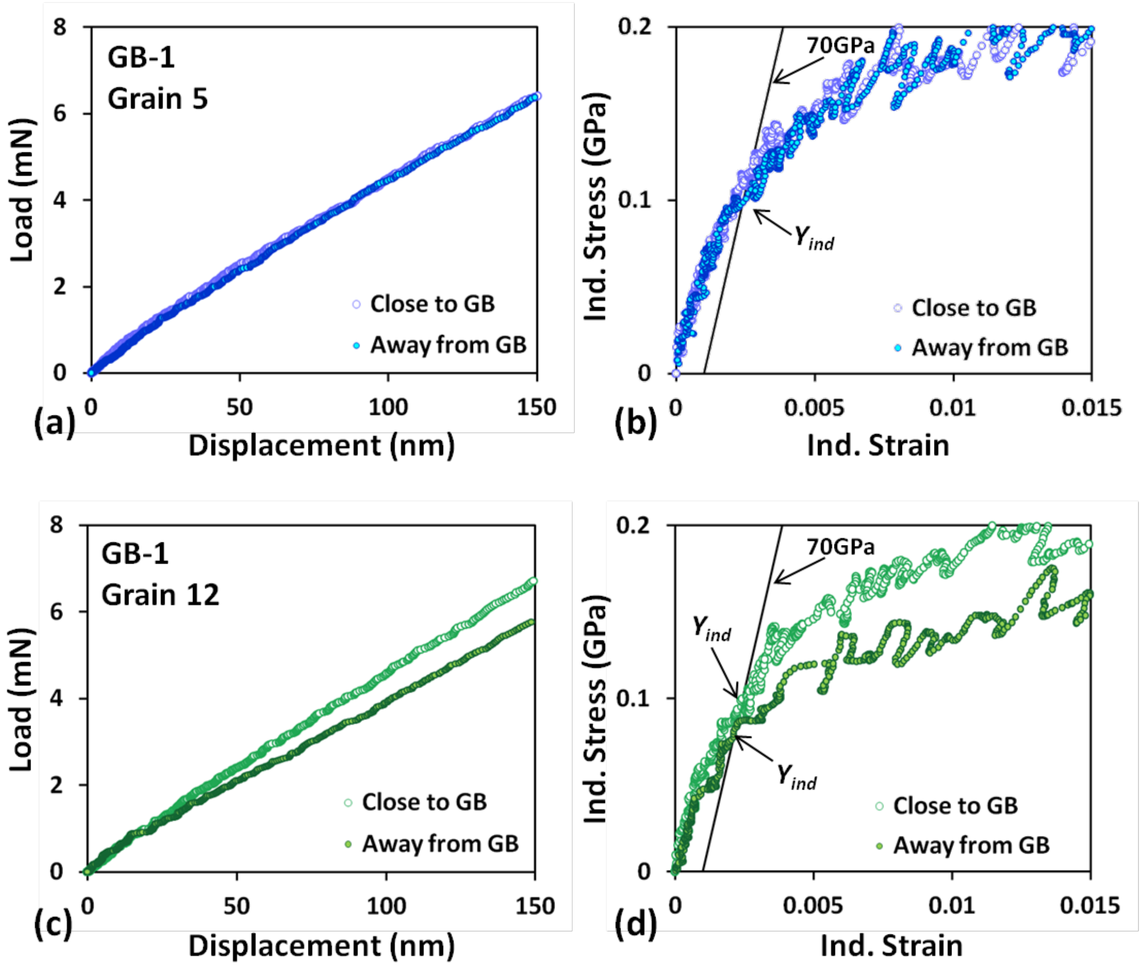

Figure 6.2: Representative(a) and (c) load-displacement curves and (b) and (d) corresponding indentation stress-strain curves obtained for grains 5 and 12 respectively, the vicinity of grain boundary 6 (GB-6). The open circles represent data from close to the boundary (>10 μm) and the closed circles represent data obtained away from the boundary (~40-50 μm).

discussed in Section 4 and in Figure 4.2, it has been shown that as far as the indentation yield strength is concerned, the size of the indenter tip used has little effect. The Y_{ind} values extracted for a given grain using the 20 µm and 100 µm spherical tips were in excellent agreement with one another, although the post elastic behavior is substantially different. Thus the indentation yield surface for high purity aluminum is not expected to change as a result of the change in the tip size used for the measurements. Using the measured indentation yield point ($Y_{ind}(g,d)$) in the deformed condition and the estimated $Y_{ind}(g,0)$ in the fully annealed condition, an estimate for the percentage increase in the indentation yield strength is obtained as in the previous chapter. Here d refers to the deformation step (20% reduction in height by plane strain compression) and g refers to the local crystal lattice orientation at the indentation site. As discussed in Section 5.3, the percentage increase in Y_{ind} provides an indirect measure of the local dislocation content or the local stored energy at the indentation site.

The indentation test results for six boundaries studied are summarized in Figures 6.3- 6.8. The interesting observations and finding of this work are highlighted through these figures. The OIM map showing the grain boundary, the orientation on a standard [ND] inverse pole figure map and the position of the indents with respect to the grain boundaries are provided for each grain boundary in Figure 6.3-6.8(a). The summaries of the measured Y_{ind} and the percentage increase in Y_{ind} due to the imposed macroscopic deformation are given in Figures 6.3-6.8 (b) and (c) respectively.

Table 6.1 summaries the details of the OIM and nanoindentation measurements away from the grain boundaries for the six boundaries of interest. The orientation away from the grain boundary represents the average orientation in the region of about 500 µm

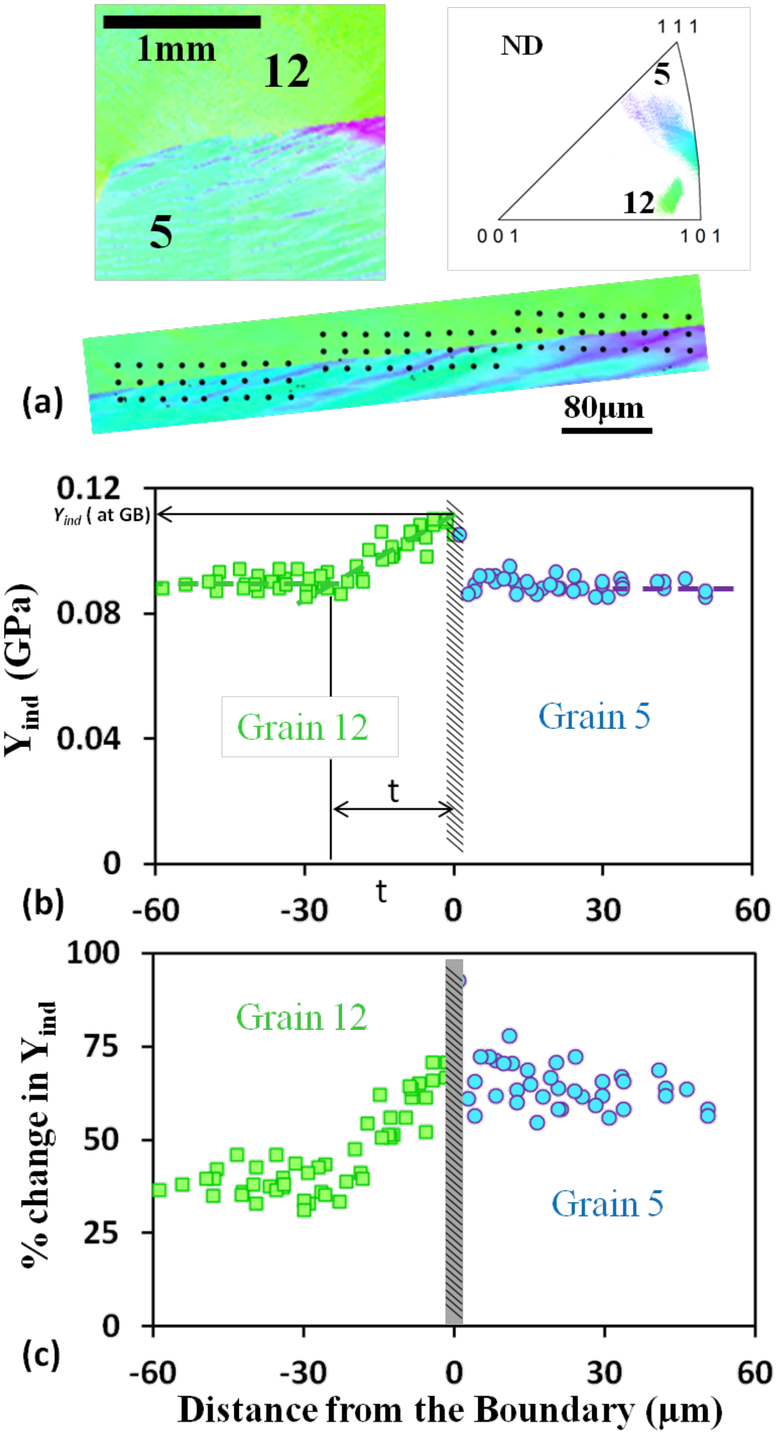

Figure 6.3: (a) Crystallographic details of the grain boundary 1 (GB-1) and the location of indents across the boundary. (b) The measured Yind across GB-6 between grain #12 and #5. (c) Percentage change in the Yind, with respect to the annealed condition.

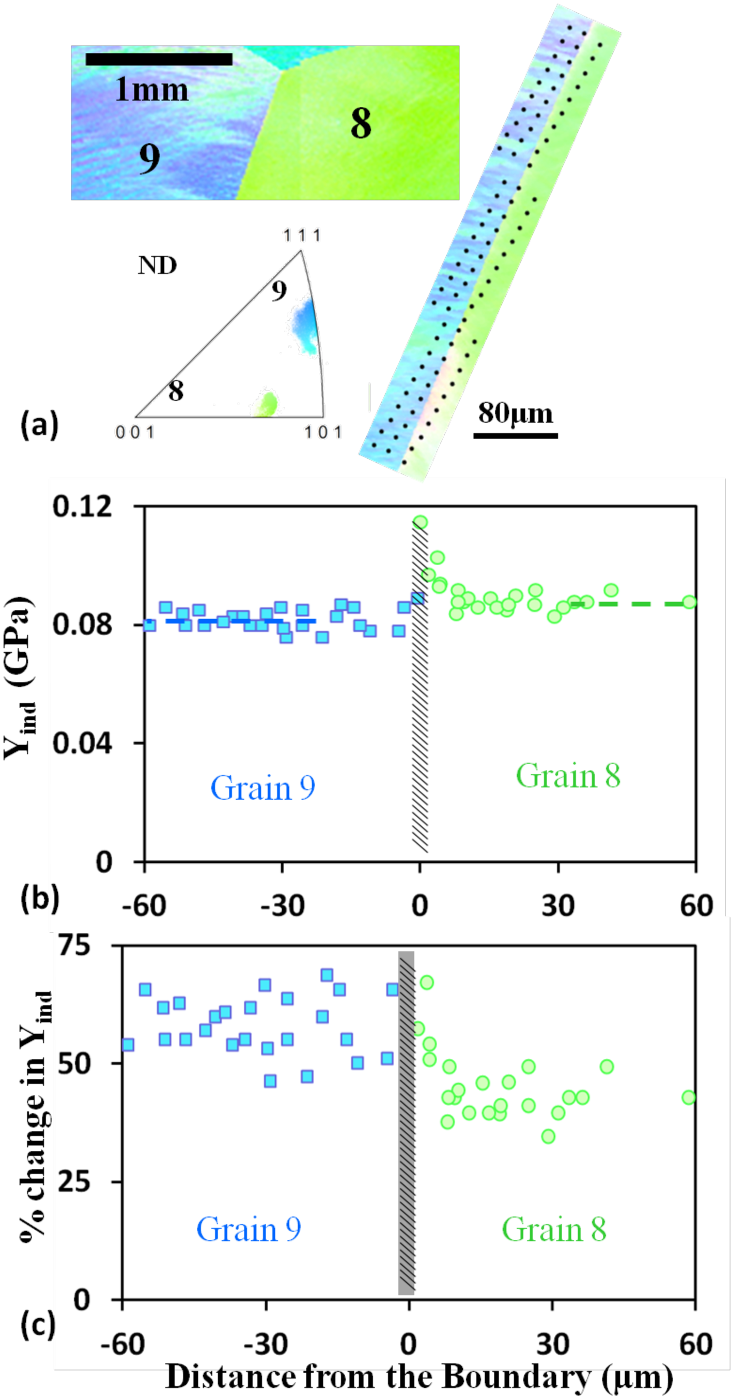

Figure 6.4: (a) Crystallographic details of the grain boundary 3 (GB-3) and the location of indents across the boundary. (b) The measured Yind across GB-3 between grain #9 and #8. (c) Percentage change in the Yind, with respect to the annealed condition.

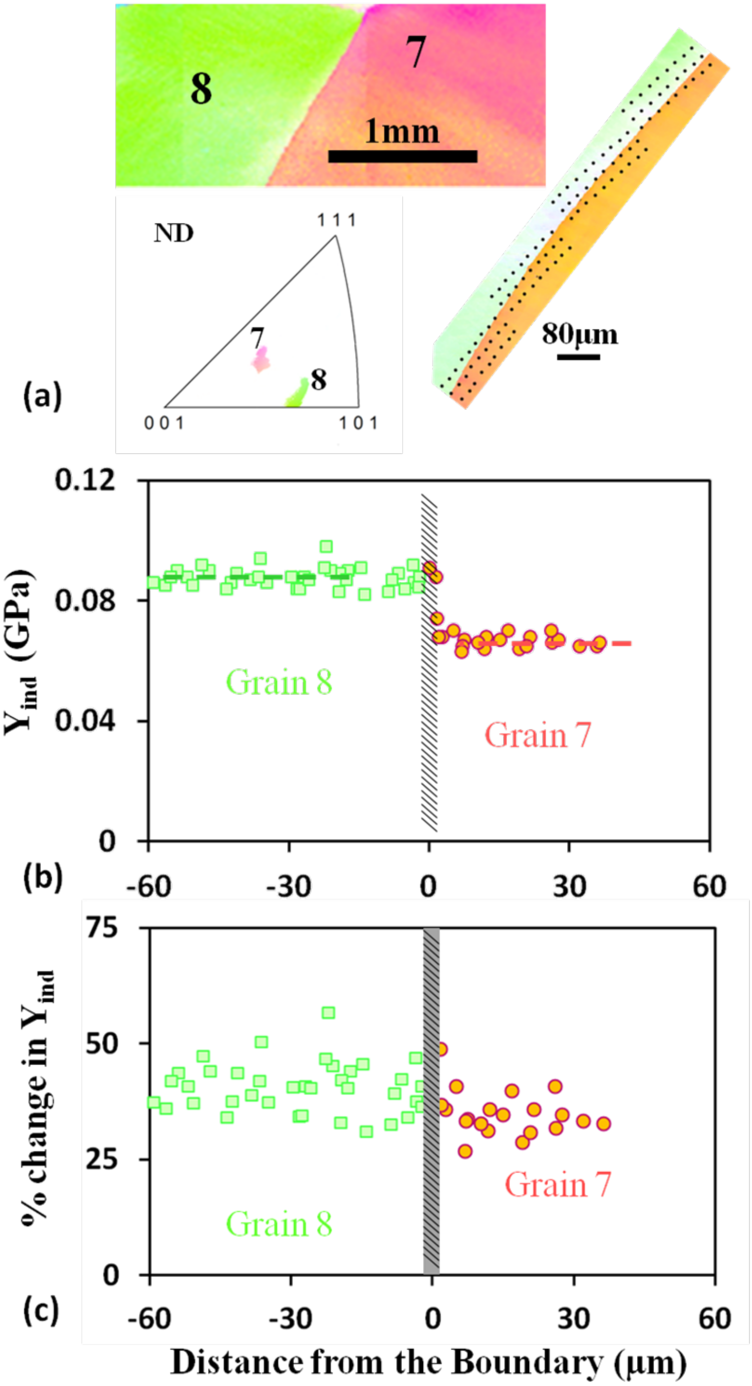

Figure 6.5: (a) Crystallographic details of the grain boundary 4 (GB-4) and the location of indents across the boundary. (b) The measured Yind across GB-2 between grain #8 and #7. (c) Percentage change in the Yind, with respect to the annealed condition.

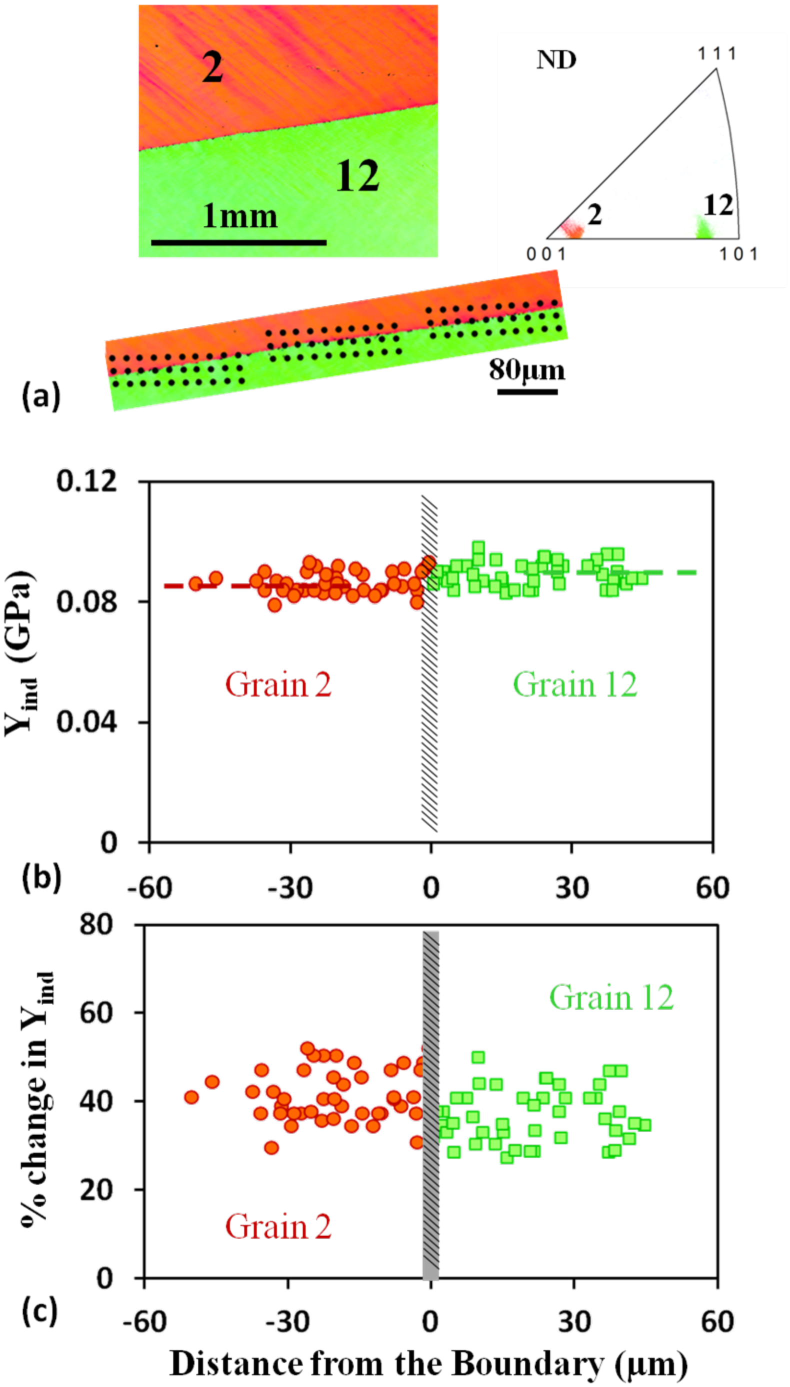

Figure 6.6: (a) Crystallographic details of the grain boundary 5 (GB-5) and the location of indents across the boundary. (b) The measured Yind across GB-1 between grain #2 and #12. (c) Percentage change in the Yind, with respect to the annealed condition.

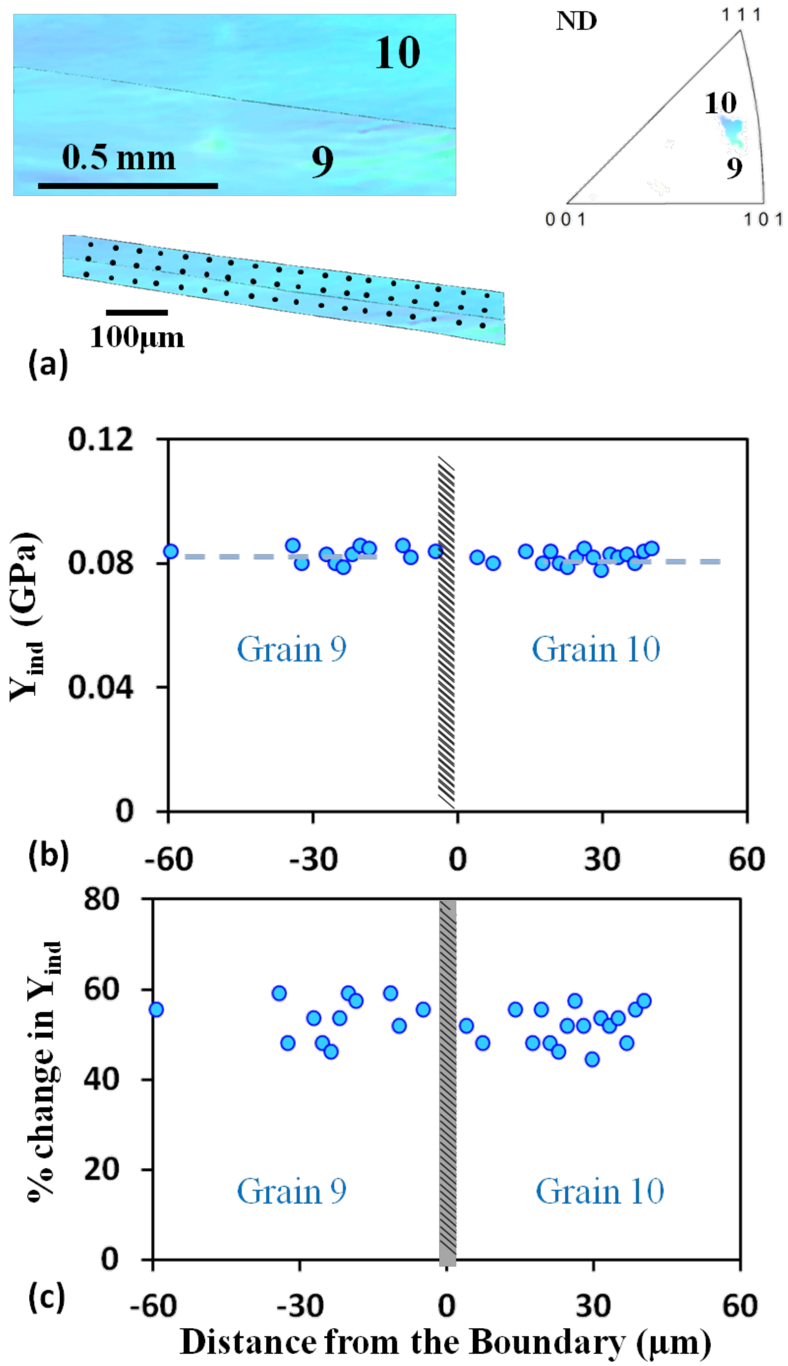

Figure 6.7: (a) Crystallographic details of the grain boundary 6 (GB-6) and the location of indents across the boundary. (b) The measured Yind across GB-5 between grain #12 and #3. (c) Percentage change in the Yind, with respect to the annealed condition.

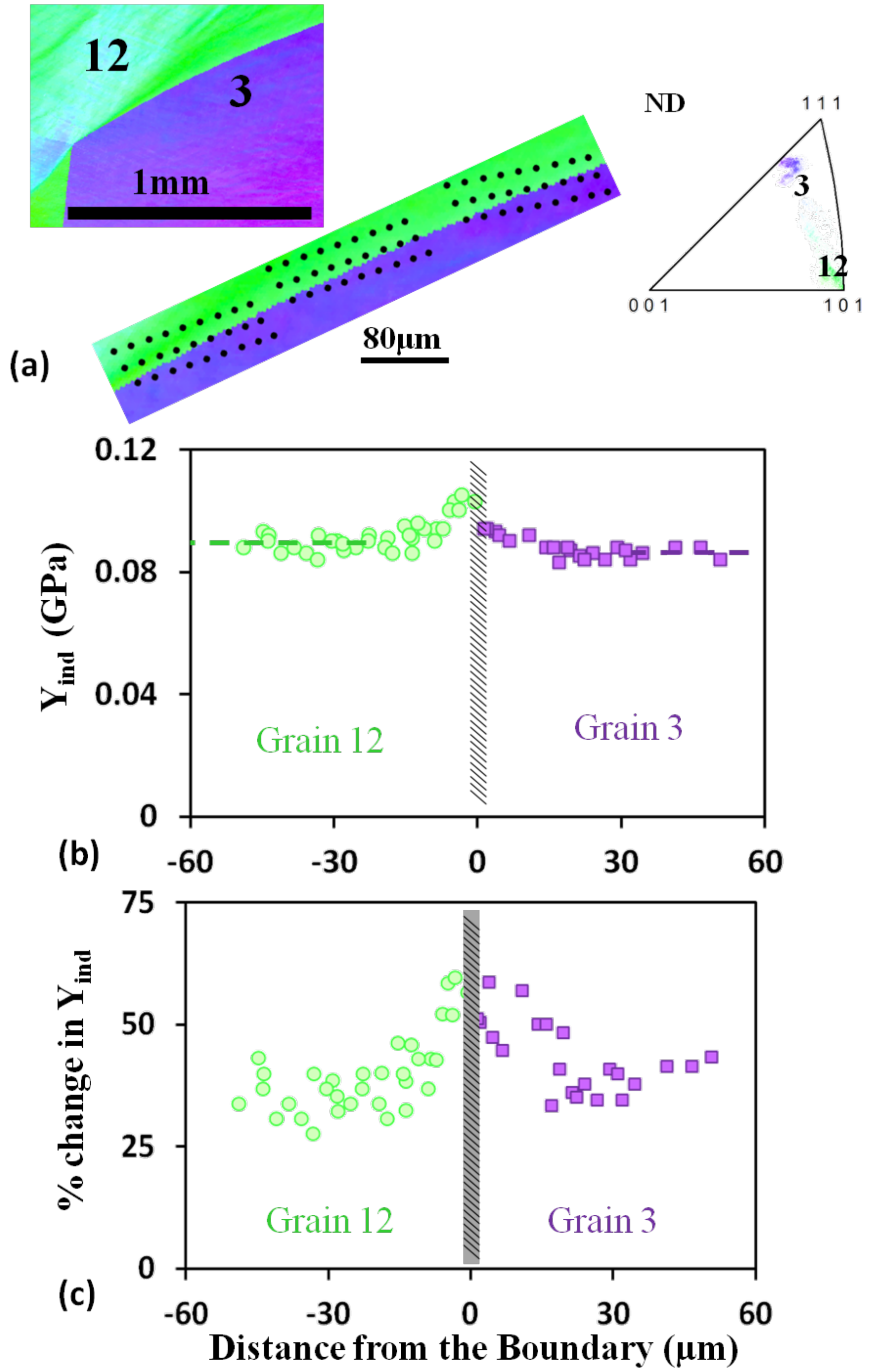

Figure 6.8: (a) Crystallographic details of the grain boundary 6 (GB-6) and the location of indents across the boundary. (b) The measured Yind across GB-5 between grain #12 and #3. (c) Percentage change in the Yind, with respect to the annealed condition.

around the grain boundary where the indentation tests were performed. Δg across the boundary is the minimum calculated misorientation between the average orientations measured in the region of about 500 µm on either side of the grain boundary and GOS represents the grain orientation spread measured in the same region. The Taylor factors presented are for plane strain compression calculated, again for the average orientations measured in the region of about 500 µm on either side of the grain boundary. Y_{ind} and the predicted Y_{ind} *(undef)* represent the indentation yield strength values measured within the grains (well away from the grain boundaries) and the indentation yield strength values extracted from Figure 4.3, which represent the expected Y_{ind}, if the orientations were tested in the fully annealed condition.

Table 6.2 summaries the details of the OIM and nanoindentation measurements in the vicinity of the grain boundaries, for the six boundaries of interest. The orientation at the grain boundary represents the average orientation in the region of about 60 µm around the grain boundary where the indentation tests were performed. Δg across the boundary is the minimum calculated misorientation between the average orientations measured in the region of about 60 µm on either side of the grain boundary. The Taylor factors (at GB) presented are for plane strain compression calculated for the average orientations in the grain boundary region and GOS

Table 6.1 (next page): Summary of OIM and nanoindentation measurements away from the grain boundaries, for the 8 grain boundaries studied in this work: Misorientation across the boundary, average grain orientation (with respect to the macroscopic deformation axes), Taylor factor and grain orientation spread (GOS) of each of the grains, the measured Y_{ind} away from the grain boundary and the predicted Y_{ind} for the orientation in the fully annealed condition

Grain Boundary	Δg across GB	Grain No.	Average Orientation			Taylor Factor	GOS	Yind	Predicted Yind (undef)
	(°)		φ1	Φ	φ2		(°)	GPa	GPa
GB-1	46.5	5	116.4	45.3	249.5	4.55	2.39	0.09	0.049
		12	149.1	40.1	176.1	2.80	1.82	0.089	0.066
GB-2	47.3	4	132.9	28.6	260.7	3.02	1.82	0.09	0.064
		5	69	42.7	286.1	4.65	2.37	0.09	0.049
GB-3	33.1	5	269.4	43.3	74.8	4.66	2.11	0.088	0.049
		7	110	25.3	245.8	3.37	1.54	0.066	0.048
GB-4	52	9	64.4	38.5	293.3	4.24	2.47	0.083	0.053
		8	144.4	33.1	255.2	3.11	3.02	0.0887	0.065
GB-5	39.1	7	91.9	17.4	275.5	3.37	1.78	0.067	0.048
		8	144.8	33.4	255.8	3.08	2.39	0.088	0.065
GB-6	29.6	2	143.9	7	184.9	2.34	2.28	0.087	0.063
		12	151.7	36.2	173.3	2.55	1.88	0.089	0.066
GB-7	11.8	8	117.5	41.5	245.7	3.97	0.085	0.082	0.053
		9	268.8	43	114.6	4.12	1.05	0.082	0.054
GB-8	45.6	3	210.3	42.3	138.6	4.03	2.65	0.085	0.056
		12	135.4	48.3	189.5	2.34	7.4	0.088	0.066

represents the grain orientation spread measured in the region of about 60 µm on either side of the grain boundary. Δg (center to GB) is the calculated misorientation between the average orientations away from the boundary (reported on Table 6.1) and average orientation in the grain boundary region (reported in Table 6.2). Y_{ind} *(undef)* represents the indentation yield strength values extracted from Figure 5.3, which represents the expected Y_{ind}, if the orientations at the grain boundary were tested in the fully annealed condition. Y_{ind} is the y-intercept for the best fit line through all the Y_{ind} values measured between 2 µm and 8-15 µm from the grain boundary, on a plot of Y_{ind} vs. distance from the boundary. The thickness of hardened layer is calculated as the distance from the grain boundary where the best fit line through all the Y_{ind} values measured between 2 µm and 8-15 µm from the grain boundary intersects the horizontal line that represents, on a plot of Y_{ind} vs. distance from the boundary plot, Y_{ind} (measured away from the boundary). Note here that the extrapolated value of Y_{ind} and the calculated thickness of the hardened layer are both strongly affected by the number of data points used for the interpolation and hence it is important to have a sufficiently large number of data points in the 'hardened region' in order to be confident about the numbers extracted.

From Figures 6.3-6.8 and Tables 6.1 and 6.2, it is clear that all grain boundaries do not behave in the same manner. For GB-1 (See Figure 6.3), there is a substantial transition zone on one side of the boundary where the measured values of Y_{ind} are higher than those measured within the grains (away from the boundary region). The immediate vicinity of GB-2, GB-3 and GB-4 (See Figure 6.4), also has a hardened layer, at least on one side of the grain boundary, although it appears to be significantly less pronounced as compared to GB-1. For GB-5 and GB-6 (See Figure 6.5 and 6.6), the presence of a grain boundary appears to have a negligible effect on the Y_{ind} values measured in the vicinity of the grain boundary. In other words, the Y_{ind} measured very close to the grain boundary is very similar to the Y_{ind} measured within the respective grains, well away from the boundary. All these boundaries (GB-1 to GB-6) were high angle grain boundaries. GB-7 is a low again grain boundary, and once again, the presence of a grain boundary appears to have a negligible effect on the Y_{ind} values measured in the vicinity of the grain boundary (See Figure 6.7).

From the Taylor factors in plane strain compression for each of the orientation of interest, it is seen that away from the grain boundaries, the orientations with a higher Taylor factor show more hardening as a result of the 20% height reduction. This is consistent with the findings reported previously in Chapter 5.

However, in the immediate vicinity of the grain boundary, a grain with a low Taylor factor (soft grain) when present next to a grain with relatively high Taylor factor (hard grain) showed much more hardening. The difference in the Taylor factor between adjacent grains is highest across GB-1, where grain #12 is a very soft grain with a Taylor factor of 2.80 next to a very hard grain (Taylor factor- 4.55). From Figure 6.3 and Table

Table 6.2 (next page): Summary of OIM and nanoindentation measurements near the grain boundary region, for the 8 grain boundaries studied in this work: Misorientation across the boundary, average crystal orientation (with respect to the macroscopic deformation axes), misorientation across the grain boundary, Taylor factor and grain orientation spread (GOS) on either side of the boundary, the predicted Y_{ind} for the orientation in the fully annealed condition, the extrapolated Y_{ind} at grain boundary and the thickness of the hardened layer after which the Y_{ind} is equal to that measured within the grain

Grain Boundary	Δg across GB	Grain No.	Average Orientation			Taylor Factor	GOS	Δg from center to GB	Yind (undef)	Yind (at GB)	Thickness of Hardened layer
	(°)		φ1	Φ	φ2		(°)	(°)	GPa	GPa	µm
GB-1	46.5	5	117.6	46.1	249	4.51	2.65	1.2	0.054	0.09	0
		12	155.3	39.8	170.5	2.64	1.35	3.6	0.066	0.11	27
GB-2	47.3	4	132.9	28.6	260.7	3.02	2.14	1.9	0.062	0.1	22
		5	69	42.7	286.1	4.65	2.18	1.3	0.048	0.09	0
GB-3	35.2	5	272.6	42.8	71.5	4.52	1.41	2.4	0.049	0.088	0
		7	111.3	25.5	244.6	3.41	1.47	0.6	0.049	0.073	16
GB-4	52	9	63	39.2	295.4	4.19	2.33	1.2	0.052	0.083	0
		8	144.22	32.2	254.3	3.11	2.45	1.3	0.065	0.098	7.5
GB-5	39.1	7	88.6	17.8	278.1	3.38	1.71	1.2	0.045	0.067	0
		8	148.2	32.3	251.1	3.11	2.11	2.5	0.066	0.088	0
GB-6	29.6	2	157.7	6.6	170.5	2.37	1.88	1.8	0.061	0.087	0
		12	147.2	37	178.5	2.74	1.49	3.1	0.066	0.089	0
GB-7	12.1	8	117.8	41.5	245.4	4.00	0.81	0.2	0.053	0.082	0
		9	268.4	42.6	114.9	4.08	0.88	0.6	0.055	0.082	0
GB-8	45.6	3	212.1	44.1	138.8	3.48	1.55	2.7	0.063	0.095	20
		12	144.1	44.7	180.3	3.09	5.92	7.9	0.066	0.104	17

6.1 and 6.2, it is also seen that grain #12, in the immediate vicinity of GB-1 shows the most significant amount of hardening both in terms of the percentage change in the Y_{ind} as well as the thickness of the hardened layer. GB-2, GB-3 and GB-4 show progressively lesser difference in the Taylor factors for the orientations on either side of the boundary and also progressively lesser amount of hardening on the 'soft grain' side. GB-5 has two moderately 'hard' grains of almost the same Taylor factor on either side of the boundary and GB-6 has two 'soft' grains of very similar Taylor factors next to each other. In both these cases, the hardened layer is completely absent. GB-7 is a low angle grain boundary with two relatively hard grains next to one another across the boundary. Consistent with previous observations, here again, there is little effect of the boundary on the hardening near the grain boundary. Note that all low angle grain boundaries will have grains of very similar orientation next to each other. The Taylor factors considered here are those calculated for the average orientations within the grains but note that the Taylor factor values close to the boundaries are not very different from these calculated for the grain interiors.

Figure 6.9 shows the variation of the thickness of the hardened layer in the 'soft' grain as well as the percentage increase in the indentation yield strength (Y_{ind}) with respect to the Y_{ind} measured in the grain interior as a function of the difference in the Taylor Factor of the grains on either side of the grain boundary in question. There appears to be a very strong relationship between the difference in Taylor factor at the grain boundary and the extent of hardening at the grain boundary. Although more data points need to be added to this plot in order to reliably quantify the relationship, this is a very important observation. It supports the hypothesis [42] of the presence of hardened layer at grain boundaries in deformed materials, due to the mismatch in the mechanical properties across the boundaries. The measurements reported in this work indicate that these hardened layers are predominantly on the side with the softer (lower Taylor factor) grain. Note that the thickness of the hardened layer observed near these grain boundaries is comparable to the average grain sizes in most commercially used metals and alloys. This would mean that if a majority of grain boundaries in a sample are between hard and soft grains, then there will be significant hardening within the entire soft grain, due to the presence of the boundary. Thus stored energy distributions within a deformed sample are likely to be strongly affected by the grain size in the material.

The observations for the case of GB-8 however, appears to be the exception to the trends discussed above. GB-8 has a soft grain #12 (Taylor factor - 2.34) adjacent to a hard grain #3 that has a Taylor factor of 4.03. However in this case, there is a significant hardened layer present on either side of the grain boundary. Interestingly, this grain boundary has a sharp curvature (See Figure 6.8) and significant spread in the orientation is observed close to this sharp bend in the boundary. Although indentation tests were performed at least 500 µm away from the curvature (measured along the boundary), the presence of the curvature is likely to have affected the deformation response in the region of the grain boundary that was tested. Also, grain #3 is present at the free surface during plane strain compression and consequently underwent significant shear. Note the significant spread in the orientation within the grain (See figure 6.1). A combination of these two factors is likely to have lead to GB-6 behaving differently compared to the trends seen in the other grain boundaries.

Measures of the grain orientation spread in the vicinity of the grain boundary and the calculated misorientations between the average orientations measured within the grains and in the vicinity of the boundaries (See Table 6.2) both seem to provide an indication of the presence of a hardened layer in the immediate vicinity of the boundary. This is not surprising because if the ‘soft’ grain is forced to undergo additional deformation in the immediate vicinity of the boundary, due to the presence of a ‘hard’ grain as in neighbor, the spread is the orientation is going to be larger due to the varying extent of deformation in the vicinity of the grain boundary. The difference in the dislocation activity in different regions near the boundary is likely to produce a larger spread in the orientations in this region. This additional deformation near the grain boundary region is also likely to change the orientation in this region as compared to the orientation within the grains and grains with a hardened boundary layer are therefore likely to have a higher degree of misorientation between orientation measured in grain and at the grain boundary regions. These measures are only indications and from Table 6.2 it is clear that there are exceptions to this trend. Long range interactions between neighboring grains, the stability of the orientation with respect to the imposed deformation etc are probably causes for this. A more detailed investigation involving a more uniform grain size distribution within the sample, larger number of boundaries as well as one where the grain orientations are tracked during the imposed macroscopic deformation will shed more light on this matter.

Note here again that the grains in these samples were grown after the samples were cut out. As the grains grow very large during the long annealing treatment (72 hours at 640°C), the grain boundaries, very close to the surfaces, will then be migrating very

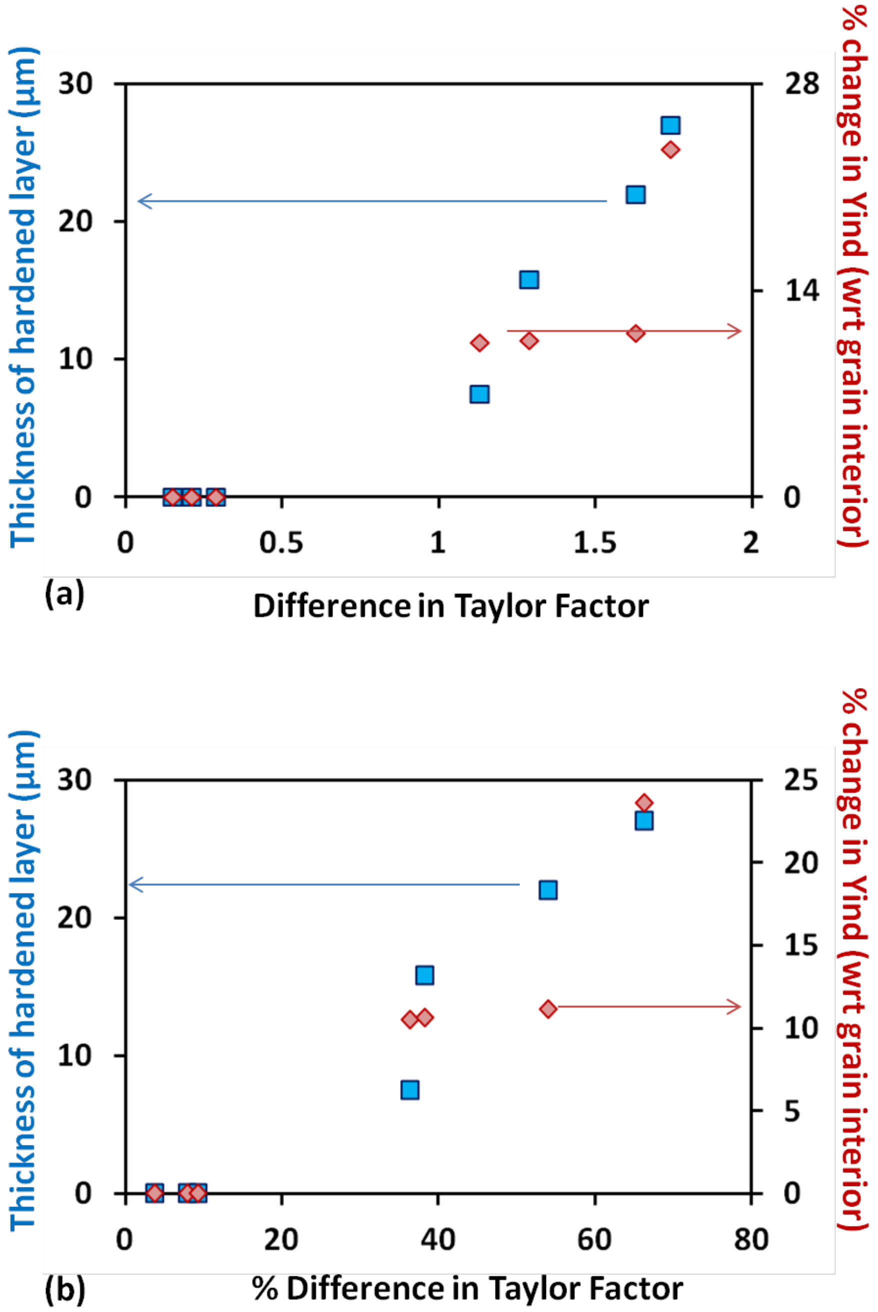

Figure 6.9: The variation of the thickness of the hardened layer and the percentage increase in the indentation yield strength (with respect to the grain interior) for the 'soft' grain for 5 grain boundaries (GB-1 to GB-5) as a function of (a) the difference in the Taylor factor for the two grain across the boundary and (b) the percentage difference in the Taylor factor for the two grain across the boundary.

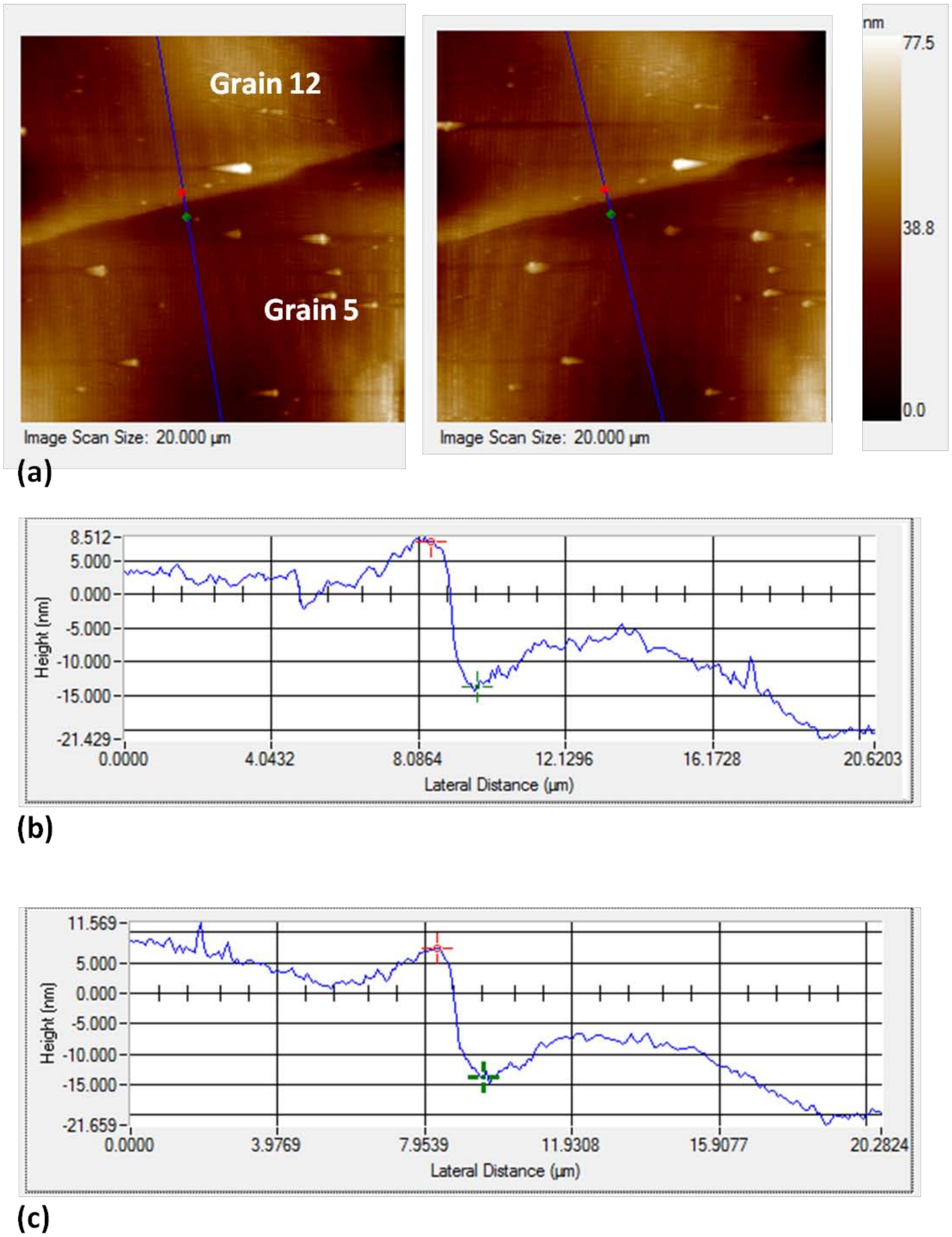

Figure 6.10: (a) Topology of the surface in the vicinity of GB-1 across grains #5 and #12. (The two profiles are generated as the probe scans right to left (forward) and left to right (reverse). (b) and (c) show the variation in surface height along the blue line (in (a)) across the boundary as measured during the forward and reverse scan respectively.

slowly and will have time to orient themselves at right angles to the free surface. Therefore we expect the grain boundaries we are investigating to be nominally perpendicular to the sample surface. This was also verified by removing a top layer of about 50 µm and re-imaging the sample surface using OIM. Thus, the possibility of a grain boundary being inclined to the sample surface is very remote. Another concern in the interpretation of the observed changes in local mechanical properties near the grain boundaries is that there might be artifacts resulting from curvatures on the sample surface at the grain boundary regions due to sample preparation, particularly, electropolishing. In order to verify this, the topography of the sample surface around two grain boundaries of interest (GB-1 and GB-5) was imaged with a sharp Berkovich tip using Hysitron's TI 950 TriboIndenter® in the SPM imaging mode. For both these boundaries, it was observed that the sample surface was very smooth and that the maximum height difference at the grain boundary was ~8 nm and occurred within a distance of ~2 µm around the boundary. The surface topography around GB-1 as measured by the SPM imaging is shown in Figure 6.10. Any data points affected by such steps (if present) at the boundary would lie within a region of ±1 µm from the grain boundary (grey-ed out on the plots and excluded during the analysis). This region of ±1 µm from the boundary is also the region where the indentation zone at the point of yield might be directly intersecting the grain boundary which makes the interpretation of tests within these regions difficult.

6.4 Conclusions

In summary, a novel approach to characterizing the mechanical behavior of grain boundary regions in deformed polycrystalline materials using spherical nanoindentation is used in this study to investigate regions around eight grain boundaries. From percentage changes in the indentation yield strengths measured as a function of distance from the boundary, it is concluded that ‘soft’ grains when present next to ‘hard’ grain harden significantly more in the immediate vicinity of the boundary. The extent of hardening increases with the increase in the difference in the Taylor factor for the adjacent grains. In other words, spatial variations in stored energy are significant in the vicinity of the boundary when a ‘hard’ grain is present adjacent to a ‘soft’ one. However, sharp curvatures in the boundary or additional shear due to the proximity of a boundary to the free sample surface mask these trends.

CHAPTER 7

CONCLUSIONS

In this dissertation, a novel combination of spherical nanoindentation and orientation imaging microscopy has been used to gain insights into the local structure-mechanical property relations in face centered cubic (fcc) metals. This work was made feasible due to the recent advances in the nanoindentation data analysis procedures that capture various aspects of the elastic-plastic material response more reliably compared to conventional nanoindentation data analysis protocols. This advancement was leveraged, in this work, to quantify subtle changes in the mechanical properties at a sub-micron length scale. Orientation imaging microscopy (OIM) was used as a very effective complimentary technique to obtain information about local structure at and near the indentation site. Using this combination of nanoindentation and OIM, effect of the local structure on its mechanical properties was studied for high purity aluminum after different levels of deformation. Structure-property correlations in the undeformed state were used as a baseline to gain insights into the evolution of stored energies in this material, as a result of the imposed macroscopic deformation. The main concepts and findings of this dissertation are summarized below:

i. The Continuous Stiffness Measurement (CSM) is central to the new nanoindentation data analysis procedures, to convert raw nanoindentation load–displacement data into indentation stress–strain (ISS) curves and therefore, the effect of the CSM on the indentation stress-strain curves during spherical nanoindentation was critically examined. From tests on pure aluminum and fused silica, it was concluded that the amplitude and frequency of the superimposed oscillations in the CSM affected the harmonic stiffness signal (S) most significantly, owing to the machine dynamics and the characteristics of the data collection system. The phase angle between the harmonic displacement and harmonic load is expected to be near zero for elastic oscillations and is used here as an indicator for questionable measurements of the stiffness. The values for the harmonic stiffness are unreliable at lower oscillation frequencies, and the noise levels are very high for low oscillation amplitudes. Therefore, 45 Hz–2 nm oscillations in the CSM during nanoindentation testing appears to be the best option.

ii. The inherent dependence of the indentation yield strength (Y_{ind}) on the local crystal lattice orientation was documented for the first time by measuring the mechanical response at various locations of known crystal lattice orientation on a fully annealed aluminum sample and the variation of indentation yield strength (Y_{ind}) as a function of local crystal lattice orientation (indentation yield surface map) was established. It was seen that the Y_{ind} can vary by as much as 40% depending on the local crystal orientation. Quantifying the contribution of lattice orientation to the measured Y_{ind} is necessary to reliably estimate the specific contribution of the changes in dislocation density to the Y_{ind}.

iii. Using percentage change in the Y_{ind} as an indicator of local dislocation density, it was concluded that after light (10% reduction in height) and moderate (20% reduction in height) deformation, grains with a higher Taylor factor have higher stored energy content as compared to grains with a lower Taylor factor. While significant scatter is observed for measurements on the deformed samples, the trends are fairly clear. Although this relationship between Taylor factor and local stored energy of deformation has been hypothesized by many researchers in the past, there has been little direct experimental evidence to show it. To the best of the author's knowledge, this is the first time a rich dataset showing a strong relationship between local stored energies and Taylor factors has been documented.

iv. Using the same experimental approach, regions near grain boundaries in a moderately deformed high purity aluminum sample were investigated in order to gain insights into the role of grain boundaries in the development of stored energy gradients during deformation. Again, using percentage change in the Y_{ind} as an indicator of local stored energy, it was concluded that 'soft' grains when present next to 'hard' grain harden significantly more in the immediate vicinity of the boundary. The extent of hardening near the grain boundary increases with the increase in the difference in the Taylor factor for the adjacent grains. In other words, spatial variations in stored energy were significant in the vicinity of the boundary, on the side of the 'soft' grain, when it was present adjacent to a 'hard' one. When both grains on either side of the boundary had similar values of Taylor factor, no additional hardening at the grain boundary was observed. It was shown that there is a fairly strong correlation between the extent of hardening (both in terms of the thickness of the hardened layer adjacent to the boundary and in terms of the percentage increase in the Y_{ind}) and the difference in the Taylor factor across the grain boundary. This is a very important observation, as it is generally expected that low angle grain boundaries have little effect on deformation behavior. Here, it is shown that the Taylor Factor determines the effect of a grain boundary and not the misorientation across the boundary. However, sharp curvatures in the grain boundary and additional deformation due to the proximity to the grains of interest to the sample surface leads to behavior that deviates from this trend.

v. The observation that orientations with lower Taylor factors have lower stored energies and that there are stronger stored energy gradients at boundaries between hard and soft grains in a deformed sample might also shed some new light on the 'laws of recrystallization': (i) orientations with a lower Taylor factor are likely to form recrystallization nuclei, and (ii) in material that has a lot of grain boundaries between hard and soft grains, there will be many more nuclei and therefore a smaller recrystallization grain size (and also easier recrystallization), whereas a sample with more of a uniform Taylor factor (irrespective of whether it is high or low) will produce less nuclei (therefore a larger recrystallized grain size).. This might explain some of the existing gaps in the development of recrystallization textures in heavily deformed cubic metals.

CHAPTER 8

FUTURE WORK

Development of stored energy gradients within light and moderately deformed high purity aluminum sample have been successfully characterized in this work using a combination of spherical nanoindentation and orientation imaging microscopy. While this data has lead to significant advancement in our understanding of stored energy developments in metallic materials, in order to increase the confidence in the relationships established, particularly in the case of the work near grain boundaries, it will be useful to characterize regions around many (15-20) more boundaries. Equipped with this information, and using similar investigation techniques, insights into the process of recrystallization, particularly the location and orientation of the nuclei and newly formed recrystallized grains, can be obtained.

One of the major challenges in an investigation like this is that it is currently impractical to characterize the entire surface of the deformed sample, and on the other hand, our current understanding of recrystallization does not help in predicting where the regions of interest might be, with respect to nucleation activity. Also, the process of indentation testing introduces additional deformation that is likely to interfere with the subsequent recrystallization process. Additionally, once the sample is heated, there are significant changes in the microstructure and therefore, any and all information regarding the deformed structure prior to the heating is lost. A smart experimental design, either using a split sample geometry or splitting a sample after deformation, to obtain two surfaces that have microstructures that are mirror-images of one another, is proposed for future work. While one half can be heat treated to determine the regions of interest, the other half can be used to characterize the material in its as-deformed condition. This would be a very valuable study providing insights into the process of grain nucleation during recrystallization.

The work discussed in this dissertation has for the first time helped document the evolution of microstructure and local mechanical properties during macroscopic deformation with much more detail than ever before. The full potential of information such as this, can be realized when the experimental information, obtained using OIM and spherical nanoindentation is combined with modeling and simulation tools such as Finite element methods (FEM). Using data relating local mechanical properties (in the fully annealed condition and after macroscopic deformation) as a function of local orientation in deformed materials together with Crystal Plasticity Finite Element Models (CPFEM), slip resistances and hardening parameters for aluminum can potentially be extracted following inverse methodologies. Lack of knowledge of crystal level plasticity parameters is currently a major challenge in applying crystal plasticity theories for simulating the deformation behavior in metallic materials. In order to accomplish this, a systematic investigation that sheds light onto the relationships between properties extracted from spherical nanoindentation (both experimental and from simulations) and macroscale mechanical behavior is critical.

While the current research focuses only on metallic materials, the techniques for spherical nanoindentation testing developed and validated here are equally applicable to non-metallic materials such as ceramics, man-made and natural composite materials, etc. In fact, I have also applied the nanoindentation methodologies explained in this work to study the effect of local composition on the lamellar level mechanical properties in bone. In those studies, the local mechanical property information obtained from spherical nanoindentation was combined with local composition information extracted using Raman spectroscopy. A brief summary of this work in presented in appendix-A. Thus, the proposed work is highly interdisciplinary and has applications in the mechanical, materials and biomedical engineering fields. The long term impact of this work is likely to result in better designed materials and processing routes, from which a very broad sector of the population would benefit.

APPENDIX A

ESTABLISHING CORRELATIONS BETWEEN LOCAL MECHANICAL PROPERTIES AND COMPOSITION IN INBRED MOUSE FEMUR

A.1 Introduction

This Chapter provides a brief overview of the application of spherical nanoindentation methodologies together with Raman Spectroscopy measurements to obtain insights into the correlations between the lamellar level composition in bone and its local mechanical behavior. Despite the fact that nanoindentation testing techniques are frequently utilized in characterizing the mechanical properties in bone, the inherent assumptions and limitations associated with the data analysis methods commonly used in literature prevent the use of this tool to successfully interrogate the local structure-property relationships [98]. As discussed in the main body of this dissertation, the newly developed methodologies [5] for spherical nanoindentation produces highly reliable and repeatable results and is a far more refined approach to studying local mechanical properties in bone using nanoindentation. Moreover, details of bone's matrix level organization (at length scales on the order of 1μm and below including details of collagen fibril and mineral crystal organization) have traditionally been difficult to characterize, as bone's mineral and collagen components are closely intertwined. Recent advances in characterization techniques such as Fourier Transform Infrared Microspectroscopy

(FTIR) [99-102] and Raman scattering spectroscopy (RS) [103-105] are opening new avenues of research that investigates mineral and collagen compositions as a function of anatomical location [7] in both normal and diseased bone [99, 106-108].

In this work, two species of genetically inbred mice (A/J and C57BL/6J, hereafter referred to as B6) were studied. One of the main reasons for selecting these strains is that these two strains show the maximum difference in their whole bone mechanical properties. Previous studies have demonstrated that A/J mouse bone has higher ash content than the B6 mouse bone, and while equally stiff, the A/J mouse bone has a higher yield point and more brittle post-yield behavior [109-111]. The growth patterns [111-112] in these mice strains are also well documented. The availability of all this knowledge makes these genetically inbred mouse strains an ideal model for studying the local composition - mechanical property relationships in bone. Five and six individuals each of A/J and B6 mouse strain respectively were used to study the tissue level differences in composition and local mechanical properties of these two strains. Specifically, the first aim of this study was to demonstrate the viability of these procedures for characterizing complex relationships between mineral/matrix variation and tissue-level mechanical properties in bone The second aim was to determine if there was a statistically significant difference in the composition of the bone (as determined by Raman Spectroscopy) and if so, did these differences originate as the bone was being laid down or do they develop at later stages as bone matures. Was the higher ash content values previously identified in the A/J bones reflected in a higher average mineral to matrix ratio (as determined by Raman Spectroscopy) in the mouse bones? The third aim of this study was to determine whether localized differences in the composition (mineral to matrix ratio, mineral maturation and collagen cross-linking) at the depositional surfaces of the femoral cortex reflected localized variation in elastic behavior and indentation yield point.

A.2 Materials and Methods

A.2.1 Subjects and Samples

Samples of femora were obtained from A/J (N=5) and B6 (N=6) strains of genetically inbred mice at 16 weeks of age. A/J and B/6 mice were purchased from Jackson Laboratory (Bar Harbor, ME, USA) at 4–6 weeks of age, and then housed at the animal care facility of the Mount Sinai School of Medicine. They were maintained on a 12-hour light: dark cycle, fed a standard feed (Purina Laboratory Chow 5001; Purina Mills, St. Louis, MO, USA) and given water ad libitum. All mice were then sacrificed at 16 weeks of age. The Mount Sinai Institutional Animal Care and Use Committee approved all procedures for the treatment of mice. Analyses were carried out at the 16 week time-point because by this age, the mice have achieved their peak bone mass, inter-strain differences have already been established and slow, lamellar bone growth characterizes the endosteal and periosteal formative surfaces [111]. We chose one of these sites (the Antero-Medial or AM cortex) for our study. Here, the newest bone is present closest to the endosteal surface and as we progress away from this edge, we encounter older, more mature bone. The location of the section with respect to the femur length, the representative backscattered electron microscopy (BSEM) image of the cross section of the A/J mice bone and the region of interest for performing the Raman spectroscopy and nanoindentation measurements are shown in Figure A.1. Previous work by Jepsen et al. [109, 111] has shown that the two mice do not differ significantly in their cortical areas, meaning that the same amount of bone is distributed differently in these two mice strains. However, whole bone mechanical tests have shown that the A/J mouse femur exhibit overall stiffness and strength values that are very close to the B6 mice femur, although one would expect that the A/J mice femur would be less stiff, if the bone composition in these two mice were the same. Jepsen et al. [109-110] have hypothesized that the A/J mice compensates for their less efficient mechanical structure of the femur by altering the bone quality. This hypothesis is supported by the findings of other researchers who have reported higher mineral to matrix ratios (as measured by Fourier transform infra-red imaging (FTIR) [113-114] and a significantly higher whole bone ash content [110] in A/J mouse bone as compared to the B6 mouse.

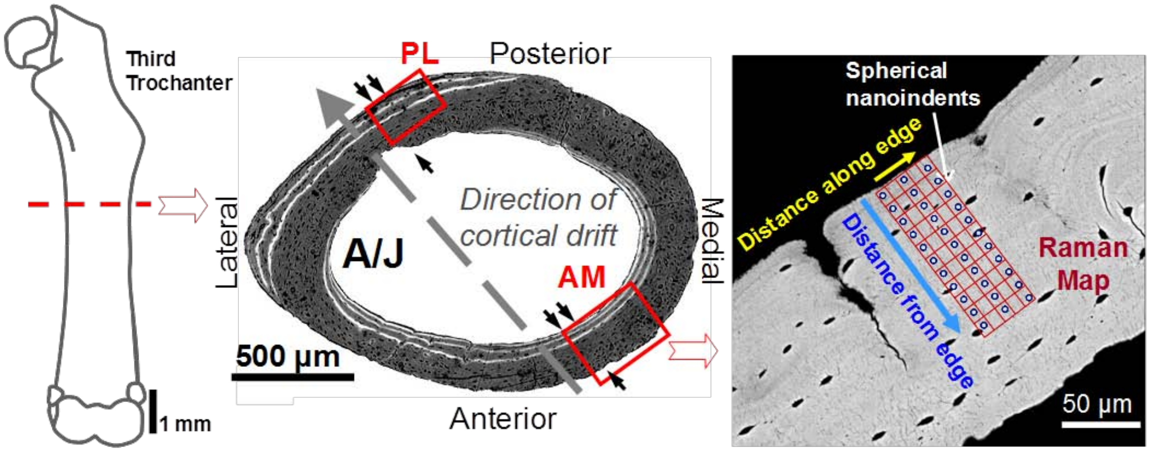

Figure A.1. For indentation testing the mouse femurs were sectioned transversely distal to the third trochanter. During post-natal growth, bone is deposited (double arrows) and resorbed (single arrows) at different sites around this region of the femoral cortex. Spherical nanoindents (shown as blue dots in the SEM image) at the antero-medial (AM) cortex thus probe newer bone closer to the endosteal edge while the bone is more mature away from this surface. Three rows of indentation were performed on each sample. The region surrounding the indents was mapped by Raman Spectroscopy (shown by the red grid around the indented region).

Right femora from A/J (n=5) and B6 (n=6) were harvested, cleaned of soft tissue and fixed in 70% ethanol, dehydrated in ascending grades of ethanol and embedded in polymethylmethacrylate (PMMA). A block of tissue was removed by sectioning the bone transversely just distal to the 3rd trochanter. The bone surface was prepared for Raman Spectroscopy and nanoindentation testing by grinding with increasingly fine sandpapers up to 1200 grit, and polishing by means of a series of napped cloth impregnated with diamond pastes, finishing with a grain size of 0.05μm. The samples were cleansed in a distilled water ultrasonic bath after each successive step.

A.2.2 Spherical Nanoindentation

The MTS nanoindenter XP® equipped with the CSM attachment was used to carry out the nanoindentation experiments. A spherical diamond tip of 13.5 μm was used to make indents of 300 nm nominal depth and the tip was held at maximum load for 10 seconds before unloading. Multiple rows of 15 indenters were made on each sample, starting from the endosteal surface of the AM cortex and proceeding radially inwards.

The raw nanoindentation data was converted into indentation stress-strain curves, following the methodologies developed by Kalidindi and Pathak in [5]. These methods are described in Section 2.4 and hence will not be detailed here. The elastic modulus values are calculated from the initial loading segment and from the indentation stress-strain curves, the indentation yield strength (Y_{ind}) is extracted as the stress at 0.2% offset strain.

A.2.3 Raman Spectroscopy

Each block surface was analyzed in a Renishaw 1000 Raman micro spectrometer using a semiconductor diode excitation laser operating at 785nm wavelength, to eliminate the auto-florescence of the bone proteins [115]. The 50x objective lens (NA = 0.75) provided a laser spot size of approximately 2 μm. Spectra were taken point by point in extended mode from 750cm^{-1} to 1800 cm^{-1} using a grating of 1200 I/mm. Initial tests were conducted using an interrogation time of 20s, where final spectrum of each spot was an average of three scans. A Renishaw silicon piece was used for x-calibration of the wave numbers of the Raman spectra with a sensitivity of less than 1 cm^{-1}. Care was taken not to focus the laser directly at the location of the indents, in order to ensure loss of focus and avoid scanning area damaged during the indentation process.

All analyses were performed using the Wire 2.0 Software. The spectra were divided into different sub regions for analysis based on methods used by Timlin et al. [116]. The first region was from 750-1150 cm^{-1} which contains bands arising from vibrations of the mineral component of bone, and the second region from 1170-1800 cm^{-1} which contains mostly bands from bone matrix. This pre-processing step reduced background effects and focused on the regions of the spectra where the signal was due to either mineral or matrix. After separation into the two sub regions, mineral and matrix, the data was further analyzed to subtract the background fluorescence using a baseline curve fit.

Compositional characteristics were obtained from peak intensities of the recorded spectra [61]. Peak intensity of the phosphate (~959 cm^{-1}), carbonate (1070 cm^{-1}), monohydrogen phosphate, Amide I (1616-1720 cm^{-1}) and CH_2 wag (1450 cm^{-1}) bands were analyzed following protocols described in our previous work [66, 101]. The phosphate to monohydrogen phosphate intensity ratios assessed as a measure of mineral maturity. Phosphate to carbonate peak intensity ratios were used to investigate substitutions in the lattice of apatite, providing a measure of mineral composition. The mineral to matrix ratio, which relates to bone mineralization density [117], was determined using the phosphate to CH_2 wag peak intensity ratio. Note that both the phosphate to CH_2 wag peak intensity ratio and the phosphate to Amide I band intensity ratio can be used to denote the mineral to matrix ratio. However, CH_2 wag band was more distinguishable in the Raman spectra, and ethanol fixation methods have been known to alter the Amide I band intensity, while the CH_2 wag intensity band is minimally affected by ethanol fixation [118]. Though PMMA bands do overlap the CH_2 wag band, the strongest peak of PMMA at ~820 cm^{-1} was only minimally observed in the bone spectra, its effects were therefore considered negligible and no extra processing steps were taken to eliminate the effects of PMMA on the spectra.

In order to accurately determine the local bone composition as a function of the distance from the edge of the bone, the location of the bone edge on the Raman grid was first determined. For each row of data in the scan, the PMMA-bone interface was determined as the positions were the linearly interpolated P-CH_2 wag ratio reached a critical value of 1. The cut off value of 1 was determined by super imposing the Raman Spectroscopy data on the optical images for the corresponding scan locations, in cases where the optical images had a clear and sharp PMMA-bone interface, to determine the P-CH_2 wag ratios obtained in the PMMA regions (which are always lower than any values obtained inside the bone). However, optical Images alone could not be used for bone edge determination as in some of the images the PMMA-bone interface was not sharp and hence hard to accurately determine. The P-CH_2 wag ratio was selected as the metric since these ratios had consistently low values outside the bone and then gradually

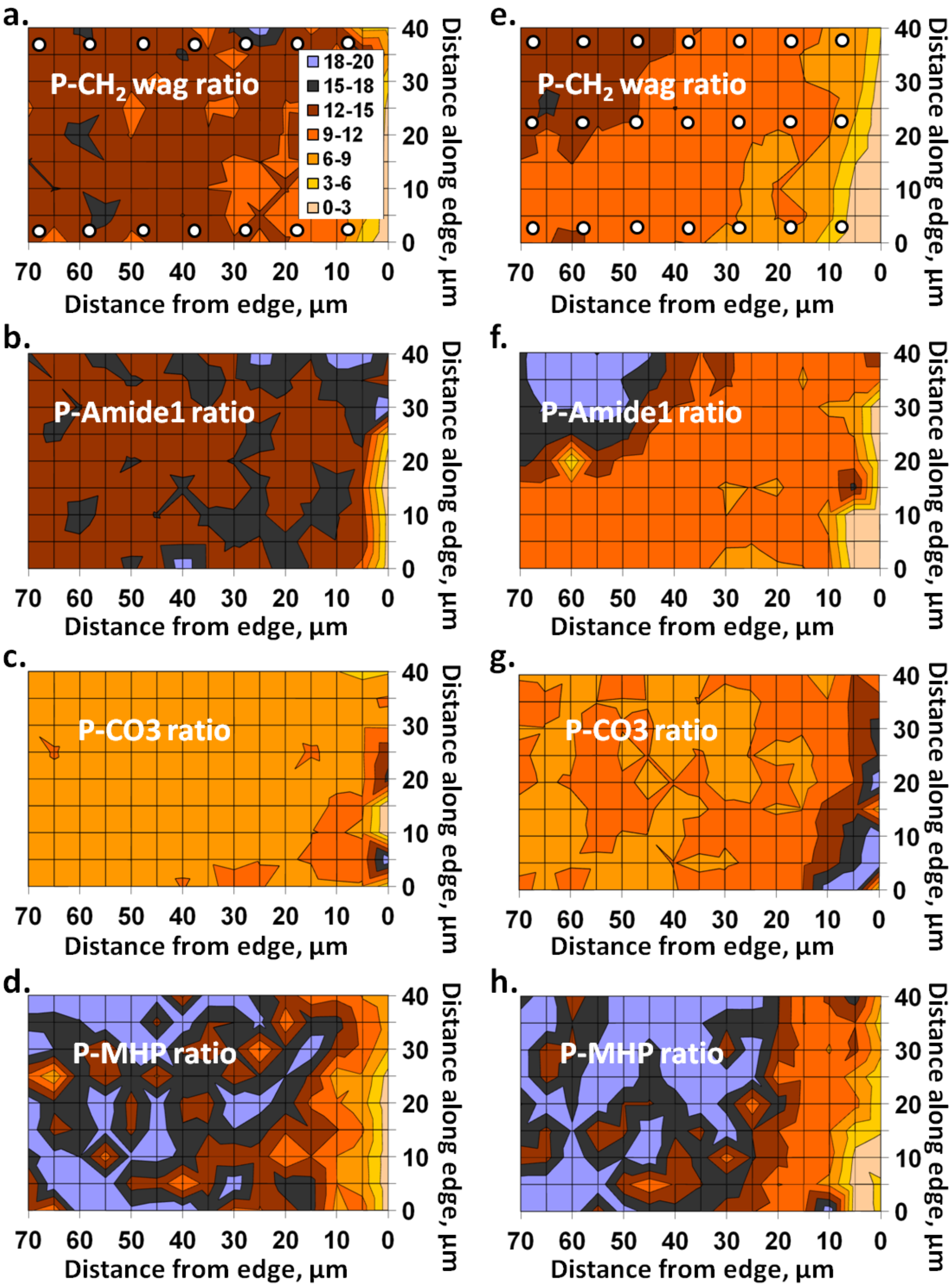
a.
P-CH$_2$ wag ratio
🟦 18-20
■ 15-18
■ 12-15
■ 9-12
■ 6-9
■ 3-6
■ 0-3
e.
P-CH$_2$ wag ratio
b.
P-Amide1 ratio
f.
P-Amide1 ratio
c.
P-CO3 ratio
g.
P-CO3 ratio
d.
P-MHP ratio
h.
P-MHP ratio
70 60 50 40 30 20 10 0
Distance from edge, µm
0 10 20 30 40
Distance along edge, µm

Figure A.2 (previous page). Representative 2D surface maps obtained using Raman spectroscopy, showing the various aspects of the composition information extracted from a scan over a 70μm by 40μm region close to the endosteal edge of the AM cortex of (a-d) A/J mouse and (e-h) B6 mouse sample. The figure about show the Phosphate to CH2 wag peak intensity ratio for (a) A/J and (e) B6 mice, Phosphate to Amide1 peak intensity ratio for (b) A/J and (f) B6 mice, Phosphate to CO3 peak intensity ratio for (c) A/J and (f) B6 mice and Phosphate to mono-hydrogen phosphate peak intensity ratio for (d) A/J and (g) B6 mice. The white circles in (a) and (e) denote the approximate size and location of the indentations with respect to the Raman map.

increased rapidly away from the bone edge (from the new bone region to the old bone region). Use of the P-amide I ratios for determining the edge instead of the P-CH2 wag did not alter the edge position significantly.

A.3 Results

Representative Raman maps, detailing the different aspects of the local bone composition in the two mouse strains are shown in Figure A.2. Figures A.2(a) and (e) show the variation in the mineral-to-matrix ratio, defined as the phosphate to CH_2 wag peak intensity ratio, in the antero-medial (AM) cortex of the A/J and B6 mouse femur respectively. The while circles in Figures A.2(a) and (e) represent the approximate position and size of the indents. Figure 2 also shows the variation in the phosphate to Amide-1, phosphate to CO3 (which is a measure of the mineral composition) and phosphate to MHP peak intensity ratios (which represents mineral maturity) calculated from the Raman data in two representative samples, one of A/J mouse and one for B6. From these Raman measurements, it is evident that the both mice strains show lower values of mineral-to matrix ratio close to the edge. The mineral is less mature and has a

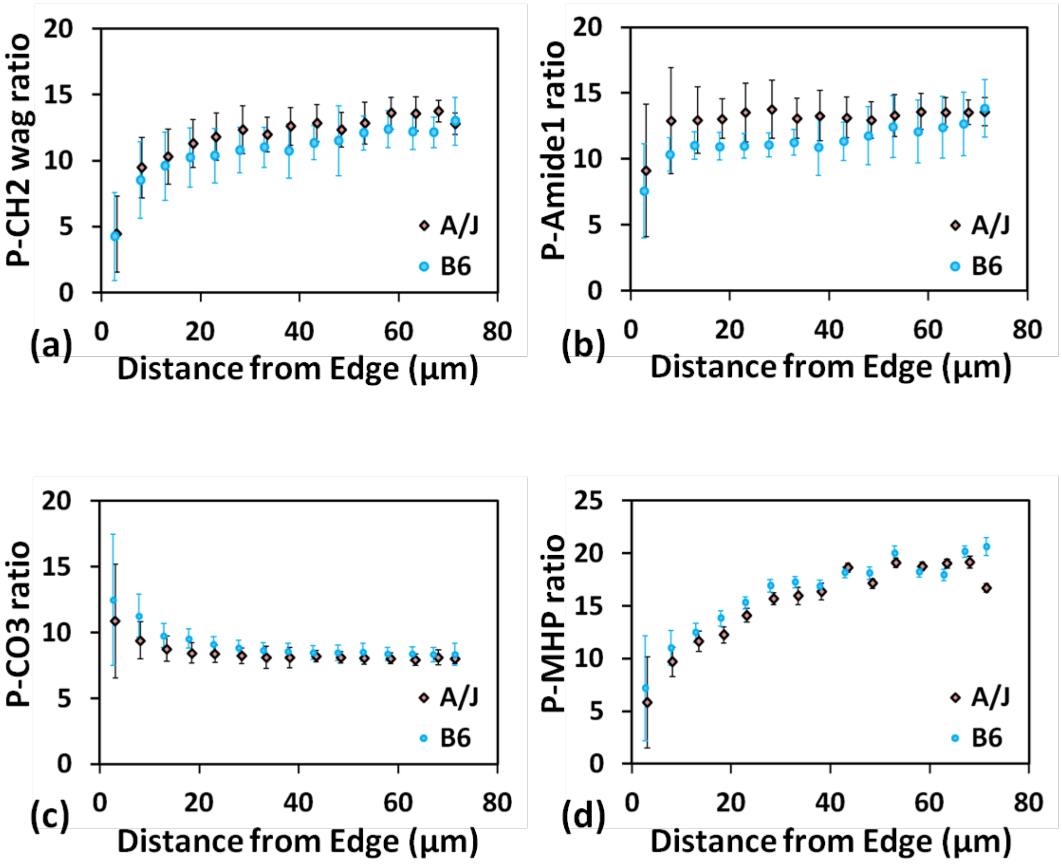

Figure A.3. Variation in the composition of bone, (a) Phosphate to CH2 wag peak intensity ratio, (b) Phosphate to Amide1 peak intensity ratio, (c) Phosphate to CO3 peak intensity ratio and (d) Phosphate to mono-hydrogen phosphate peak intensity ratio, with respect to distance from the edge, determined by averaging measurements along the bone edge and across the various samples characterized using Raman Spectroscopy. For clarity, the mean and standard deviation values for each 1µm bin, starting from 0µm from the edge for the bone is shown here.

higher degree of carbonate substitution close to the edge. Also, at a similar distance from the endosteal edge of the bone, the A/J mice shows higher values for the mineral to matrix ratio as well as bone maturity accompanied with lower degree of carbonate substitution in the mineral.

Figure A.3 shows the averaged variation in the bone composition as a function of distance from the endosteal edge for A/J and B6 mice, calculated using all the data from 5 and 6 individuals of the A/J and B6 mouse strain respectively . For clarity and better visualization, the data was grouped into bins of 1 μm, starting at 0 μm from the edge of the bone. The average and standard deviation values for each bin are used in the plots. For the statistical analysis however, the entire dataset was used and no averaging was performed.

Figure A.4 shows representative indentation load-displacement (Figure A.4(a)) and indentation stress–strain curves (Figure A.4(b)) for the two mouse strains. Tests from two indent locations in each strain are shown as examples of the material behavior close to (at a distance of around 12 μm) and far (around 42 μm) from the endosteal edge. These representative indents help demonstrate a similar trend to that of the Raman measurements; thus the bone tissue close to the endosteal edge shows lower sample modulus (E_s) and indentation yield (Y_{ind}) values, while both these values increase as the indenter probes more intracortical regions. The A/J mice also demonstrate larger values of E_s and Y_{ind} than the B6 at similar locations. As mentioned earlier, E_s in these figures is calculated from the initial loading segment of the indentation experiment while Y_{ind} is calculated using a 0.2% offset strain. Note that these differences are better captured by the indentation stress–strain curves in Fig Figure A.4(b) than they are by the raw load-

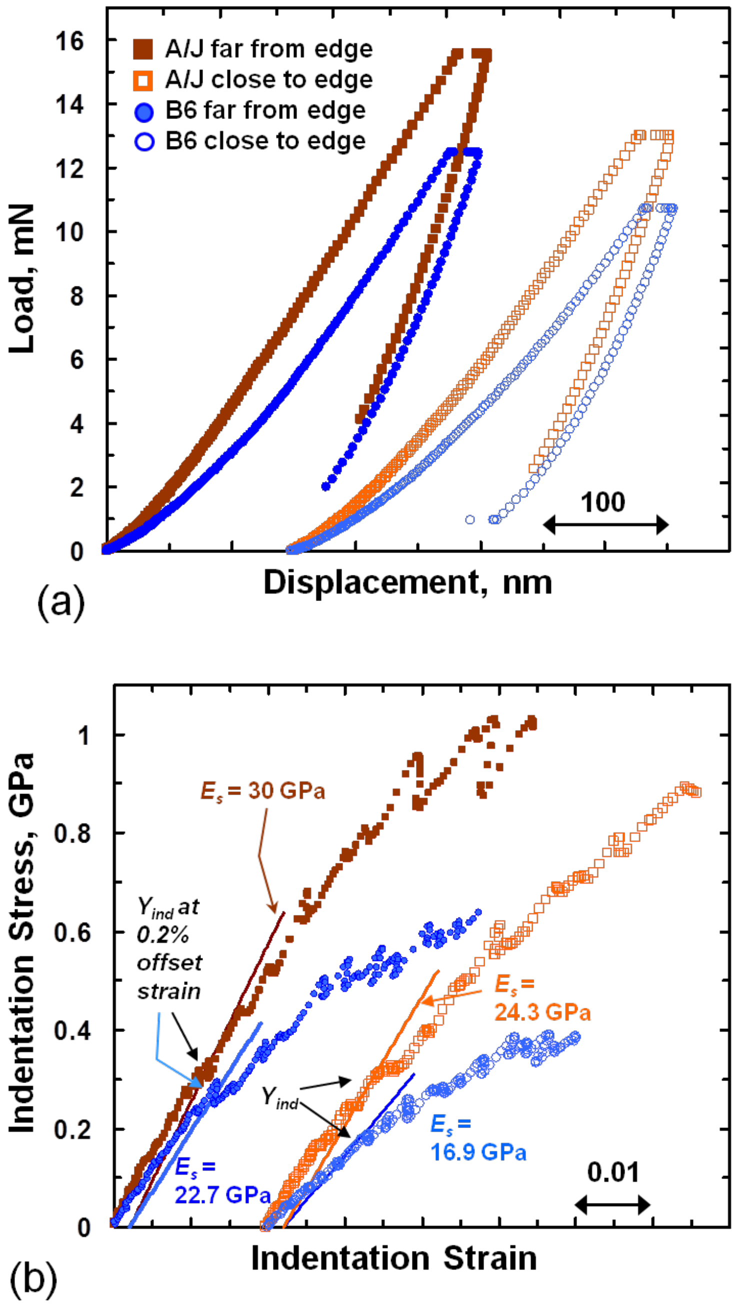

Figure A.4: Representative (a) load-displacement and (b) indentation stress-strain curves from A/J and B6 femur samples showing the differences in mechanical response between regions near and far from the endosteal edge of the respective AM cortices. (b) also shows our procedure for calculating Yind at 0.2% offset strain from the indentation stress-strain curves.

displacement data in Figure A.4(a). The A/J mouse bone also appears to show a higher hardening tendency in their post-yield region than the B6.

The trends shown in the Raman and the spherical nanoindentation measurements are illustrated further in Figure A.5, where the mineral to matrix ratios across a representative row of indents in A/J-5 and B6-5 are plotted along with the associated sample indentation modulus (E_s) and the indentation yield (Y_{ind}) values. These data suggest that both the local chemical composition (in terms of the mineral-to-matrix ratio) and the local mechanical behavior (E_s and Y_{ind}) of bone follow a similar pattern as a function of distance from the endosteal edge. Thus a lower mineral to matrix ratio close to the edge results in a lower indentation modulus and yield behavior at similar locations, while all three increase with increasing distances from the edge before stabilizing at their higher values. Concurrently, at a similar distance from the endosteal edge, the A/J mouse is seen to exhibit a slightly higher response for all three parameters as compared to B6.

Figure A.6 summarizes the indentation results on two A/J and three B6 samples, along with their associated Raman measurements. Figure A.6(a) shows a scatter plot of the elastic modulus, measured from the initial loading segment of the indentation stress–strain curves as a function of the mineral-to-matrix ratio measured by Raman spectroscopy. The variables in this figure show a strong, approximately linear, relationship, although some outliers do exist at the lower values. Since the A/J samples show a much more rapid increase in their mineral-to-matrix ratio (seen before in Figs. 5 and 7), there are far fewer data points for A/J in the mid-section of the scatter plot, as compared to B6. The A/J mouse samples also show the highest values of both the modulus and the mineral-to-matrix ratio. Figure A.6 (b) illustrates the modulus data, this

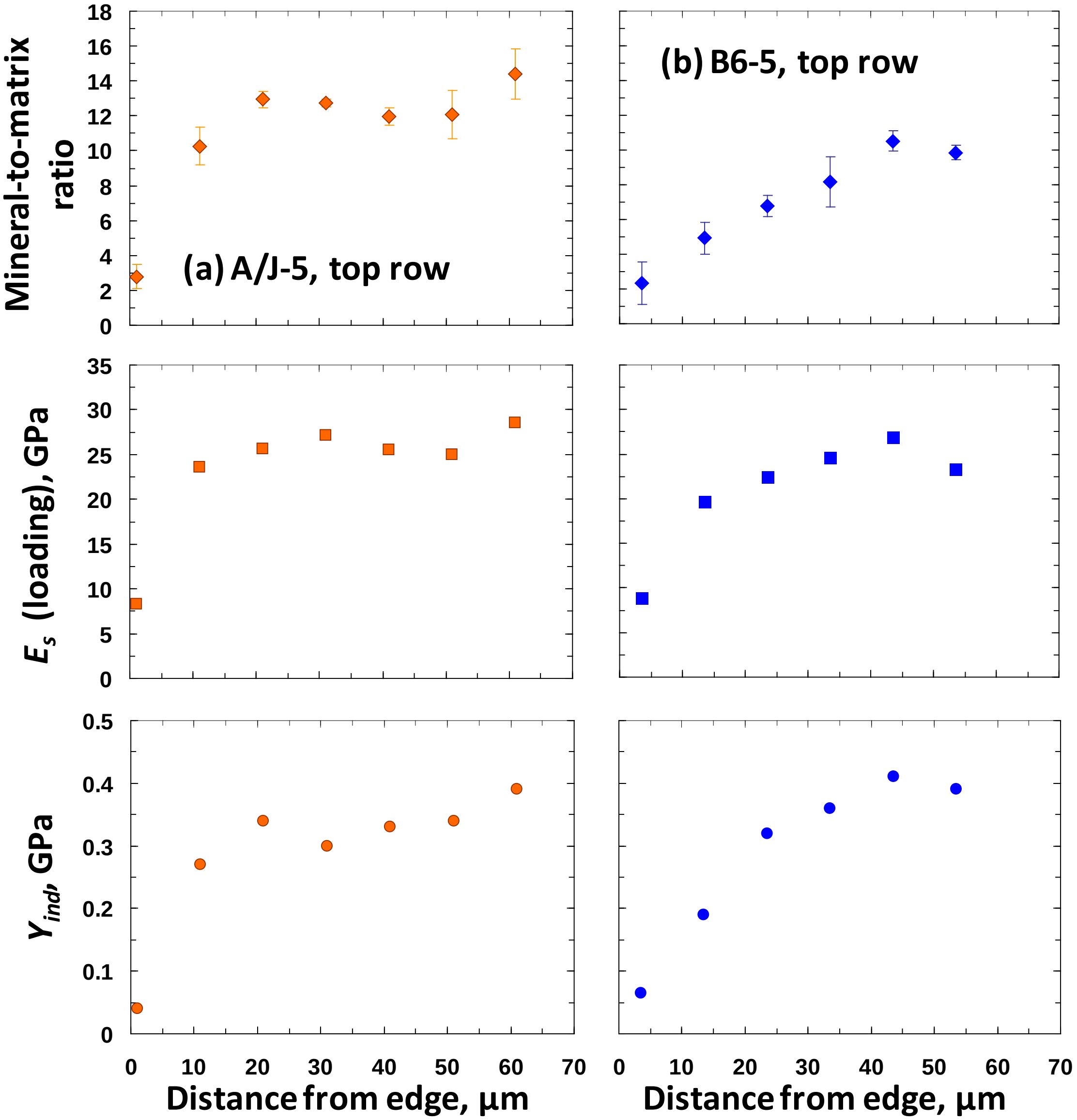

Figure A.5. Variations of the mineral-to-matrix ratios across a representative row of in (a) A/J sample #5 and (b) B6, sample #5 mouse femora as a function of their associated sample indentation modulus (Es, from the loading segment) and the indentation yield (Yind) values.

time calculated from the unloading portion of the load-displacement plot using the Oliver–Pharr technique [62], as a function of the mineral-to-matrix ratio. When contrasted with Figure A.6(a), the data in Figure A.6 (b) shows a much weaker relationship between the two variables. In addition, modulus values from the unloading segments tend to be lower than the values from the loading segments. Figure A.6 (c) and (d) compare of the post-elastic behavior of bone tissue under indentation to their local composition. Figure A.6(c) shows Y_{ind}, calculated at 0.2% offset strain, as a function of the mineral-to-matrix ratio across the two mouse strains. The figure shows a clear positive linear relationship between Y_{ind} and the mineral-to-matrix ratio, although the correlation is slightly weaker than that of the modulus measured from the loading segments. As in the case of the modulus data from Figure A.6(a), the values from the B6 sample are lower and they also show a wider range than A/J. In comparison, Figure A.6(d) shows the conventional hardness values as a function of the mineral-to-matrix ratio across the two mouse strains. As in the case of the modulus values, the hardness values also show a much weaker correlation compared to the Y_{ind} values calculated from the initial loading segment of the test. Our results demonstrate that data measured using the initial loading portions of the indentation tests (both E_s from loading and Y_{ind}) show a much higher correlation with mineral to matrix ratio than those measured using the unloading curves (namely E_s from unloading and the hardness)

A.4 Discussion

At 16 weeks of age, when the mice were sacrificed, the bones had attained their peak mass. It is known [111-112] that the growth in these mice femora is characterized by a pattern of cortical drift where new bone in being deposited at the endosteal surface

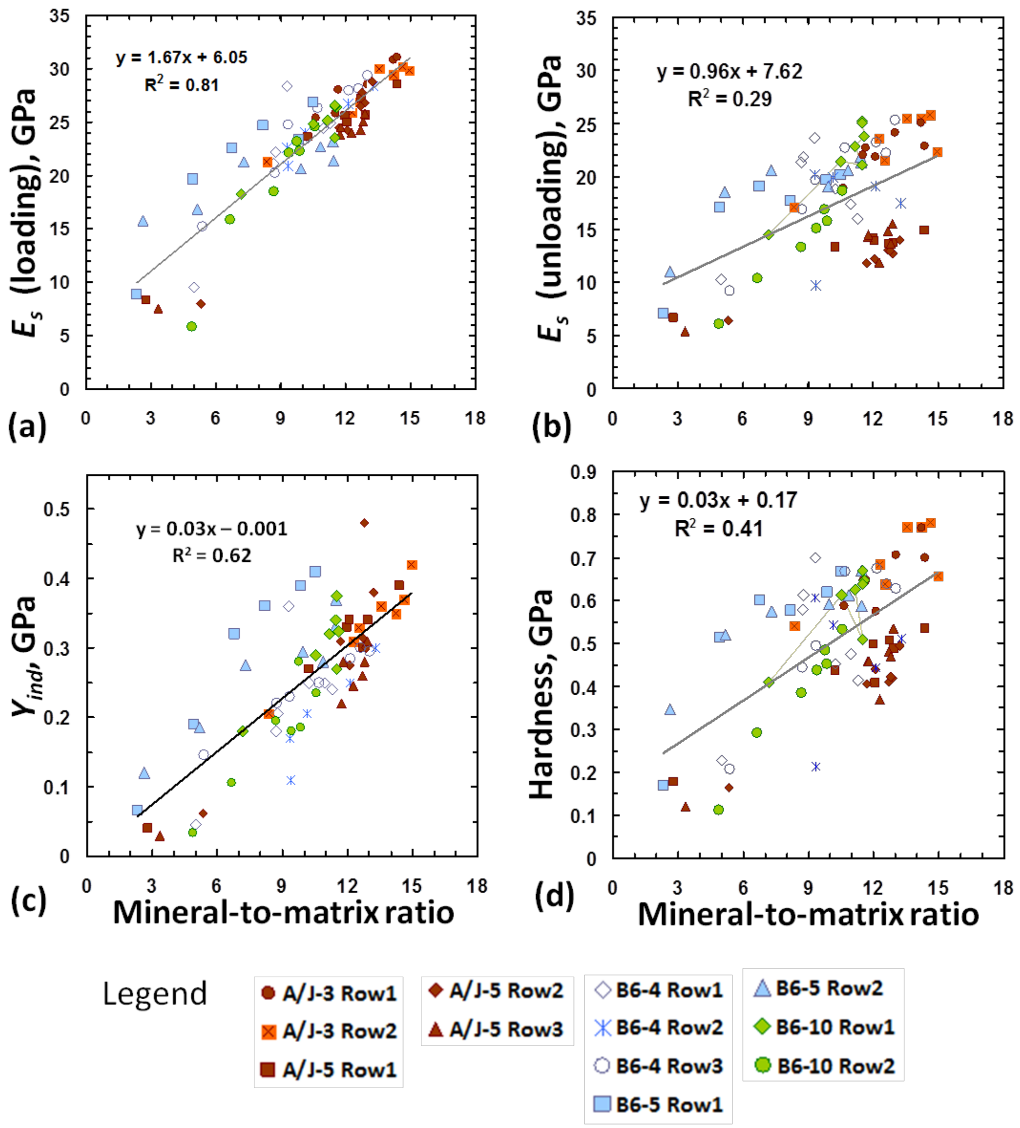

Figure A.6: Scatter plots of (a) the elastic modulus Es measured from the initial loading segment of the indentation stress-strain curves, (b) Es calculated from the unloading portion of the load-displacement data, (c) indentation yield strength (Yind) and (d) indentation hardness at max load, all as functions of the mineral-to-matrix ratio measured by Raman spectroscopy across two A/J and three B6 samples. The table in (e) shows the coefficient of determination (R2) values using both linear and exponential fits of the measured data.

of the antero-medial cortex and the periosteal surface of the postero-lateral cortex. Thus in our area of interest (endosteal region of the antero-medial cortex), newer bone is present close to the edge while, old, more mature bone is present away from the bone edge. In order to determine if the local composition in bone, as measured by Raman spectroscopy, is significantly different between the two mouse strains in question, a detailed statistical analysis was performed on compositional data obtained from the 5 samples of A/J and 6 samples of B6 mouse strain.

The average mineral to matrix ratio including data from the entire area mapped by Raman, considering all the samples tested (N=5 in each strain) was significantly ($p < 0.05$) lower in the B6 relative to the A/J mouse samples. This observation supports earlier findings that the A/J mouse had a higher whole bone ash content compared to B6 mouse femur. Additionally, there is very strong evidence, on the basis of 4 separate t-tests or the Hotelling's T2 test that the bone composition (all four ratios discussed above) is significantly different ($p < 10^{-5}$) in the two mouse strains. On the basis of exploratory data analysis including estimated density plots and normal probability plots, the distributions of the bone compositions were found to be mildly non-normal. However, because of the large sample size, the t-tests are robust [119] to non-normality. When using four independent t-tests, we assessed statistical significance using a per-test p-value of alpha = 0.05/4 = 0.0125.

We also investigated whether this is a clear individual mouse effect within strain using the Bayesian Information Criterion (BIC). The BIC ($BIC = MSE + n\log(p)$, where MSE is the mean squared error, n is the sample size, and p is the number of parameters) is a common method to select the number of parameters in a model, and is a residual sum of squares that includes a penalty term to guard against over-fitting by using too many parameters. The BIC values suggested that there is negligible reduction in the *MSE* if additional individual-mouse-effect terms are added.

Confocal imaging studies in order to visualize the calcein labels along the endosteal aspect of the antero-medial cortex (not included in this work) have shown that both the A/J and the B6 mice lay down bone at the same rate. Therefore, the measured distance from the edge is used as a surrogate for bone age. The measurements of the distance from the bone edge have nearly the same distribution in the A/J and B6 strains. Hence, the differences in composition are due to strain differences, not due to different age distributions.

Further, using distance from edge as a surrogate for bone age, the composition data was binned into three groups: New bone region was defined as region within 10 µm from the bone endosteal edge and old bone was defined as bone greater that 50 µm away from the edge. All bone in between was binned as being of intermediate age. A smooth curve was then fit to a scatter plot for composition vs. distance from the edge for each bin. For curve smoothing, we experimented with cubic polynomials, smoothing splines, and exponential fitting by fitting a cubic polynomial to the log transformed composition and then back transforming to the original scale. 4 separate T-tests for each bin, one for each of the ratios of interest determined from the Raman Spectroscopy data were again used to determine the statistical significance in the differences between the two much strains. Our results show that differences in the mineral to matrix ratio (determined by the phosphate to CH_2 wag peak ratio) and mineral maturity are not very significant in the new bone ($0.05 < p < 0.22$). In the old bone region, where there is not much difference in the mineral maturity ($p > 0.6$), the mineral to matrix ratio is significantly different ($p < 10^{-12}$). The carbonate substitutions and phosphate to amide peak intensity ratio are significantly different for all age groups. Therefore, it can be concluded that the mineralization in the new bone is very similar for the two mice strains and differences are developed as the bone ages.

Several attempts have been made literature to correlate the mechanical behavior of bone with the bone composition. Boivin et al. [120] have reported that microhardness measurements and degree of mineralization were both significantly lower in osteoporotic patients as compared to the controls. Follet et al. [121] used uniaxial compression of samples cut out from human calcanai and contact microradiography method [122-124] to conclude that the degree of mineralization was a determinant of bone strength. These approaches however have a much lower spatial resolution and the measurements are still being averaged over relatively large regions. Alternatively, when nanoindentation testing was used by Zebaze et al [125], it was found that the bone tissue mineralization account for little of the differences in the bone's mechanical properties in human femur. Zebaze and colleagues, like several other studies [98, 126-128], used a sharp (Berkovich) tip and the unloading segments of the nanoindentation tests for their calculations which might have rendered nanoindentation testing less sensitive to the local composition. The novel data analysis protocols for spherical nanoindentation, that convert the raw data into indentation stress-strain curves produce much more reliable measurements of the local mechanical behavior in bone. The elastic modulus and indentation yield point (Y_{ind}), calculated from the initial loading segment showed a much higher correlation with the local mineral-to-matrix ratio in the bone as compared to the elastic modulus and hardness values extracted from unloading segments.

The variation of the local elastic modulus and indentation yield strength as a function of bone composition is shown in Figure 5. As suggest by from these figures and confirmed by statistical analysis, there is a strong relationship between the mineral to matrix ratio (P-CH2 wag peak intensity ratio) and the local properties extracted from the initial loading segment of the indentation stress-strain curves. There is a highly significant linear correlation between the local mechanical properties and the mineral to matrix ratio. However, P-Amide1 ratio, which is also used as a measure of the mineral-to matrix ratio did not seem to have as strong an influence on the local properties. Based on the Bayesian Information Criterion (BIC) evaluations, including information about other compositional aspects such as mineral maturity and carbonate substitutions, mouse strain and/or the individual mouse IDs for the fit did not improve the correlations significantly. This might change however if other functional forms for the relationship between composition and properties is used and this possibility will investigated in continuing work. Note here that while Figure A.6 shows data obtained only from 5 individuals (2 A/J and 3 B6 mouse samples), for the statistical analysis all the data obtained from 5 A/J and 6 B6 mouse samples was used.

A.5 Conclusions

Our investigations using Raman Spectroscopy and spherical nanoindentation establish that the bone composition in A/J mice was significantly different from the B6 mice. While bone laid down by these two mice strains was of similar quality, in terms of its mineralization, differences developed as bone aged. A novel way to characterize local mechanical behavior at the sub-micron level in bone was successfully demonstrated and applied to show statistically significant correlation between the mineral to matrix ratio (defined as the phosphate to CH_2 peak intensity ratio) and the local mechanical properties, extracted from the initial loading segment of the nanoindentation data. Intra-strain differences in both bone composition and relationship between composition and properties were found to be statistically insignificant.

REFERENCES

1. Hay, J.L. and G.M. Pharr, *Instrumented indentation testing*, ASM Handbook.

2. Hay, J.C., A. Bolshakov, and G.M. Pharr, *A critical examination of the fundamental relations used in the analysis of nanoindentation data.* Journal of Materials Research, 1999. **14**(6): p. 2296-2305.

3. Fischer-Cripps, A.C., *A review of analysis methods for sub-micron indentation testing.* Vacuum, 2000. **58**(4): p. 569-585.

4. Fischer-Cripps, A.C., *Nanoindentation*. Mechanical Engineering Series, ed. F.F. Ling. 2002, New York: Springer.

5. Kalidindi, S.R. and S. Pathak, *Determination of the effective zero-point and the extraction of spherical nanoindentation stress-strain curves.* Acta Materialia, 2008. **56**: p. 3523-32.

6. Pathak, S., J. Shaffer, and S.R. Kalidindi, *Determination of an effective zero-point and extraction of indentation stress-strain curves without the continuous stiffness measurement signal.* Scripta Materialia, 2009. **60**: p. 439-42.

7. Kalidindi, S.R., A. Bhattacharya, and R. Doherty, *Detailed Analysis of Plastic Deformation in Columnar Polycrystalline Aluminum Using Orientation Image Mapping and Crystal Plasticity Models.* Proceedings of the Royal Society of London: Mathematical, Physical and Engineering Sciences., 2004. **460**(2047): p. 1935 - 1956

8. Doherty, R.D., et al., *Current issues in recrystallization: a review.* Materials Science and Engineering A, 1997. **238**(2): p. 219-274.

9. Anthony D. Rollett, A.P.B., C.G. Roberts, *An Overview of Accomplishments and Challenges in Recrystallization and Grain Growth.* Materials Science Forum, 2007. **558-559**: p. 33-42.

10. Faivre, P. and R.D. Doherty, *Nucleation of recrystallization in compressed aluminum: Studies by electron microscopy and Kikuchi diffraction. .* Journal of Materials Science, 1979. **14**: p. 897-919.

11. Bellier, S.P. and R.D. Doherty, *The Structure of Deformed Aluminum and Its Recrystallization--Investigations With Transmission Kossel Diffraction.* Acta Metallurgica et Materialia, 1977. **25**(5): p. 521-538.

12. Doherty, R.D., *The Deformed State and Nucleation of Recrystallization* Materails Science, 1974. **8**(1): p. 132-142.

13. F.H. Humphreys, M.H., *Recrystallization and Related Annealing Phenomena*. 1995, Oxford: Pergamon Press.

14. Cottrell, A.H., *Theory of dislocations.* Progress in Metal Physics, 1953. **4**: p. 205-264.

15. Viswanathan, R. and C.L. Bauer, *Kinetics of grain boundary migration in copper bicrystals with [001] rotation axes.* Acta Metallurgica, 1973. **21**: p. 1099-108.

16. Hutchinson, W.B., *Recrystallisation textures in iron resulting from nucleation at grain boundaries.* Acta Metallurgica, 1989. **37**(4): p. 1047-1056.

17. Y. Inokuti, R.D.D., *Transmission Kossel Study of the Structure of Cold-Rolled Iron and its Nucleation Behaviour.* Texture of Crystalline Solids, 1977. **2**(3): p. 143-168.

18. Doherty, R.D. and J.A. Szpunar, *Kinetics of sub-grain coalescence-a reconsideration of the theory.* Acta Metallurgica, 1984. **32**: p. 1789-98.

19. Schmidt, U. and K. Lucke, *Recrystallization textures of silver, copper and -brasses with different zinc-contents as a function of the rolling temperature.* Texture of Crystalline Solids, 1979. **3**: p. 85-112.

20. Doherty, R.D., K. Kashyap, and S. Panchanadeeswaran, *Direct observation of the development of recrystallization texture in commercial purity aluminum.* Acta Metallurgica et Materialia, 1993. **41**: p. 3029-53.

21. Hjelen, J., R. Orsund, and E. Nes, *On the origin of recrystallization textures in aluminium.* Acta Metallurgica et Materialia, 1991. **39**(7): p. 1377-1404.

22. Doherty, R.D., *Recrystallization and Texture.* Progress in Materials Science, 1997. **42**: p. 39-58.

23. Doherty, R.D., L.-C. Chen, and I. Samajdar, *Cube recrystallization texture--experimental results and modeling.* Materials Science and Engineering A, 1998. **257**(1): p. 18-36.

24. Inokuti, Y. and R.D. Doherty, *Transmission Kossel Study of the Structure of Compressed Fe and Its Recrystallization Behaviour.* Acta Metallurgica et Materialia, 1978. **26**(1): p. 61-80.

25. Taylor, G.I., *Plastic strain in metals.* Journal of the Institute of Metals, 1938. **62**: p. 307-324.

26. Sachs, G., *Stresses causing flow*

Zur Ableitung einer Fliessbedingung. V.D.I. Zeitschrift, 1928. **72**(22): p. 734-736.

27. Kalidindi, S.R., *Incorporation of deformation twinning in crystal plasticity models.* Journal of the Mechanics and Physics of Solids, 1998. **46**(2): p. 267-271.

28. Van Houtte, P., L. Delannay, and S.R. Kalidindi, *Comparison of two grain interaction models for polycrystal plasticity and deformation texture prediction.* International Journal of Plasticity, 2002. **18**(3): p. 359-377.

29. Panchanadeeswaran, S., R.D. Doherty, and R. Becker, *Direct observation of orientation change by channel die compression of polycrystalline aluminum - use of a split sample.* Acta Materialia, 1996. **44**(3): p. 1233-1262.

30. Panchanadeeswaran, S., R.D. Doherty, and R. Becker, *Direct observation of orientation change by channel die compression of polycrystalline aluminum--Use of a split sample.* Acta Materialia, 1996. **44**(3): p. 1233-1262.

31. Quey, R., D. Piot, and J.H. Driver, *Microtexture tracking in hot-deformed polycrystalline aluminium: Experimental results.* Acta Materialia, 2010. **58**(5): p. 1629-1642.

32. Kallend, J.S. and Y.C. Huang, *Orientation dependence of stored energy of cold work in 50% cold rolled copper.* Metal Science, 1984. **18**(7): p. 381-386.

33. Sam, D. and B. Adams, *Orientation and strain dependence of stored energy of cold work in axisymmetric copper.* Metallurgical Transactions A, 1986. **17**(3): p. 513-517.

34. Borbély, A., J.H. Driver, and T. Ungár, *An X-ray method for the determination of stored energies in texture components of deformed metals; application to cold worked ultra high purity iron.* Acta Materialia, 2000. **48**(8): p. 2005-2016.

35. Godfrey, A., N. Hansen, and D. Juul Jensen, *Microstructural-Based Measurement of Local Stored Energy Variations in Deformed Metals.* Metallurgical and Materials Transactions A, 2007. **38**(13): p. 2329-2339.

36. Rajmohan, N., et al., *Neutron diffraction method for stored energy measurement in interstitial free steel.* Acta Materialia, 1997. **45**(6): p. 2485-2494.

37. Hazra, S.S., A.A. Gazder, and E.V. Pereloma, *Stored energy of a severely deformed interstitial free steel.* Materials Science and Engineering: A, 2009. **524**(1–2): p. 158-167.

38. Hordon, M.J. and B.L. Averbach, *X-ray measurements of dislocation density in deformed Copper and Aluminum single crystals.* Acta Metallurgica, 1961. **9**(3): p. 237-246.

39. Hall, E.O., *The Deformation and Ageing of Mild Steel: III Discussion of Results* Proceedings of the Physical Society. Section B 1951. **64**(9).

40. Petch, N.J., *Cleavage strength of polycrystals.* Iron and Science Institure-journal, 1953. **173**.

41. Cottrell, A.H., *Theory of brittle fracture in steel and similar metals.* Metallurgical Society of American Institute of Mining, Metallurgical and Petroleum Engineers -- Transactions, 1958: p. 212.

42. Meyers MA, A.E., *A model for the effect of grain size on the yield stress of metals.* Philosophical Magazine A, 1982. **46**: p. 737.

43. Kobayashi, S., S. Tsurekawa, and T. Watanabe, *Grain boundary hardening and triple junction hardening in polycrystalline molybdenum.* Acta Materialia, 2005. **53**(4): p. 1051-1057.

44. Kobayashi, S., S. Tsurekawa, and T. Watanabe, *Roles of structure-dependent hardening at grain boundaries and triple junctions in deformation and fracture of molybdenum polycrystals.* Materials Science and Engineering: A, 2008. **483–484**(0): p. 712-715.

45. Ng, K.S. and A.H.W. Ngan, *Deformation of micron-sized aluminium bi-crystal pillars.* Philosophical Magazine, 2009. **89**(33): p. 3013-3026.

46. Kunz, A., S. Pathak, and J.R. Greer, *Size effects in Al nanopillars: Single crystalline vs. bicrystalline.* Acta Materialia, 2011. **59**(11): p. 4416-4424.

47. Dietiker, M., et al., *Deformation behavior of gold nano-pillars prepared by nanoimprinting and focused ion-beam milling.* Acta Materialia, 2011. **59**(5): p. 2180-2192.

48. Soer, W.A. and J.T.M. De Hosson, *Detection of grain-boundary resistance to slip transfer using nanoindentation.* Materials Letters, 2005. **59**(24–25): p. 3192-3195.

49. Soer, W.A., K.E. Aifantis, and J.T.M. De Hosson, *Incipient plasticity during nanoindentation at grain boundaries in body-centered cubic metals.* Acta Materialia, 2005. **53**(17): p. 4665-4676.

50. T.B. Britton, D.R., A.J. Wilkinson, *Nanoindentation study of slip transfer phenomenon at grain boundaries.* Journal of Materials Research, 2009. **24**: p. 607-615.

51. Wang, M.G. and A.H.W. Ngan, *Indentation strain burst phenomenon induced by grain boundaries in niobium.* Journal of Materials Research, 2004. **19**(8): p. 2478-86.

52. Wo, P.C. and A.H.W. Ngan, *Investigation of slip transmission behavior across grain boundaries in polycrystalline Ni3Al using nanoindentation.* Journal of Materials Research, 2004. **19**(01): p. 189-201.

53. Ohmura, T., et al., *Dislocation-grain boundary interactions in martensitic steel observed through in situ nanoindentation in a transmission electron microscope.* Journal of Materials Research, 2004. **19**(12): p. 3626-3632.

54. Hosson, J.M., et al., *In situ TEM nanoindentation and dislocation-grain boundary interactions: a tribute to David Brandon.* Journal of Materials Science, 2006. **41**(23): p. 7704-7719.

55. Zhang, H., et al., *The design of accurate micro-compression experiments.* Scripta Materialia, 2006. **54**(2): p. 181-186.

56. Hemker, K.J. and W.N. Sharpe Jr, *Mechanical Testing of Very Small Samples*, in *Encyclopedia of Materials: Science and Technology (Second Edition)*, K.H.J.B. Editors-in-Chief: , et al., Editors. 2006, Elsevier: Oxford. p. 1-6.

57. Tabor, D., *The hardness of metals*. 1951: Clarendon Press, Oxford University Press. ix + 176.

58. Hertz, H., *Miscellaneous Papers.* New York: MacMillan and Co., Ltd, 1896.

59. Johnson, K.L., *Indentation Contact Mechanics*. 1985: Cambridge University Press, Cambridge.

60. Oliver, W.C. and G.M. Pharr, *Measurement of hardness and elastic modulus by instrumented indentation: Advances in understanding and refinements to methodology*. Journal of Materials Research, 2004. **19**: p. 3-20.

61. Doerner, M.F. and W.D. Nix, *A method for interpreting the data from depth-sensing indentation instruments.* J. Mater. Res., 1986. **1**(4): p. 601-609.

62. Oliver, W.C. and G.M. Pharr, *Improved technique for determining hardness and elastic modulus using load and displacement sensing indentation experiments.* Journal of Materials Research, 1992. **7**(6): p. 1564-1580.

63. Pathak, S., D. Stojakovic, and S.R. Kalidindi, *Measurement of the local mechanical properties in polycrystalline samples using spherical nanoindentation and orientation imaging microscopy.* Acta Materialia, 2009. **57**: p. 3020-8.

64. Pathak, S., et al., *Studying grain boundary regions in polycrystalline materials using spherical nano-indentation and orientation imaging microscopy*. Journal of Materials Science, 2012. **47**(2): p. 815-823.

65. Pathak, S., et al., *Viscoelasticity and high buckling stress of dense carbon nanotube brushes.* Carbon, 2009. **47**: p. 1969-1976.

66. Pathak, S., et al., *Assessment of lamellar level properties in mouse bone utilizing a novel spherical nanoindentation data analysis method.* Journal of the Mechanical Behavior of Biomedical Materials, 2012. **13**(0): p. 102-117.

67. Sneddon, I.N., *Relation between load and penetration in axisymmetric Boussinesq problem for punch of arbitrary profile.* International Journal of Engineering Science, 1965. **3**: p. 47-57.

68. Li, X. and B. Bhushan, *A review of nanoindentation continuous stiffness measurement technique and its applications.* Materials Characterization, 2002. **48**(1): p. 11-36.

69. Gene Simmons, H.W., *Single Crystal Elastic Constants and Calculated Aggregate Properties*. 1971, Cambridge MIT Press.

70. Vlassak, J.J. and W.D. Nix, *Measuring the elastic properties of anisotropic materials by means of indentation experiments.* Journal of the Mechanics and Physics of Solids, 1994. **42**(8): p. 1223-1245.

71. Field, J.S. and M.V. Swain, *A simple predictive model for spherical indentation.* Journal of Materials Research, 1993. **8**(02): p. 297-306.

72. Basu, S.M., Alexander; Barsoum, Michel W., *On the determination of spherical nanoindentation stress?strain curves.* Journal of Materials Research, 2006. **21**(10): p. 2628-2637.

73. Donohue, B.R., A. Ambrus, and S.R. Kalidindi, *Critical evaluation of the indentation data analyses methods for the extraction of isotropic uniaxial*

mechanical properties using finite element models. Acta Materialia, 2012. **60**(9): p. 3943-3952.

74. Pathak, S., et al., *Importance of surface preparation on the nano-indentation stress-strain curves measured in metals.* Journal of Materials Research, 2009. **24**: p. 1142-55.

75. G.M. Pharr, J.H.S.a.W.C.O., *Critical issues in making small-depth mechanical property measurements by nanoindentation with continuous stiffness measurement.* Journal of Materials Research, 2009. **24**: p. 653-666.

76. Cordill, M.J., N.R. Moody, and W.W. Gerberich, *Effects of dynamic indentation on the mechanical response of materials.* Journal of Materials Research, 2008. **23**(Compendex): p. 1604-1613.

77. Cordill, M.J., et al., *The Nano-Jackhammer effect in probing near-surface mechanical properties.* International Journal of Plasticity, 2009. **25**: p. 2045-58.

78. Asif, S.A.S., K.J. Wahl, and R.J. Colton, *Nanoindentation and contact stiffness measurement using force modulation with a capacitive load-displacement transducer.* Review of Scientific Instruments, 1999. **70**: p. 2408-13.

79. Asif, S.A.S., et al., *Quantitative imaging of nanoscale mechanical properties using hybrid nanoindentation and force modulation.* Journal of Applied Physics, 2001. **90**: p. 1192-200.

80. Cordill, M.J., N.R. Moody, and W.W. Gerberich, *The role of dislocation walls for nanoindentation to shallow depths.* International Journal of Plasticity, 2009. **25**: p. 281-301.

81. VanLandingham, M.R., et al., *Viscoelastic characterization of polymers using instrumented indentation. I. Quasi-static testing*.* Journal of Polymer Science Part B: Polymer Physics, 2005. **43**(14): p. 1794-1811.

82. Mencik, J., et al., *Determination of elastic modulus and hardness of viscoelastic-plastic materials by instrumented indentation under harmonic load.* Journal of Materials Research, 2005. **20**(10): p. 2660-9.

83. Pharr, G.M. and A. Bolshakov, *Understanding nanoindentation unloading curves.* Journal of Materials Research, 2002. **17**(10): p. 2660-71.

84. Herbert, E.G., et al., *On the measurement of stress-strain curves by spherical indentation.* Thin Solid Films, 2001. **398-399**: p. 331-335.

85. Gerberich, W.W., et al., *The injection of plasticity by millinewton contacts.* Acta Metallurgica et Materialia, 1995. **43**: p. 1569-76.

86. Bahr, D.F., et al. *Yield point phenomena during indentation*. in *Fundamentals of Nanoindentation and Nanotribology. Symposium, 13-17 April 1998*. 1998. Warrendale, PA, USA: Mater. Res. Soc.

87. Gouldstone, A., et al., *Discrete and continuous deformation during nanoindentation of thin films.* Acta Materialia, 2000. **48**: p. 2277-95.

88. Schuh, C.A. and A.C. Lund, *Application of nucleation theory to the rate dependence of incipient plasticity during nanoindentation.* Journal of Materials Research, 2004. **19**: p. 2152-2158.

89. *Metallography and Microstructures*, in *ASM handbooks Online*, G.F.V. Voort, Editor. 2004.

90. Adams, B.L., *Orientation imaging microscopy: applications to the characterization of the grain-boundary network.* Materials Science Forum

Proceedings of the 1995 7th International Conference on Intergranular and Interphase Boundaries in Materials, Jun 26-29 1995, 1996. **207-209**(pt 1): p. 13-22.

91. Bunge, H.-J., *Texture analysis in materials science. Mathematical Methods*. 1993, Göttingen: Cuvillier Verlag.

92. Meyers, M.A., K.K. Chawla,, *Mechanical Metalurgy: Principles and Applications*. 1984: Prentice-Hall, New York.

93. Gundlach, C., et al., *Direct observation of subgrain evolution during recovery of cold-rolled aluminium.* Scripta Materialia, 2004. **50**(4): p. 477-481.

94. Bhattacharyya, A., et al., *Evolution of grain-scale microstructure during large strain simple compression of polycrystalline aluminum with quasi-columnar grains: OIM measurements and numerical simulations.* International Journal of Plasticity, 2001. **17**(6): p. 861-883.

95. Kalidindi, S.R., *Special issue on: Plasticity and microstructure evolution.* International Journal of Plasticity, 2001. **17**(6): p. 781-781.

96. Dillamore, I.L., Morris P. L., Smith C. J. E. , Hutchinson W. B., *Transition Bands and Recrystallization in Metals.* Proceedings of the Royal Society A, 1972. **329**: p. 405-420.

97. Stojakovic, D., *Micorstructure Evolution in Deformed and Recrystallized Electrical Steel*, in *Materials Science and Engineering*. 2008, Drexel University: Philadlephia. p. 101.

98. Fan, Z., et al., *Anisotropic properties of human tibial cortical bone as measured by nanoindentation.* Journal of orthopaedic research, 2002. **20**(4): p. 806-810.

99. Kazanci, M., et al., *Bone osteonal tissues by Raman spectral mapping: orientation–composition.* Journal of Structural Biology, 2006. **156**(3): p. 489-496.

100. Ager, I.J.W., et al., *Deep-ultraviolet Raman spectroscopy study of the effect of aging on human cortical bone.* Journal of Biomedical Optics, 2005. **10**(3): p. 034012-0340128.

101. Akkus, O., F. Adar, and M.B. Schaffler, *Age-related changes in physicochemical properties of mineral crystals are related to impaired mechanical function of cortical bone.* Bone, 2004. **34**(3): p. 443-453.

102. Ramasamy, J. and O. Akkus, *Local variations in the micromechanical properties of mouse femur: the involvement of collagen fiber orientation and mineralization.* Journal of biomechanics, 2007. **40**(4): p. 910-918.

103. Fan, Z. and J.Y. Rho, *Effects of viscoelasticity and time-dependent plasticity on nanoindentation measurements of human cortical bone.* Journal of Biomedical Materials Research Part A, 2003. **67**(1): p. 208-214.

104. Tai, K., H.J. Qi, and C. Ortiz, *Effect of mineral content on the nanoindentation properties and nanoscale deformation mechanisms of bovine tibial cortical bone.* Journal of Materials Science: Materials in Medicine, 2005. **16**(10): p. 947-959.

105. Goodwin, K.J. and N.A. Sharkey, *Material properties of interstitial lamellae reflect local strain environments.* Journal of orthopaedic research, 2002. **20**(3): p. 600-606.

106. Gamsjaeger, S., et al., *Cortical bone composition and orientation as a function of animal and tissue age in mice by Raman spectroscopy.* Bone, 2010. **47**(2): p. 392-399.

107. Grey, A., et al., *Bone mineral density and body composition in adult patients with cystic fibrosis.* Thorax, 1993. **48**(6): p. 589-593.

108. Boskey, A. and N. Pleshko Camacho, *FT-IR imaging of native and tissue-engineered bone and cartilage.* Biomaterials, 2007. **28**(15): p. 2465-2478.

109. Jepsen, K.J., et al., *Bone brittleness varies with genetic background in A/J and C57BL/6J inbred mice.* Journal of Bone and Mineral Research, 2001. **16**(10): p. 1854-1862.

110. Jepsen, K.J., et al., *Hierarchical relationship between bone traits and mechanical properties in inbred mice.* Mammalian Genome, 2003. **14**(2): p. 97-104.

111. Price, C., et al., *Genetic variation in bone growth patterns defines adult mouse bone fragility.* Journal of Bone and Mineral Research, 2005. **20**(11): p. 1983-1991.

112. Beamer, W.G., et al., *Genetic variability in adult bone density among inbred strains of mice.* Bone, 1996. **18**(5): p. 397-403.

113. Courtland, H.-W., et al., *Fourier Transform Infrared Imaging Microspectroscopy and Tissue-Level Mechanical Testing Reveal Intraspecies Variation in Mouse Bone Mineral and Matrix Composition.* Calcified Tissue International, 2008. **83**(5): p. 342-353.

114. Courtland, H.W., et al., *Genetic Variation in Mouse Femoral Tissue-Level Mineral Content Underlies Differences in Whole Bone Mechanical Properties.* Cells Tissues Organs, 2009. **189**(1-4): p. 237-240.

115. Carden, A. and M.D. Morris, *Application of vibrational spectroscopy to the study of mineralized tissues (review).* Journal of Biomedical Optics, 2000. **5**(3): p. 259-268.

116. Timlin, J.A., A. Carden, and M.D. Morris, *Chemical Microstructure of Cortical Bone Probed by Raman Transects.* Applied Spectroscopy, 1999. **53**(11): p. 1429-1435.

117. Boskey, A.L., Pleshko, N., Doty, S.B., Mendelsohn, R, *Applications of Fourier transform infrared (FT-IR) microscopy to the study of mineralization in bone and cartilage.* Cells and Materials and Corrosion, 1992(2): p. 209-220.

118. Yeni, Y.N., et al., *Effect of Fixation and Embedding on Raman Spectroscopic Analysis of Bone Tissue.* Calcified Tissue International, 2006. **78**(6): p. 363-371.

119. Thomas, E., *Miller, Rupert G. Jr.: Beyond ANOVA, Basics of Applied Statistics. Wiley, New York – Chichester – Brisbane – Toronto – Singapore 1986, 317 S., £ 30.65; ISBN 0-471-81922-0.* Biometrical Journal, 1988. **30**(7): p. 874-874.

120. Boivin, G., et al., *The role of mineralization and organic matrix in the microhardness of bone tissue from controls and osteoporotic patients.* Bone, 2008. **43**(3): p. 532-538.

121. Follet, H., et al., *The degree of mineralization is a determinant of bone strength: a study on human calcanei.* Bone, 2004. **34**(5): p. 783-789.

122. Jowsey, J., et al., *Quantitative Microradiographic Studies of Normal and Osteoporotic Bone.* The Journal of Bone & Joint Surgery, 1965. **47**(4): p. 785-872.

123. Boivin G, B.C., *Microradiographic methods for calcified tissues.*, in *Methods of calcified tissue preparation*. 1984, Amsterdam: Elsevier. p. 391-411.

124. Boivin, G. and P.J. Meunier, *The Degree of Mineralization of Bone Tissue Measured by Computerized Quantitative Contact Microradiography.* Calcified Tissue International, 2002. **70**(6): p. 503-511.

125. Zebaze, R., et al., *Differences in the degree of bone tissue mineralization account for little of the differences in tissue elastic properties.* Bone, 2011. **48**(6): p. 1246-1251.

126. Rho, J.-Y., L. Kuhn-Spearing, and P. Zioupos, *Mechanical properties and the hierarchical structure of bone.* Medical Engineering & Physics, 1998. **20**(2): p. 92-102.

127. Rho, J.-Y. and G.M. Pharr, *Effects of drying on the mechanical properties of bovine femur measured by nanoindentation.* Journal of Materials Science: Materials in Medicine, 1999. **10**(8): p. 485-488.

128. Hengsberger, S., et al., *How is the indentation modulus of bone tissue related to its macroscopic elastic response? A validation study*. Journal of biomechanics, 2003. **36**(10): p. 1503-1509.